Development and Application of Flat Shell Element in Hybrid-type Penalty Method

VARDANIAN, Anna

(開始ページ / Start Page)
1
(終了ページ / End Page)
114
(発行年 / Year)
2023-03-24
(学位授与番号 / Degree Number)
32675甲第579号
(学位授与年月日 / Date of Granted)
2023-03-24
(学位名 / Degree Name)
博士(工学)
(学位授与機関 / Degree Grantor)
法政大学 (Hosei University)
(URL)
https://doi.org/10.15002/00026671

Dissertation for doctoral
degree reviewed by
Hosei University

Development and Application of Flat Shell Element in Hybrid-type Penalty Method

Anna Vardanian

TABLE OF CONTENTS

1 INTRODUCTION [1]

2 DEVELOPMENT OF FLAT SHELL ELEMENT BY HPM [5]

1 INTRODUCTION

1.1 Background and Objective

In recent years, the model order reduction (MOR) method [1], which improves the efficiency of processing calculations by reducing the number of dimensions of the model, has attracted attention in the field of stress analysis. For example, as shown in Figure 1.1, when a CAD model is used for analysis by the Finite Element Method (FEM) [2], the detailed modeling uses solid elements to divide the mesh. However, in the simplified modeling by the MOR method, elements with reduced orders, such as flat shell elements [3], are used. In this case, the simulation result can be obtained in a shorter time compared with the detailed modeling.

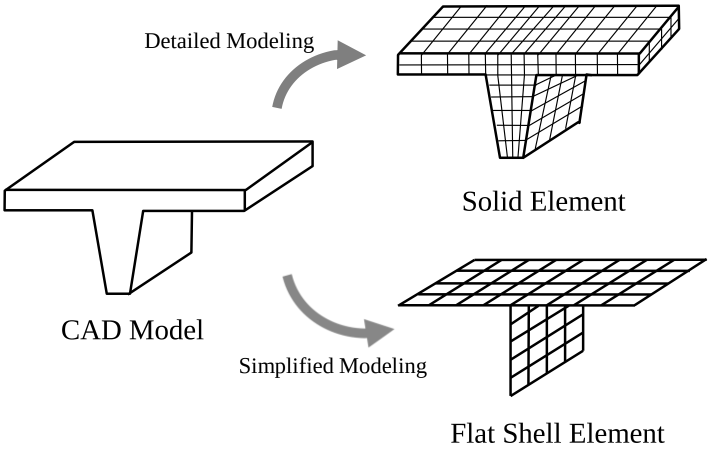

Fig.1.1 Modeling by the finite element method

Phenomena such as thermal cracking of flat glass cannot be expressed as cracking even if analyzed as an in-plane or out-of-plane deformation problem [4]. It is considered that such a phenomenon occurs when both the in-plane and out-of-plane deformation states occur at the same time. Flat shell elements can also be conveniently used to analyze problems that receive both in-plane and out-of-plane forces at the same time.

The development of shell elements for use in the finite element method has been underway since the 1960s [5], and new elements are still being researched. For example, Hamadi et al. [6] developed a flat shell element with four vertices in a quadrangle and one node within the element. In addition, benchmark problems were analyzed using general purpose software. Burand and Angalekar [7] analyzed a benchmark nonlinear problem using ANSYS software. Lamine et al. [8] analyzed the benchmark problem using ABAQUS and compared their results with experimental values.

Many studies have been conducted on shell structures for geometric nonlinear problems; Rivera et al. [9] verified their accuracy using elements with eight parameters. Sze et al. [10] also analyzed benchmark problems for various methods in geometric nonlinear problems.

In relation to the MOR mentioned earlier, a method using an interface element for the deformed connection has been proposed [11]. In recent years, models used in isogeometric analysis [12] have been developed [13],[14], and methods such as the isogeometric inverse finite element method have been studied [15].

Generally, to evaluate the safety of a structure, it is necessary to understand its destruction state and collapse load. When analyzing progressive fracture problems such as cracks, the handling of discontinuous parts is generally complicated. In order to solve these problems, various modeling techniques, such as discontinuous elements in FEM, have been studied [16]-[18].

The hybrid-type penalty method (HPM) [19]-[21], which is based on the principle of the hybrid virtual work [22], is one such analysis method. In the HPM, the analysis domain is decomposed into subregions, and an independent displacement field is assumed for each element. This displacement field is composed of rigid body displacement, strain, and gradient. HPM is suitable for the analysis of large displacement problems, wherein the rigid body displacement is dominant. In addition, if HPM can be used for the MOR method, it is possible to know the approximate fracture characteristics at the initial stage of structural design and provide useful information for safety evaluation. The HPM frame elements [23] and flat plate elements [24]-[26] required for simplified modeling of structures have already been developed.

The subsidiary condition regarding the continuity of displacement on the element boundary is introduced using the Lagrange multiplier. This undetermined multiplier physically equates to the surface force. Therefore, the idea of the spring of the rigid body spring model (RBSM) developed by Kawai [27] is applied to the Lagrange multiplier, and the penalty function is used as the spring constant; thus, the surface force between the subregions is expressed. The surface force is obtained from the relative displacement along the boundary between adjacent elements. By applying the fracture condition to the penalty function on the element boundary using this surface force, it is possible to introduce fracture phenomena, such as a slip, crack, or hinge. As mentioned above, HPM is used for the analysis of progressive fracture because the occurrence of cracks can be clearly expressed by treating the penalty function as a hard spring [28] [29].

However, when flat shell elements are used to model the shell structure of a shape, the adjacent elements are joined diagonally; therefore, it is challenging to obtain the relative displacement between the different coordinate systems.

The purpose of this study is to develop an algorithm and a shell model that utilizes the advantages of HPM, for material nonlinear large displacement analysis using the shell model. First, the displacement field represented by the local coordinate system, which is different for each element, is converted into the local coordinate system of one of the adjacent elements. Subsequently, it is converted into the coordinate system of the element boundary edge. Finally, we propose a method to calculate the relative displacement from the displacement of the boundary edge of the adjacent elements obtained in this manner.

1.2 Contents of this Study

This thesis is composed of 6 chapters, and the outline of the remaining chapters is as follows:

Chapter 2 first summarizes the assumptions as in-plane and out-of-plane problems and presents that the superposition of these constitutes a flat shell problem. Subsequently, the governing equation of the elastic problem and equation of the hybrid virtual work that is the basis of HPM are derived. Next, the HPM discretization equation for the flat shell problem is derived. Because this study is formulated based on the local coordinate system, the relationship between the coordinate systems is described. In addition, the quadratic displacement field used in the proposed model, relationship between the stress in the element and the moment, and relationship between the relative displacement and the surface force is described. Finally, the accuracy of the solution obtained by the proposed model is verified from simple numerical examples.

Chapter 3 describes the discrete limit analysis of the flat shell problem. First, the fracture conditions are described, and the relationship between the surface force and the constitutive equation in HPM is summarized. As a numerical algorithm for material nonlinear analysis, the r-min method (Yamada's method) in the load increment method is used. Next, the concept of load increment in this material nonlinear analysis is described, and the analysis flowchart of this nonlinear analysis method is shown. Finally, from a simple numerical calculation example, it is shown that the collapse load obtained by the proposed model is equivalent to the analytical solution.

Chapter 4 describes the large displacement analysis of the flat shell problem. In this study, the r-min method in the load increment method described in Chapter 3 is applied as an algorithm for large displacement analysis. To control the load increment, a limit rotation angle is introduced and described. In the large displacement problem, the coordinate transformation of the stress in the element is required owing to the rotation of the local coordinate system. The relationship between this coordinate transformation and the stress in the element is also described. Based on the above relationship, the algorithm for large displacement analysis is established. Finally, numerical examples using this algorithm are shown, and the characteristics and accuracy of the solution are discussed.

Chapter 5 describes large displacement analysis with material nonlinearity. The numerical algorithm for nonlinear analysis uses the r-min method in the load increment method described in Chapters 3 and 4. The rate of load increment is determined by simultaneously considering both the rate of load increment with respect to the strength, described in Chapter 3, and the rate of load increment owing to the limit rotation angle, described in Chapter 4. In this chapter, the details of this algorithm are presented. Finally, the characteristics of the solution obtained in the numerical examples using the proposed algorithm are described.

Chapter 6 summarizes the results obtained in this research and describes the future scope.

2 DEVELOPMENT OF FLAT SHELL ELEMENT BY HPM

2.1 Assumption of Flat Shell Problems

2.1.1 *Assumption of In-plane Problems*

Frequently, a 2D model can usefully represent a 3D model. The thin plate deformation problem has two analysis models as shown in Figure 2.1.1. Figure (a) shows an in-plane problem wherein in-plane deformation is caused by various loads acting in the plane. Figure (b) shows an out-of-plane problem wherein bending deformation occurs by the action of an out-of-plane force.

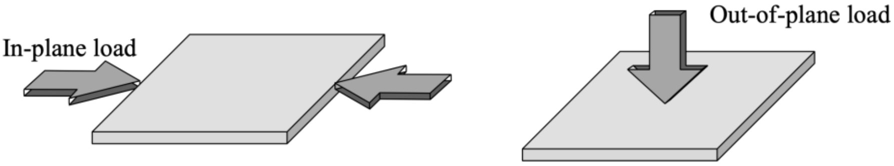

(a) in-plane problem (b) out-of-plane problem

Fig.2.1.1 Thin plate problem

There are two ways to model the in-plane deformation problem: to assume a plane stress condition, where the in-plane force is loaded to a sufficiently thin flat plate; or, to assume a plane strain condition, where the lateral force is loaded to a sufficiently long column. The plane stress and strain states are shown in Figure 2.1.2(a) and (b), respectively.

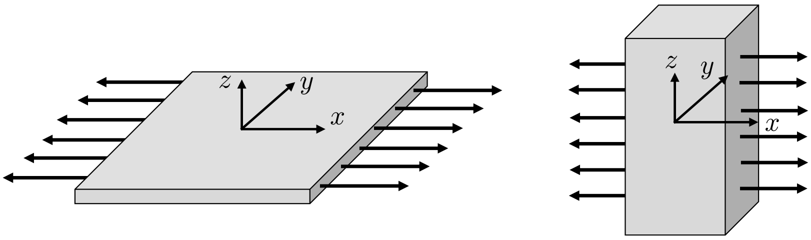

(a) plane stress (b) plane strain

Fig.2.1.2 In-plane deformation problem

Because thin plates are modeled in this study, plane stress conditions are assumed. The stress in the plate thickness direction is assumed to be 0 because the thickness is sufficiently low in the plane stress state, and it can deform freely. Therefore, the following assumptions are made:

$$\sigma_z = 0\ ,\quad \tau_{yz} = \tau_{zx} = 0 \tag{2.1.1}$$

2.1.2 *Assumption of Out-of-plane Problems*

The thin plate subjected to the out-of-plane load shown in Figure 2.1.1(b) can be modeled in two dimensions based on the Kirchhoff theory. The flat plate in Kirchhoff theory is assumed to be in the state where the elastic body of thickness *t* is placed on the neutral plane as shown in Figure 2.1.3. Assuming that the elastic body follows the behavior of the neutral plane in two dimensions, the flat plate can be treated identically as the neutral plane.

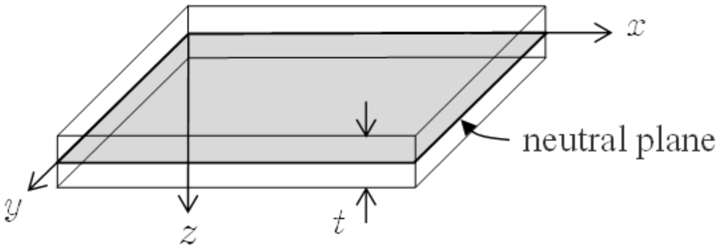

Fig.2.1.3 Plate and neutral plane in Kirchhoff theory

Following are the assumptions of Kirchhoff theory.

(i) Assume infinitesimal deformation that is not greater than plate thickness:

$$w << h\ ,\ \left(\frac{\partial w}{\partial x}\right)^2 << 1\ ,\ \left(\frac{\partial w}{\partial y}\right)^2 << 1 \tag{2.1.2}$$

(ii) The reference plane assumes no stretching:

$$\varepsilon_x = 0\ ,\ \varepsilon_y = 0\ ,\ \gamma_{xy} = 0 \quad \text{on}\ \ z = 0 \tag{2.1.3}$$

(iii) Normal direction is maintained:

$$\gamma_{zx} = \gamma_{yz} = 0 \tag{2.1.4}$$

(iv) The length in the normal direction is constant:

$$\varepsilon_z = 0 \tag{2.1.5}$$

(v) Normal stress is ignored:

$$\sigma_z \simeq 0 \tag{2.1.6}$$

2.1.3 *Flat Shell Problems*

The deformed state in the flat shell problem is shown in Figure 2.1.4. Horizontal displacement in the flat shell problem is the sum of displacement u_1 of in-plane deformation and displacement $-z(\partial w_1/\partial x)$ of out-of-plane deformation as shown.

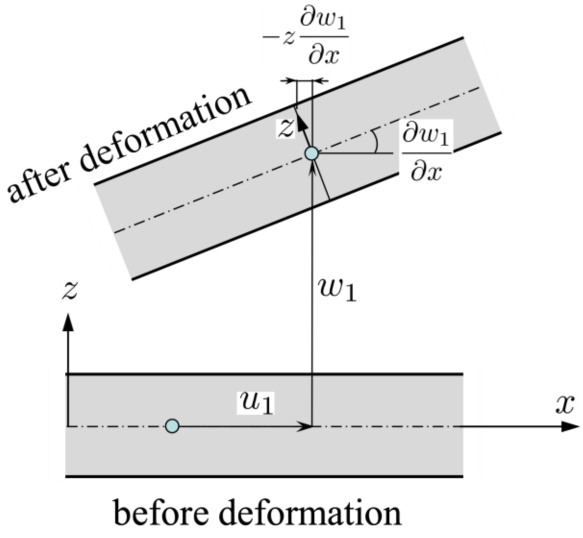

Fig.2.1.4 Flat shell deformation

As described above, the deformation of the flat shell problem is expressed by the sum of the plane stress and plate bending deformation.

Flat shell deformation = in-plane deformation + bending deformation

This relation is expressed as follows.

$$\begin{aligned} u &= \boxed{u_1} \boxed{- z\frac{\partial w_1}{\partial x}} \\ v &= \boxed{v_1} \boxed{- z\frac{\partial w_1}{\partial y}} \\ w &= \boxed{w_1} \end{aligned} \tag{2.1.7}$$

Here, v_1 is the displacement in the y direction. The displacement contained within the solid red line is the displacement due to the in-plane deformation, and the displacement contained within the blue solid line is the deformation due to the plate bending deformation. The sum of these displacements is the displacement of the flat shell problem proposed in this study.

2.2 Governing Equation and Hybrid-type Virtual Work

2.2.1 *Governing Equation*

Let $\Omega \subset \mathbb{R}^{\mathrm{n_{dim}}}$, with $(1 \leq \mathrm{n_{dim}} \leq 3)$, be the reference configuration of a continuum body with smooth boundary $\Gamma := \partial\Omega$ and closure $\overline{\Omega} := \Omega \cup \partial\Omega$. Here $\mathbb{R}^{\mathrm{n_{dim}}}$ is the $\mathrm{n_{dim}}$ dimensional Euclidean space.

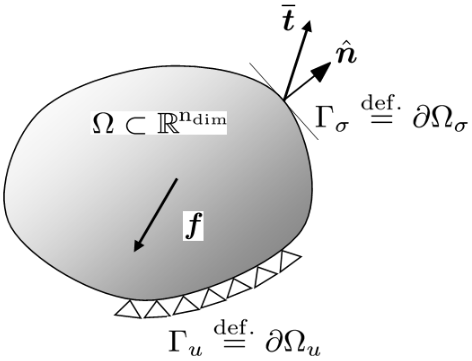

Fig.2.2.1. Reference configuration Ω and smooth boundary $\partial\Omega$

The local form of the equilibrium equation for a deformable body is obtained as

$$\mathrm{div}\boldsymbol{\sigma} + \boldsymbol{f} = 0 \text{ in } \Omega, \tag{2.2.1}$$

$$\boldsymbol{\sigma} = \boldsymbol{\sigma}^t \text{ in } \Omega, \tag{2.2.2}$$

where $\boldsymbol{f} : \Omega \to \mathbb{R}^{\mathrm{n_{dim}}}$ is the body force per unit volume, and $\boldsymbol{\sigma} : \overline{\Omega} \to \mathbb{S}$ is the Cauchy stress tensor. Here $\mathbb{S} = \mathbb{R}^{(\mathrm{n_{dim}}+1)\cdot\mathrm{n_{dim}}/2}$ is the vector space of the symmetric rank-two tensor, and $\boldsymbol{e}_i$ is the standard base vector of $\mathbb{R}^{\mathrm{n_{dim}}}$, such that the stress tensor becomes $\boldsymbol{\sigma} = \sigma_{ij}\boldsymbol{e}_i \otimes \boldsymbol{e}_j$, where $\otimes$ denotes a tensor product; $\boldsymbol{u} : \overline{\Omega} \to \mathbb{R}^{\mathrm{n_{dim}}}$ is a displacement field of particles with reference position $\boldsymbol{x} \in \Omega$. Define $\boldsymbol{u}(\boldsymbol{x})$ and denote the infinitesimal strain tensor by

$$\boldsymbol{\varepsilon} = \boldsymbol{\nabla}^s \boldsymbol{u} \overset{\mathrm{def.}}{=} \frac{1}{2}\left\{\boldsymbol{\nabla}\boldsymbol{u} + {}^t(\boldsymbol{\nabla}\boldsymbol{u})\right\} \tag{2.2.3}$$

where $\boldsymbol{\nabla} := (\partial/\partial x_i)\boldsymbol{e}_i$ is the differential vector operator, and $\boldsymbol{\nabla}^s$ shows the symmetry element of $\boldsymbol{\nabla}$. It is assumed that the boundary $\Gamma = \Gamma_u \cup \Gamma_\sigma$.

$$\overline{\Gamma} = \overline{\Gamma_u \cup \Gamma_\sigma} \ \ , \ \ \Gamma_u \cap \Gamma_\sigma = \emptyset \tag{2.2.4}$$

Here $\Gamma_u := \partial_u\Omega \subset \partial\Omega$, and the displacement is given as follows:

$$\boldsymbol{u}|_{\Gamma_u} = \overline{\boldsymbol{u}} \ \ \text{(given)} \tag{2.2.5}$$

However, $\Gamma_\sigma := \partial_\sigma \Omega \subset \partial\Omega$, and traction $\boldsymbol{t} := \boldsymbol{\sigma n}$ is prescribed as follows:

$$\boldsymbol{\sigma}|_{\Gamma_\sigma} \hat{\boldsymbol{n}} = \overline{\boldsymbol{t}} \ \ \text{(given)} \tag{2.2.6}$$

Here, $\hat{\boldsymbol{n}}$ is the outward normal vector on the boundary Γ_σ.

The constitutive equation to the elastic body is provided as follows by the use of the elasticity tensor $\boldsymbol{D}$:

$$\boldsymbol{\sigma} = \boldsymbol{D} : \boldsymbol{\varepsilon} \tag{2.2.7}$$

The constitutive equation of the three-dimensional problem is given as follows:

$$\begin{Bmatrix} \sigma_x \\ \sigma_y \\ \sigma_z \\ \tau_{xy} \\ \tau_{yz} \\ \tau_{zx} \end{Bmatrix} = \frac{E}{(1+\nu)(1-2\nu)} \begin{bmatrix} 1-\nu & \nu & \nu & 0 & 0 & 0 \\ \nu & 1-\nu & \nu & 0 & 0 & 0 \\ \nu & \nu & 1-\nu & 0 & 0 & 0 \\ 0 & 0 & 0 & \frac{(1-\nu)}{2} & 0 & 0 \\ 0 & 0 & 0 & 0 & \frac{(1-\nu)}{2} & 0 \\ 0 & 0 & 0 & 0 & 0 & \frac{(1-\nu)}{2} \end{bmatrix} \begin{Bmatrix} \varepsilon_x \\ \varepsilon_y \\ \varepsilon_z \\ \gamma_{xy} \\ \gamma_{yz} \\ \gamma_{zx} \end{Bmatrix} \tag{2.2.8}$$

2.2.2 *Virtual Work Equation (Weak Forms)*

Let the space of admissible displacement field be denoted by $\mathbb{U}$, defined as

$$\mathbb{U} \overset{\text{def.}}{=} \{\boldsymbol{u} : \Omega \to \mathbb{R}^{\mathrm{n_{dim}}} \mid \boldsymbol{u}|_{\Gamma_u} = \hat{\boldsymbol{u}}\} \tag{2.2.9}$$

Moreover, let the space of admissible virtual displacement field be denoted by $\mathbb{V}$, defined as

$$\mathbb{V} \overset{\text{def.}}{=} \{\delta\boldsymbol{u} : \Omega \to \mathbb{R}^{\mathrm{n_{dim}}} \mid \delta\boldsymbol{u}|_{\Gamma_u} = \boldsymbol{0}\} \tag{2.2.10}$$

Now, using Equation (2.2.1) and integrating the volume of the elastic body, the weak form of the static equilibrium of the elastic body is obtained as

$$\delta W := \int_\Omega (\operatorname{div} \boldsymbol{\sigma} + \boldsymbol{f}) \cdot \delta\boldsymbol{u}\, dV = 0 \quad {}^\forall \delta\boldsymbol{u} \in \mathbb{V} \tag{2.2.11}$$

It can further derive a more common and useful expression to give the divergence of the vector $\boldsymbol{\sigma}\delta\boldsymbol{u}$ as

$$\mathrm{div}(\boldsymbol{\sigma}\delta\boldsymbol{u}) = (\mathrm{div}\boldsymbol{\sigma}) \cdot \delta\boldsymbol{u} + \boldsymbol{\sigma} : \mathrm{grad}\ \delta\boldsymbol{u} \tag{2.2.12}$$

Using this equation together with the Gauss' theorem enables Equation (2.2.11) to be rewritten as

$$\int_{\Omega} \boldsymbol{\sigma} : \mathrm{grad}\delta\boldsymbol{u}\, dV - \int_{\Omega} \boldsymbol{f} \cdot \delta\boldsymbol{u} dV - \int_{\Gamma_\sigma} \bar{\boldsymbol{t}} \cdot \delta\boldsymbol{u}\, dS = 0 \quad {}^{\forall}\delta\boldsymbol{u} \in \mathbb{V} \tag{2.2.13}$$

This equation is a virtual work equation. If $\boldsymbol{u}$ is the weighing function, it implies a weak form. Moreover, $\mathbb{U} \subset \mathbb{H}^1(\Omega)$ and $\mathbb{V} \subset \mathbb{H}^1(\Omega)$, where $\mathbb{H}^1(\Omega)$ denotes the Sobolev space of a function possessing space integrable derivatives.

2.2.3 *Hybrid-type Virtual Work Equation*

Let Ω consist of *M* subdomains $\Omega^{(e)} \subset \Omega$ with the closed boundary $\Gamma^{(e)} := \partial\Omega^{(e)}$, as shown in Figure 2.2.2.

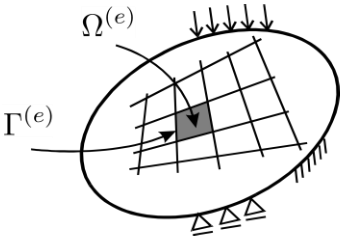

Fig.2.2.2 Subdomain $\Omega^{(e)}$ and its boundary $\Gamma^{(e)}$

We have,

$$\Omega = \bigcup_{e=1}^{M} \Omega^{(e)} \quad \Omega^{(r)} \cap \Omega^{(q)} = 0 \quad (r \neq q) \tag{2.2.14}$$

The closure $\overline{\Omega}^{(e)}$ is defined by the subdomain $\Omega^{(e)}$ and its boundary $\partial\Omega^{(e)}$ as

$$\overline{\Omega}^{(e)} := \Omega \cup \partial\Omega^{(e)} \tag{2.2.15}$$

As shown in Figure 2.2.3, the common boundary between the two adjacent subdomains $\Omega^{(a)}$ and $\Omega^{(b)}$ is defined as

$$\Gamma_{<ab>} := \Gamma^{(a)} \cap \Gamma^{(b)} \tag{2.2.16}$$

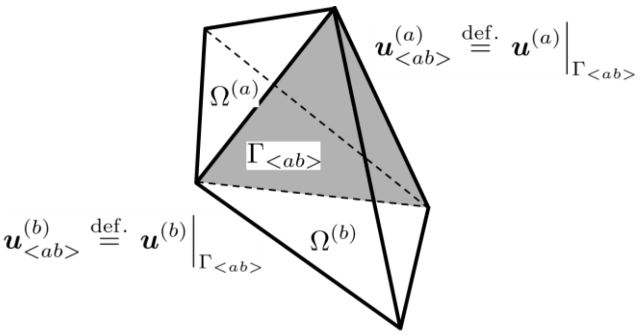

Fig.2.2.3 Common boundary $\Gamma_{<ab>}$ of subdomains $\Omega^{(a)}$ and $\Omega^{(b)}$

Suppose $\boldsymbol{u}^{(a)}_{<ab>}$ and $\boldsymbol{u}^{(b)}_{<ab>}$ are the displacements on $\Gamma_{<ab>}$, the intersection boundary, in the $\Omega^{(a)}$ and $\Omega^{(b)}$ subdomains, respectively; they are defined as

$$\boldsymbol{u}^{(a)}_{<ab>} \overset{\text{def.}}{=} \boldsymbol{u}^{(a)}\Big|_{\Gamma_{<ab>}} \tag{2.2.17a}$$

$$\boldsymbol{u}^{(b)}_{<ab>} \overset{\text{def.}}{=} \boldsymbol{u}^{(b)}\Big|_{\Gamma_{<ab>}} \tag{2.2.17b}$$

They have the following relationship:

$$\boldsymbol{u}^{(a)}_{<ab>} = \boldsymbol{u}^{(b)}_{<ab>} \ \text{ on } \ \Gamma_{<ab>} \tag{2.2.18}$$

This introduces the subsidiary condition into the framework of the variational Equation (2.2.13) with Lagrange multipliers $\boldsymbol{\lambda}$ as

$$H_{<ab>} \overset{\text{def.}}{=} \delta \int_{\Gamma_{<ab>}} \boldsymbol{\lambda}\cdot(\boldsymbol{u}^{(a)}_{<ab>} - \boldsymbol{u}^{(b)}_{<ab>})\, dS \tag{2.2.19}$$

Here, $\delta(\bullet)$ shows the variation of $(\bullet)$.

As described above, the hybrid-type virtual work equation with respect to the *M* subdomain and *N* intersection boundary is the following:

$$\begin{aligned}
&\sum_{e=1}^{M} \delta W^{(e)} + \sum_{s=1}^{N} H_{<s>} = \\
&\quad \sum_{e=1}^{M} \left(\int_{\Omega^{(e)}} \boldsymbol{\sigma} : \text{grad}\delta\boldsymbol{u}\, dV - \int_{\Omega^{(e)}} \boldsymbol{f}\cdot\delta\boldsymbol{u} dV - \int_{\Gamma^{(e)}} \boldsymbol{t}\cdot\delta\boldsymbol{u}\, dS \right) \\
&\qquad\qquad - \sum_{s=1}^{N} \left(\delta \int_{\Gamma_{<s>}} \boldsymbol{\lambda}\cdot(\boldsymbol{u}^{(a)}_{<ab>} - \boldsymbol{u}^{(b)}_{<ab>})\, dS \right) = 0 \quad {}^{\forall}\delta\boldsymbol{u} \in \mathbb{V}
\end{aligned} \tag{2.2.20}$$

2.2.4 *Physical Meaning of Lagrange Multiplier*

Equation (2.2.20) is expanded as follows:

$$\int_{\Omega^{(a)}} \boldsymbol{\sigma} : \mathrm{grad}\delta\boldsymbol{u}\; dV + \cdots + \int_{\Omega^{(b)}} \boldsymbol{\sigma} : \mathrm{grad}\delta\boldsymbol{u}\; dV$$

$$- \int_{\Gamma_{<ab>}} \Big[(\boldsymbol{t}^{(a)} - \lambda)\delta\boldsymbol{u}^{(a)} - (\boldsymbol{t}^{(b)} + \lambda)\delta\boldsymbol{u}^{(b)}$$

$$+ (\boldsymbol{u}^{(a)}_{<ab>} - \boldsymbol{u}^{(b)}_{<ab>})\delta\lambda\; dS \Big] + \cdots = 0 \qquad (2.2.21)$$

Therefore, physical meaning of the Lagrange multiplier $\boldsymbol{\lambda}$ is equivalent to the surface force on the intersection boundary $\Gamma_{<ab>}$. That is,

$$\boldsymbol{\lambda} = \boldsymbol{t}^{(a)} = -\boldsymbol{t}^{(b)} \qquad (2.2.22)$$

Here, $\boldsymbol{t}^{(a)}$ and $\boldsymbol{t}^{(b)}$ represent the surface forces on intersection boundary $\Gamma_{<ab>}$ at subdomains $\Omega^{(a)}$ and $\Omega^{(b)}$, respectively.

2.3 Discretization of Flat Shell Problems

2.3.1 *Definition of Local Coordinate System*

In this study, a local coordinate system was set up for each subdomain, and a displacement field within the domain was assumed based on it. The local coordinate system for each subdomain is described here.

Figure 2.3.1 shows the global coordinate system $X - Y - Z$ with respect to the analysis domain, and the coordinate system $X' - Y' - Z'$ moves parallel to any vertex of the triangular shaped subdomain.

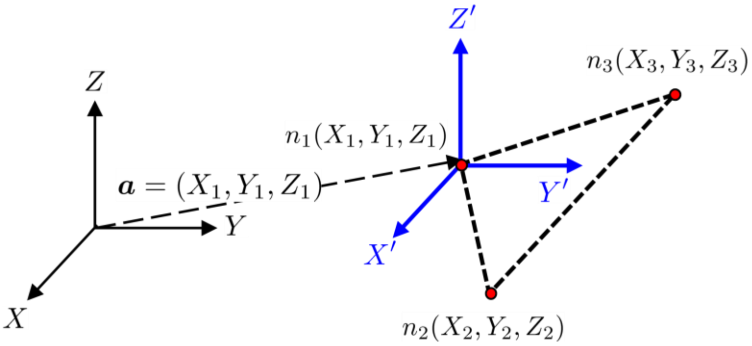

Fig.2.3.1 Parallel translation of the global coordinate system

At this time, the transformation matrix in the affine transformation is expressed as follows:

$$\boldsymbol{X}' = \boldsymbol{R}_{\mathrm{m}} \cdot \boldsymbol{X} \tag{2.3.1}$$

$$\begin{Bmatrix} X' \\ Y' \\ Z' \\ 1 \end{Bmatrix} = \begin{bmatrix} 1 & 0 & 0 & -X_1 \\ 0 & 1 & 0 & -Y_1 \\ 0 & 0 & 1 & -Z_1 \\ 0 & 0 & 0 & 1 \end{bmatrix} \begin{Bmatrix} X \\ Y \\ Z \\ 1 \end{Bmatrix} \tag{2.3.2}$$

Next, as shown in Fig. 2.3.2, the X' axis of this coordinate system is rotated such that it coincides with one side of the subdomain. At this time, the X' axis coincides with the x' axis. In addition, the z' axis is rotated such as to face the normal direction of the subdomain. As a result, the plane formed by the x' and y' axes coincides with the plane of the subdomain.

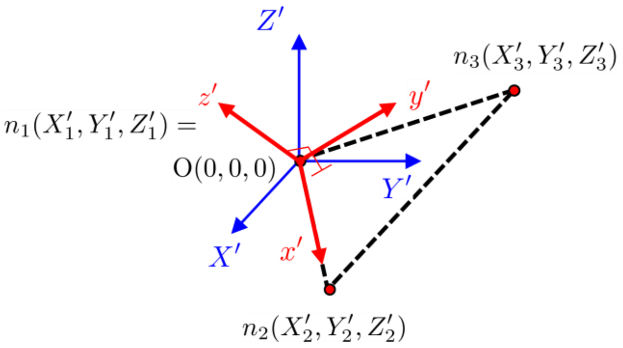

Fig.2.3.2 Rotation of axes with respect to the local coordinate system $x' - y' - z'$

This $x' - y' - z'$ coordinate system is calculated by the affine transformation as follows:

$$\boldsymbol{x}' = \boldsymbol{R}_{\mathrm{e}} \cdot \boldsymbol{X}' \tag{2.3.3}$$

It is expressed as a component using the direction cosine as follows:

$$\begin{Bmatrix} x' \\ y' \\ z' \\ 1 \end{Bmatrix} = \begin{bmatrix} l_1 & m_1 & n_1 & 0 \\ l_2 & m_2 & n_2 & 0 \\ l_3 & m_3 & n_3 & 0 \\ 0 & 0 & 0 & 1 \end{bmatrix} \begin{Bmatrix} X' \\ Y' \\ Z' \\ 1 \end{Bmatrix} \tag{2.3.4}$$

Here, each component is defined as follows:

$$L = \sqrt{(X'_2)^2 + (Y'_2)^2 + (Z'_2)^2} \quad 2A = \sqrt{\begin{vmatrix} Y'_2 & Z'_2 \\ Y'_3 & Z'_3 \end{vmatrix}^2 + \begin{vmatrix} Z'_2 & X'_2 \\ Z'_3 & X'_3 \end{vmatrix}^2 + \begin{vmatrix} X'_2 & Y'_2 \\ X'_3 & Y'_3 \end{vmatrix}^2}$$

$$l_1 = \frac{X'_2}{L} \qquad l_2 = \frac{1}{2AL}\left(Z'_2 \begin{vmatrix} Z'_2 & X'_2 \\ Z'_3 & X'_3 \end{vmatrix} - Y'_2 \begin{vmatrix} X'_2 & Y'_2 \\ X'_3 & Y'_3 \end{vmatrix} \right) \qquad l_3 = \frac{1}{2A} \begin{vmatrix} Y'_2 & Z'_2 \\ Y'_3 & Z'_3 \end{vmatrix}$$

$$m_1 = \frac{Y'_2}{L} \qquad m_2 = \frac{1}{2AL}\left(X'_2 \begin{vmatrix} X'_2 & Y'_2 \\ X'_3 & Y'_3 \end{vmatrix} - X'_2 \begin{vmatrix} Y'_2 & Z'_2 \\ Y'_3 & Z'_3 \end{vmatrix} \right) \qquad m_3 = \frac{1}{2A} \begin{vmatrix} Z'_2 & X'_2 \\ Z'_3 & X'_3 \end{vmatrix}$$

$$n_1 = \frac{Z'_2}{L} \qquad n_2 = \frac{1}{2AL}\left(Y'_2 \begin{vmatrix} Y'_2 & Z'_2 \\ Y'_3 & Z'_3 \end{vmatrix} - X'_2 \begin{vmatrix} Z'_2 & X'_2 \\ Z'_3 & X'_3 \end{vmatrix} \right) \qquad n_3 = \frac{1}{2A} \begin{vmatrix} X'_2 & Y'_2 \\ X'_3 & Y'_3 \end{vmatrix}$$

By moving the $x' - y' - z'$ coordinate system to the centroid of the subdomain as shown in

Figure 2.3.3, an independent local coordinate system is determined in each subdomain.

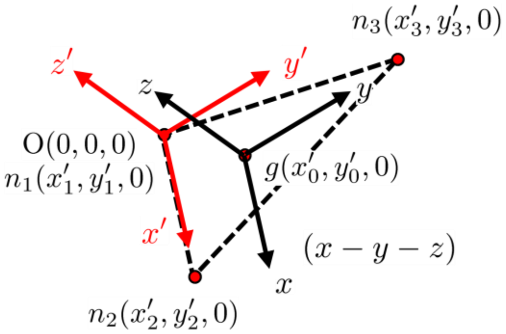

Fig.2.3.3 Parallel translation to the local coordinate system $x-y-z$

The affine transformation related to this translation is obtained as

$$\boldsymbol{x} = \boldsymbol{R}_g \cdot \boldsymbol{x}' \tag{2.3.5}$$

$$\begin{Bmatrix} x \\ y \\ z \\ 1 \end{Bmatrix} = \begin{bmatrix} 1 & 0 & 0 & -x'_0 \\ 0 & 1 & 0 & -y'_0 \\ 0 & 0 & 1 & -z'_0 \\ 0 & 0 & 0 & 1 \end{bmatrix} \begin{Bmatrix} x' \\ y' \\ z' \\ 1 \end{Bmatrix}, \tag{2.3.6}$$

Here,

$$x'_0 = \frac{1}{3}(x'_1 + x'_2 + x'_3)$$

$$y'_0 = \frac{1}{3}(y'_1 + y'_2 + y'_3)$$

$$z'_0 = 0$$

Consequently, the local coordinate system in the subdomain is as shown in Figure 2.3.4.

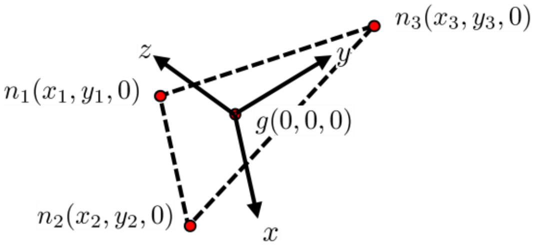

Fig.2.3.4 Local coordinate system in a subdomain

The composite transformation from the global coordinate system to the local coordinate system is as follows:

$$\boldsymbol{x} = \boldsymbol{R}_g \cdot \boldsymbol{R}_{\mathrm{e}} \cdot \boldsymbol{R}_{\mathrm{m}} \cdot \boldsymbol{X} = \boldsymbol{R}_x \cdot \boldsymbol{X} \tag{2.3.7}$$

2.3.2 *Second-order Displacement Field*

A three-dimensional displaced field $\boldsymbol{u} \in \mathbb{U}$ with $n_{\mathrm{dim}} = 3$ is now considered. Here, $\mathbb{U}$ is the space of admissible displacement field shown in Equation (2.2.9). It carries out Taylor's expansion of this displacement $\boldsymbol{u}(\boldsymbol{x})$ about the point $\boldsymbol{x}_0 = (0,0,0) \in \Omega^{(e)}$ in a domain $\Omega^{(e)}$ as follows:

$$\begin{aligned} \boldsymbol{u}^{(e)} &= \boldsymbol{u}_0 + x\boldsymbol{u}_x^0 + y\boldsymbol{u}_y^0 + z\boldsymbol{u}_z^0 \\ &\quad + \frac{1}{2}x^2\boldsymbol{u}_{xx}^0 + \frac{1}{2}y^2\boldsymbol{u}_{yy}^0 + \frac{1}{2}z^2\boldsymbol{u}_{zz}^0 + xy\boldsymbol{u}_{xy}^0 + yz\boldsymbol{u}_{yz}^0 + zx\boldsymbol{u}_{zx}^0 + \cdots \end{aligned} \tag{2.3.8}$$

The symbols and their meanings are given below.

$$\begin{gathered} (\bullet)_x = \frac{\partial}{\partial x}(\bullet) \;\;,\;\; (\bullet)_y = \frac{\partial}{\partial y}(\bullet) \;\;,\;\; (\bullet)_z = \frac{\partial}{\partial z}(\bullet) \\ (\bullet)_{xx} = \frac{\partial^2}{\partial x^2}(\bullet) \;\;,\;\; (\bullet)_{yy} = \frac{\partial^2}{\partial y^2}(\bullet) \;\;,\;\; (\bullet)_{zz} = \frac{\partial^2}{\partial z^2}(\bullet) \\ (\bullet)_{xy} = \frac{\partial^2}{\partial x \partial y}(\bullet) \;\;,\;\; (\bullet)_{yz} = \frac{\partial^2}{\partial y \partial z}(\bullet) \;\;,\;\; (\bullet)_{zx} = \frac{\partial^2}{\partial z \partial x}(\bullet) \end{gathered}$$

Here, $(\bullet)_0$ indicates the value of the physical quantity in the point $\boldsymbol{x}_0$. The stress analysis often needs to check the strain and stress; therefore, it is convenient that the rigid-displacement, strain, and slope of strain are the unknowns in the displacement field. Denoting the component of the displacement in the x, y, and z directions by u, v, and w, respectively, the strain and its derivative are given by

$$\frac{1}{2}(w_y - v_z) = \theta_x,\ \frac{1}{2}(u_z - w_x) = \theta_y,\ \frac{1}{2}(v_x - u_y) = \theta_z$$

$$u_x = \varepsilon_x,\ v_y = \varepsilon_y,\ w_z = \varepsilon_z$$

$$\frac{1}{2}(u_y + v_x) = \gamma_{xy},\ \frac{1}{2}(v_z + w_y) = \gamma_{yz},\ \frac{1}{2}(w_x + u_z) = \gamma_{zx}$$

$$u_{xx} = (\varepsilon_x)_x,\ u_{xy} = (\varepsilon_x)_y,\ u_{xz} = (\varepsilon_x)_z$$

$$v_{yy} = (\varepsilon_y)_y,\ v_{yx} = (\varepsilon_y)_x,\ v_{yz} = (\varepsilon_y)_z$$

$$w_{zz} = (\varepsilon_z)_z, w_{zx} = (\varepsilon_z)_x, w_{zy} = (\varepsilon_z)_y$$

$$(u_y + v_x)_x = (\gamma_{xy})_x, (v_z + w_y)_x = (\gamma_{yz})_x, (w_x + u_z)_x = (\gamma_{zx})_x$$

$$(u_y + v_x)_y = (\gamma_{xy})_y, (v_z + w_y)_y = (\gamma_{yz})_y, (w_x + u_z)_y = (\gamma_{zx})_y$$

$$(u_y + v_x)_z = (\gamma_{xy})_z, (v_z + w_y)_z = (\gamma_{yz})_z, (w_x + u_z)_z = (\gamma_{zx})_z$$

Now, the three-dimensional quadratic displacement field in the local coordinate system can be expressed as follows:

$$\begin{aligned} u = {} & u_0 + z\theta_y - y\theta_z + x\varepsilon_x + \frac{1}{2}y\gamma_{xy} + \frac{1}{2}z\gamma_{zx} + \frac{1}{2}x^2\varepsilon_{x,x} - \frac{1}{2}y^2\varepsilon_{y,x} - \frac{1}{2}z^2\varepsilon_{z,x} + xy\varepsilon_{x,y} + zx\varepsilon_{x,z} \\ & -\frac{1}{2}yz\gamma_{yz,x} + \frac{1}{2}y^2\gamma_{xy,y} + \frac{1}{2}yz\gamma_{zx,y} + \frac{1}{2}z^2\gamma_{zx,z} + \frac{1}{2}yz\gamma_{xy,z} \end{aligned} \tag{2.3.9}$$

$$\begin{aligned} v = {} & v_0 + x\theta_z - z\theta_x + y\varepsilon_y + \frac{1}{2}z\gamma_{yz} + \frac{1}{2}x\gamma_{xy} + \frac{1}{2}y^2\varepsilon_{y,y} - \frac{1}{2}z^2\varepsilon_{z,y} - \frac{1}{2}x^2\varepsilon_{x,y} + yz\varepsilon_{y,z} + xy\varepsilon_{y,x} \\ & -\frac{1}{2}zx\gamma_{zx,y} + \frac{1}{2}z^2\gamma_{yz,z} + \frac{1}{2}zx\gamma_{xy,z} + \frac{1}{2}x^2\gamma_{xy,x} + \frac{1}{2}zx\gamma_{yz,x} \end{aligned} \tag{2.3.10}$$

$$\begin{aligned} w = {} & w_0 + y\theta_x - x\theta_y + z\varepsilon_z + \frac{1}{2}x\gamma_{zx} + \frac{1}{2}y\gamma_{yz} + \frac{1}{2}z^2\varepsilon_{z,z} - \frac{1}{2}x^2\varepsilon_{x,z} - \frac{1}{2}y^2\varepsilon_{y,z} + zx\varepsilon_{z,x} + yz\varepsilon_{z,y} \\ & -\frac{1}{2}xy\gamma_{xy,z} + \frac{1}{2}x^2\gamma_{zx,x} + \frac{1}{2}xy\gamma_{yz,x} + \frac{1}{2}y^2\gamma_{yz,y} + \frac{1}{2}xy\gamma_{zx,y} \end{aligned} \tag{2.3.11}$$

In this study, the flat shell problem is analyzed by superimposing the plane stress state upon the plate bending state. A second-order displacement field is used as the in-plane displacement field. The degree of freedom of the in-plane problem is shown in Figure 2.3.5.

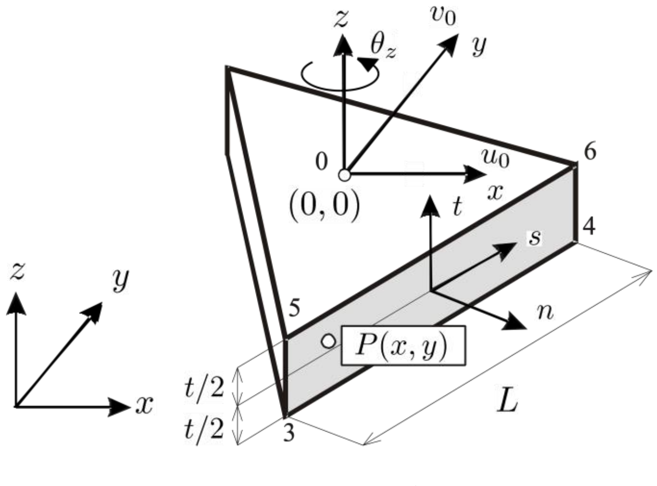

Fig.2.3.5 Rigid displacement of in-plane element

Now, the displacement field of the in-plane problem is obtained, as follows, from Equations (2.3.9) and (2.3.10) for the three-dimensional displacement field.

$$u = u_0 - y\theta_{z0} + x\varepsilon_x + \frac{1}{2}y\gamma_{xy} + \frac{1}{2}x^2\varepsilon_{x,x} - \frac{1}{2}y^2\varepsilon_{y,x} + xy\varepsilon_{x,y} + \frac{1}{2}y^2\gamma_{xy,y} \tag{2.3.12}$$

$$v = v_0 + x\theta_{z0} + y\varepsilon_y + \frac{1}{2}x\gamma_{xy} + xy\varepsilon_{y,x} + \frac{1}{2}x^2\gamma_{xy,x} - \frac{1}{2}x^2\varepsilon_{x,y} + \frac{1}{2}y^2\varepsilon_{y,y} \tag{2.3.13}$$

In the flat plate problem, to express deflection, it is necessary to assume a displacement field of a second order or higher. In this study, the second-order displacement field with the lowest order is assumed as the deflection. The degree of freedom of the out-of-plane problem is shown in Figure 2.3.6.

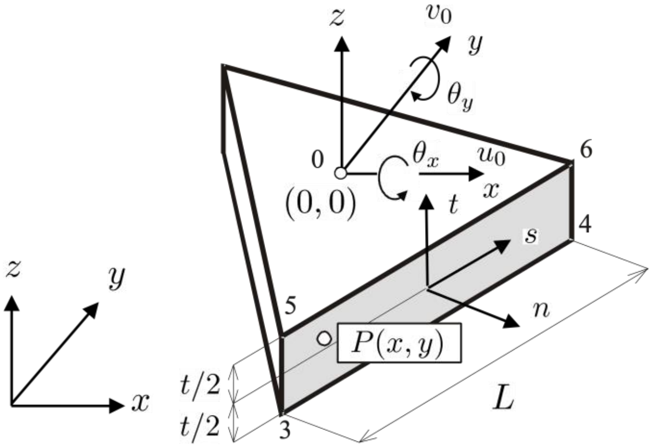

Fig.2.3.6 Rigid displacement of an out-of-plane element

In the out-of-plane problem to which the Kirchhoff's assumption is applied, the order required for the deflection is two or more. In this study, the second-order displacement field is assumed. Now, the displacement field of the out-of-plane problem is obtained, as follows, from Equation (2.3.11) for the three-dimensional displacement field.

$$w = w_0 + y\theta_x - x\theta_y - \frac{1}{2}x^2\varepsilon_{x,z} - \frac{1}{2}y^2\varepsilon_{y,z} - \frac{1}{2}xy\gamma_{xy,z} \tag{2.3.14}$$

Thus, the degrees of freedom of rigid body displacement of the flat plate shell element in the local coordinate system provided for each subdomain are shown in Figure 2.3.7.

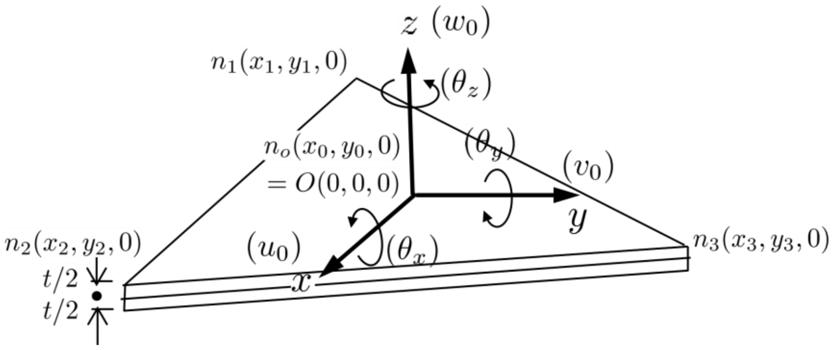

Fig.2.3.7 Rigid displacement of a flat shell element

Therefore, the degree of freedom of the flat shell $\boldsymbol{U}^{(e)}$ is as follows:

$$\boldsymbol{U}^{(e)} = \lfloor \boldsymbol{d}, \boldsymbol{\theta}, \boldsymbol{\varepsilon}, \boldsymbol{\varepsilon}_x, \boldsymbol{\varepsilon}_y, \boldsymbol{\varepsilon}_z \rfloor^t \tag{2.3.15}$$

Here, $\boldsymbol{d}$, $\boldsymbol{\theta}$, $\boldsymbol{\varepsilon}$ denote a rigid body displacement vector, rigid body rotation vector, and strain vector, respectively. Also, $\boldsymbol{\varepsilon}_x$, $\boldsymbol{\varepsilon}_y$, $\boldsymbol{\varepsilon}_z$ are the gradients of strain.

$$\boldsymbol{d} = \lfloor u_0, v_0, w_0 \rfloor^t$$

$$\boldsymbol{\theta} = \lfloor \theta_x, \theta_y, \theta_z \rfloor^t$$

$$\boldsymbol{\varepsilon} = \lfloor \varepsilon_x, \varepsilon_y, \gamma_{xy} \rfloor^t$$

$$\boldsymbol{\varepsilon}_x = \lfloor \varepsilon_{x,x}, \varepsilon_{y,x}, \gamma_{xy,x} \rfloor^t$$

$$\boldsymbol{\varepsilon}_y = \lfloor \varepsilon_{x,y}, \varepsilon_{y,y}, \gamma_{xy,y} \rfloor^t$$

$$\boldsymbol{\varepsilon}_z = \lfloor \varepsilon_{x,z}, \varepsilon_{y,z}, \gamma_{xy,z} \rfloor^t$$

Further, the displacement of an arbitrary point on the neutral plane, with respect to the plate thickness direction, in the subdomain is expressed as follows:

$$\boldsymbol{u}^{(e)} = \boldsymbol{N}^{(e)} \boldsymbol{U}^{(e)} \tag{2.3.16}$$

$$\boldsymbol{u}^{(e)} = \lfloor u, v, w \rfloor^t$$

$$\boldsymbol{N}^{(e)} = \lfloor \boldsymbol{N}_d^{(e)}, \boldsymbol{N}_\theta^{(e)}, \boldsymbol{N}_\varepsilon^{(e)}, \boldsymbol{N}_{\varepsilon_\mathrm{x}}^{(e)}, \boldsymbol{N}_{\varepsilon_\mathrm{y}}^{(e)}, \boldsymbol{N}_{\varepsilon_\mathrm{z}}^{(e)} \rfloor^t$$

$$\boldsymbol{N}_d^{(e)} = \begin{bmatrix} 1 & 0 & 0 \\ 0 & 1 & 0 \\ 0 & 0 & 1 \end{bmatrix}, \boldsymbol{N}_\theta^{(e)} = \begin{bmatrix} 0 & 0 & -y \\ 0 & 0 & x \\ y & -x & 0 \end{bmatrix}, \boldsymbol{N}_\varepsilon^{(e)} = \begin{bmatrix} X & 0 & Y/2 \\ 0 & Y & X/2 \\ 0 & 0 & 0 \end{bmatrix}$$

$$\boldsymbol{N}_{\varepsilon_{\mathrm{x}}}^{(e)} = \begin{bmatrix} x^2/2 & -y^2/2 & 0 \\ 0 & xy & x^2/2 \\ 0 & 0 & 0 \end{bmatrix}, \boldsymbol{N}_{\varepsilon_{\mathrm{y}}}^{(e)} = \begin{bmatrix} XY & 0 & Y^2/2 \\ -X^2/2 & Y^2/2 & 0 \\ 0 & 0 & 0 \end{bmatrix}$$

$$\boldsymbol{N}_{\varepsilon_{\mathrm{z}}}^{(e)} = \begin{bmatrix} 0 & 0 & 0 \\ 0 & 0 & 0 \\ -x^2/2 & -y^2/2 & -xy/2 \end{bmatrix}$$

2.3.3 *Element Stress and Moment*

(1) In-plane problem

The displacement field in the in-plane problem is expressed by Equations (2.3.12) and (2.3.13). These can be simply expressed as follows:

$$\boldsymbol{u}_{\mathrm{i}}^{(e)} = \boldsymbol{N}_{\mathrm{i}}^{(e)} \boldsymbol{U}^{(e)} \tag{2.3.17}$$

$$\boldsymbol{u}_{\mathrm{i}}^{(e)} = \lfloor u, v, w \rfloor^t$$

$$\boldsymbol{N}_{\mathrm{i}}^{(e)} = \lfloor \boldsymbol{N}_{d\mathrm{i}}, \boldsymbol{N}_{\theta\mathrm{i}}, \boldsymbol{N}_{\varepsilon\mathrm{i}}, \boldsymbol{N}_{\varepsilon_x\mathrm{i}}, \boldsymbol{N}_{\varepsilon_y\mathrm{i}}, \boldsymbol{N}_{\varepsilon_z\mathrm{i}} \rfloor^t$$

$$\boldsymbol{N}_{d\mathrm{i}}^{(e)} = \begin{bmatrix} 1 & 0 & 0 \\ 0 & 1 & 0 \\ 0 & 0 & 0 \end{bmatrix}, \boldsymbol{N}_{\theta\mathrm{i}}^{(e)} = \begin{bmatrix} 0 & 0 & -y \\ 0 & 0 & x \\ 0 & 0 & 0 \end{bmatrix}, \boldsymbol{N}_{\varepsilon\mathrm{i}}^{(e)} = \begin{bmatrix} x & 0 & y/2 \\ 0 & y & x/2 \\ 0 & 0 & 0 \end{bmatrix}$$

$$\boldsymbol{N}_{\varepsilon_{\mathrm{x}}\mathrm{i}}^{(e)} = \begin{bmatrix} x^2/2 & -y^2/2 & 0 \\ 0 & xy & x^2/2 \\ 0 & 0 & 0 \end{bmatrix}, \boldsymbol{N}_{\varepsilon_{\mathrm{y}}\mathrm{i}}^{(e)} = \begin{bmatrix} xy & 0 & y^2/2 \\ -x^2/2 & y^2/2 & 0 \\ 0 & 0 & 0 \end{bmatrix}, \boldsymbol{N}_{\varepsilon_{\mathrm{z}}\mathrm{i}}^{(e)} = \begin{bmatrix} 0 & 0 & 0 \\ 0 & 0 & 0 \\ 0 & 0 & 0 \end{bmatrix}$$

The strain for the plane stress state in subdomain $\Omega^{(e)}$ (element e) can be expressed, as follows, using Equation (2.3.17).

$$\boldsymbol{\varepsilon}_{\mathrm{i}}^{(e)} = \boldsymbol{\partial} \boldsymbol{u}_{\mathrm{i}}^{(e)} = \boldsymbol{\partial} \boldsymbol{N}_{\mathrm{i}}^{(e)} \boldsymbol{U}^{(e)} = \boldsymbol{B}_{\mathrm{i}}^{(e)} \boldsymbol{U}^{(e)} \tag{2.3.18}$$

Here, the components of each matrix are defined as

$$\boldsymbol{\varepsilon}_{\mathrm{i}}^{(e)} = \lfloor \varepsilon_x^{(e)}, \varepsilon_y^{(e)}, \gamma_{xy}^{(e)} \rfloor^t$$

$$\boldsymbol{\partial}^t = \begin{bmatrix} \dfrac{\partial}{\partial x} & 0 & \dfrac{\partial}{\partial y} \\ 0 & \dfrac{\partial}{\partial y} & \dfrac{\partial}{\partial x} \\ 0 & 0 & 0 \end{bmatrix}$$

$$\boldsymbol{B}_{\mathrm{i}}^{(e)}=\left[\begin{array}{ccc|ccc|ccc|ccc|ccc|ccc} 0&0&0&0&0&0&1&0&0&x&0&0&y&0&0&0&0&0\\ 0&0&0&0&0&0&0&1&0&0&x&0&0&y&0&0&0&0\\ 0&0&0&0&0&0&0&0&1&0&0&x&0&0&y&0&0&0 \end{array}\right]$$

Thus, in the displacement field used in this study, the strain distribution in a subdomain (element) is represented by a linear function. This is equivalent to the second-order element in the finite element method.

The stress–strain relationship in the case of plane stress state is derived, as follows, for the stress–strain relationship (2.2.7) in the three-dimensional problem:

$$\boldsymbol{\sigma}_{\mathrm{i}}^{(e)}=\boldsymbol{D}^{(e)}\boldsymbol{\varepsilon}_{\mathrm{i}}^{(e)}, \tag{2.3.19}$$

where

$$\boldsymbol{\sigma}_{\mathrm{i}}^{(e)}=\lfloor \sigma_x^{(e)},\sigma_y^{(e)},\tau_{xy}^{(e)}\rfloor^t.$$

In addition, $\boldsymbol{D}^{(e)}$ represents a constitutive matrix for plane stress state, which can be expressed by the following equation using Poisson ratio ν and elastic modulus E.

$$\boldsymbol{D}^{(e)}=\frac{E}{1-\nu^2}\begin{bmatrix} 1 & \nu & 0\\ \nu & 1 & 0\\ 0 & 0 & \dfrac{1-\nu}{2} \end{bmatrix}$$

(2) Out-of-plane problem

The strain–displacement equation for a three-dimensional problem is given by

$$\varepsilon_x=\frac{\partial u}{\partial x}\ ,\ \varepsilon_y=\frac{\partial v}{\partial y}\ ,\ \varepsilon_z=\frac{\partial w}{\partial z}$$

$$\gamma_{xy}=\frac{1}{2}\left(\frac{\partial u}{\partial y}+\frac{\partial v}{\partial x}\right)\ ,\ \gamma_{yz}=\frac{1}{2}\left(\frac{\partial v}{\partial z}+\frac{\partial w}{\partial y}\right)\ ,\ \gamma_{zx}=\frac{1}{2}\left(\frac{\partial w}{\partial x}+\frac{\partial u}{\partial z}\right)$$

Applying Kirchhoff's assumption to this relation, the strain–displacement relation for plate bending problems is obtained as follows:

$$\varepsilon_x=\frac{\partial u}{\partial x}\ ,\ \varepsilon_y=\frac{\partial v}{\partial y}\ ,\ \varepsilon_z=0$$

$$\frac{\partial u}{\partial z} = -\frac{\partial w}{\partial x} \ , \ \frac{\partial v}{\partial z} = -\frac{\partial w}{\partial y} \ , \ \gamma_{xy} = \frac{\partial v}{\partial x} + \frac{\partial u}{\partial y}$$

Integrating both sides of these equations with respect to z gives the following relationship:

$$u = -z\frac{\partial w}{\partial x} + u_c(x,y) \tag{2.3.20}$$

$$v = -z\frac{\partial w}{\partial y} + v_c(x,y) \tag{2.3.21}$$

Where u_c , v_c are the integral constants. In Kirchhoff's assumption, the neutral surface is an inextensible deformation; therefore, the integral constant is zero if the rigid body movement is zero. Consequently, the following relationship is obtained:

$$u = -z\frac{\partial w}{\partial x} \tag{2.3.22}$$

$$v = -z\frac{\partial w}{\partial y} \tag{2.3.23}$$

Applying the deflection expressed by Equation (2.3.14) to Equations (2.3.22) and (2.3.23) gives the following relationship:

$$u = -z\frac{\partial w}{\partial x} = z\left(\theta_{y_0} + x\varepsilon_{x,z} + \frac{y}{2}\gamma_{xy,z}\right) \tag{2.3.24}$$

$$v = -z\frac{\partial w}{\partial y} = z\left(-\theta_{x_0} + y\varepsilon_{y,z} + \frac{x}{2}\gamma_{xy,z}\right) \tag{2.3.25}$$

Therefore, the displacement field of the out-of-plane problem is

$$\boldsymbol{u}_{\mathrm{b}}^{(e)} = \boldsymbol{Z}\boldsymbol{N}_{\mathrm{b}}^{(e)}\boldsymbol{U}^{(e)} \tag{2.3.26}$$

$$\boldsymbol{u}_{\mathrm{b}}^{(e)} = \lfloor u, v, w \rfloor^t$$

$$\boldsymbol{N}_{\mathrm{b}}^{(e)} = \lfloor \boldsymbol{N}_{d\mathrm{b}}, \boldsymbol{N}_{\theta\mathrm{b}}, \boldsymbol{N}_{\varepsilon\mathrm{b}}, \boldsymbol{N}_{\varepsilon_x\mathrm{b}}, \boldsymbol{N}_{\varepsilon_y\mathrm{b}}, \boldsymbol{N}_{\varepsilon_z\mathrm{b}} \rfloor^t$$

$$\boldsymbol{N}_{\mathrm{db}}^{(e)} = \begin{bmatrix} 0 & 0 & 0 \\ 0 & 0 & 0 \\ 0 & 0 & 1 \end{bmatrix}, \boldsymbol{N}_{\theta\mathrm{b}}^{(e)} = \begin{bmatrix} 0 & 1 & 0 \\ -1 & 0 & 0 \\ y & -x & 0 \end{bmatrix}, \boldsymbol{N}_{\varepsilon_{\mathrm{b}}}^{(e)} = \begin{bmatrix} x & 0 & y/2 \\ 0 & y & x/2 \\ -x^2/2 & -y^2/2 & -xy/2 \end{bmatrix}$$

$$\boldsymbol{Z} = \begin{bmatrix} z & 0 & 0 \\ 0 & z & 0 \\ 0 & 0 & 1 \end{bmatrix}, \boldsymbol{N}_{\varepsilon\mathrm{b}}, = \boldsymbol{N}_{\varepsilon_x\mathrm{b}}, = \boldsymbol{N}_{\varepsilon_y\mathrm{b}}, = \boldsymbol{O}$$

Substituting Equations (2.3.22) and (2.3.23) into the strain–displacement relationship, the strain is represented by the deflection w, as follows:

$$\varepsilon_x = -z\frac{\partial^2 w}{\partial x^2} \tag{2.3.27}$$

$$\varepsilon_y = -z\frac{\partial^2 w}{\partial y^2} \tag{2.3.28}$$

$$\gamma_{xy} = -2z\frac{\partial^2 w}{\partial x \partial y} \tag{2.3.29}$$

Substituting the relation of Equation (2.3.26) into Equations (2.3.27)–(2.3.29), the strain in the subdomain $\Omega^{(e)}$ of the out-of-plane problem can be similarly expressed as follows:

$$\boldsymbol{\varepsilon}_{\mathrm{b}}^{(e)} = z\boldsymbol{B}_{\mathrm{b}}^{(e)}\boldsymbol{U}^{(e)} \tag{2.3.30}$$

$$\boldsymbol{\varepsilon}_{\mathrm{b}}^{(e)} = \lfloor \varepsilon_x^{(e)}, \varepsilon_y^{(e)}, \gamma_{xy}^{(e)} \rfloor^t$$

$$\boldsymbol{B}_{\mathrm{b}}^{(e)} = \left[\begin{array}{ccc|ccc|ccc|ccc|ccc|ccc} 0 & 0 & 0 & 0 & 0 & 0 & 0 & 0 & 0 & 0 & 0 & 0 & 0 & 0 & 0 & 1 & 0 & 0 \\ 0 & 0 & 0 & 0 & 0 & 0 & 0 & 0 & 0 & 0 & 0 & 0 & 0 & 0 & 0 & 0 & 1 & 0 \\ 0 & 0 & 0 & 0 & 0 & 0 & 0 & 0 & 0 & 0 & 0 & 0 & 0 & 0 & 0 & 0 & 0 & 1 \end{array}\right]$$

In Equation (2.3.19), the stress–strain relationship is derived assuming a plane stress state. Moreover, in the plate bending problem, stress is calculated based on the assumption of a constitutive matrix of a plane stress state using the strain represented by Equation (2.3.30).

$$\boldsymbol{\sigma}_{\mathrm{b}}^{(e)} = \boldsymbol{D}^{(e)}\boldsymbol{\varepsilon}_{\mathrm{b}}^{(e)} = z\boldsymbol{D}^{(e)}\boldsymbol{B}_{\mathrm{b}}^{(e)}\boldsymbol{U}^{(e)} \tag{2.3.31}$$

$$\boldsymbol{\sigma}_{\mathrm{b}}^{(e)} = \lfloor \sigma_x^{(e)}, \sigma_y^{(e)}, \tau_{xy}^{(e)} \rfloor^t$$

Whereas, the bending moment in a plate can be computed using Equation (2.3.31) as follows:

$$\begin{aligned}\boldsymbol{M}^{(e)} &= \int_{t/2}^{t/2} z\boldsymbol{\sigma}_{\mathrm{b}}^{(e)} dz = \int_{t/2}^{t/2} z\boldsymbol{D}^{(e)}\boldsymbol{\varepsilon}_{\mathrm{b}}^{(e)} dz \\ &= \boldsymbol{D}^{(e)} \int_{t/2}^{t/2} z^2 \, dz \boldsymbol{B}_{\mathrm{b}}^{(e)}\boldsymbol{U}^{(e)} = \frac{t^3}{12}\boldsymbol{D}^{(e)}\boldsymbol{B}_{\mathrm{b}}^{(e)}\boldsymbol{U}^{(e)} \\ &= \boldsymbol{D}_{\mathrm{b}}^{(e)}\boldsymbol{B}_{\mathrm{b}}^{(e)}\boldsymbol{U}^{(e)} \end{aligned} \tag{2.3.32}$$

Here, $\boldsymbol{D}_{\mathrm{b}}^{(e)}$is defined as

$$\boldsymbol{D}_{\mathrm{b}}^{(e)} = \frac{t^3}{12}\boldsymbol{D}^{(e)} \tag{2.3.33}$$

These bending moments can be expressed using components as follows:

$$\begin{Bmatrix} M_x \\ M_y \\ M_{xy} \end{Bmatrix} = \frac{t^3}{12} \cdot \frac{E}{1-\nu^2} \begin{bmatrix} 1 & \nu & 0 \\ \nu & 1 & 0 \\ 0 & 0 & \dfrac{1-\nu}{2} \end{bmatrix} \begin{Bmatrix} \varepsilon_{x,z} \\ \varepsilon_{y,z} \\ \gamma_{xy,z} \end{Bmatrix} \tag{2.3.34}$$

The relationship between these bending moments are shown in Figure 2.3.8.

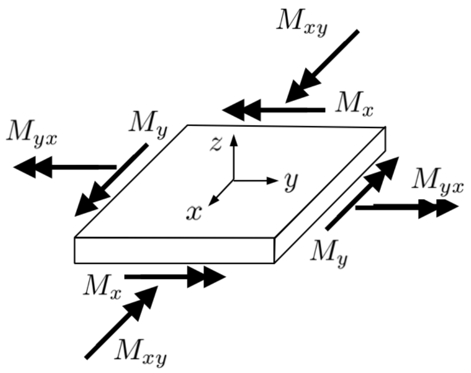

Fig.2.3.8 Bending moments acting on a plate

(3) Flat shell problem

In this study, the displacement of the flat shell is expressed by superimposing the displacements of the in-plane problem upon the out-of-plane problem as expressed by Equation (2.1.7). The displacement of the flat plate shell is given below.

$$u = u_0 - z\frac{\partial w_0}{\partial x} \tag{2.3.35}$$

$$v = v_0 - z\frac{\partial w_0}{\partial y} \tag{2.3.36}$$

$$w = w_0 \tag{2.3.37}$$

The degrees of freedom of the flat shell are as shown in Figure 2.3.7, and the displacement field is expressed as follows:

$$\boldsymbol{u}_s^{(e)} = \boldsymbol{u}_{\mathrm{i}}^{(e)} + \boldsymbol{u}_{\mathrm{b}}^{(e)} = \boldsymbol{N}_s^{(e)}\boldsymbol{U}^{(e)} \tag{2.3.38}$$

$$\boldsymbol{N}_s^{(e)} = \boldsymbol{N}_{\mathrm{i}}^{(e)} + \boldsymbol{Z}\boldsymbol{N}_{\mathrm{b}}^{(e)}$$

Whereas, the strain in the subdomain $\Omega^{(e)}$ (element e) is expressed, as follows, from the in-plane deformation and out-of-plane deformation.

$$\begin{aligned}\boldsymbol{\varepsilon}_{\mathrm{s}}^{(e)} = \left\{\begin{array}{c}\varepsilon_x^{(e)}\\ \varepsilon_y^{(e)}\\ \gamma_{xy}^{(e)}\end{array}\right\} &= \left\{\begin{array}{c}\dfrac{\partial u}{\partial x}\\ \dfrac{\partial v}{\partial y}\\ \dfrac{\partial v}{\partial x}+\dfrac{\partial u}{\partial y}\end{array}\right\} + z\left\{\begin{array}{c}-\dfrac{\partial^2 w}{\partial x^2}\\ -\dfrac{\partial^2 w}{\partial y^2}\\ -2\dfrac{\partial^2 w}{\partial x\partial y}\end{array}\right\}\\ &= \boldsymbol{\varepsilon}_{\mathrm{i}}^{(e)} + \boldsymbol{\varepsilon}_{\mathrm{b}}^{(e)}\end{aligned} \tag{2.3.39}$$

Here, the first term of Equation (2.3.39) represents strain $\boldsymbol{\varepsilon}_{\mathrm{i}}^{(e)}$ in the in-plane deformation problem, and the second term represents strain $\boldsymbol{\varepsilon}_{\mathrm{b}}^{(e)}$ in the out-of-plane deformation problem. The strains are given by Equations (2.3.18) and (2.3.30), respectively.

Additionally, in the flat shell problem, the stress–strain relationship assuming the plane stress state used in Equations (2.3.19) and (2.3.31) is applied. This stress–strain relationship is described below.

$$\boldsymbol{\sigma}_{\mathrm{s}}^{(e)} = \boldsymbol{D}^{(e)}\boldsymbol{\varepsilon}_{\mathrm{s}}^{(e)}, \tag{2.3.40}$$

where $\boldsymbol{D}^{(e)}$ is the constitutive matrix.

Equation (2.3.40) is expressed using strain $\boldsymbol{\varepsilon}_{\mathrm{i}}^{(e)}$ in the in-plane deformation problem and strain $\boldsymbol{\varepsilon}_{\mathrm{b}}^{(e)}$ in the out-of-plane deformation problem as follows:

$$\boldsymbol{\sigma}_{\mathrm{s}}^{(e)} = \boldsymbol{D}^{(e)}\left(\boldsymbol{\varepsilon}_{\mathrm{i}}^{(e)} + \boldsymbol{\varepsilon}_{\mathrm{b}}^{(e)}\right) \tag{2.3.41}$$

Substituting Equations (2.3.18) and (2.3.30) into Equation (2.3.41), the following relationship can be obtained:

$$\boldsymbol{\sigma}_{\mathrm{s}}^{(e)} = \boldsymbol{D}^{(e)} \left(\boldsymbol{B}_{\mathrm{i}}^{(e)} + z\boldsymbol{B}_{\mathrm{b}}^{(e)}\right) \boldsymbol{U}^{(e)} \tag{2.3.42}$$

The element internal force in the in-plane direction can be obtained by integrating this stress in the plate thickness direction as follows:

$$\begin{aligned} \boldsymbol{N}^{(e)} &= \int_{t/2}^{t/2} \boldsymbol{\sigma}_{\mathrm{s}}^{(e)} dz = \int_{t/2}^{t/2} \boldsymbol{D}^{(e)} \left(\boldsymbol{B}_{\mathrm{i}}^{(e)} + z\boldsymbol{B}_{\mathrm{b}}^{(e)}\right) \, dz \, \boldsymbol{U}^{(e)} \\ &= \boldsymbol{D}^{(e)} \int_{t/2}^{t/2} \, dz \boldsymbol{B}_{\mathrm{i}}^{(e)} \boldsymbol{U}^{(e)} = t\boldsymbol{D}^{(e)} \boldsymbol{B}_{\mathrm{i}}^{(e)} \boldsymbol{U}^{(e)} \\ &= \boldsymbol{D}_{\mathrm{i}}^{(e)} \boldsymbol{B}_{\mathrm{i}}^{(e)} \boldsymbol{U}^{(e)}, \end{aligned} \tag{2.3.43}$$

where

$$\boldsymbol{D}_{\mathrm{i}}^{(e)} = t\boldsymbol{D}^{(e)} \tag{2.3.44}$$

Equation (2.4.44) shows that the stress–strain relationship in the plane stress state is multiplied by the plate thickness *t*. The relationship expressed by the components is as follows:

$$t \begin{Bmatrix} \sigma_x \\ \sigma_y \\ \tau_{xy} \end{Bmatrix} = t \cdot \frac{E}{1-\nu^2} \begin{bmatrix} 1 & \nu & 0 \\ \nu & 1 & 0 \\ 0 & 0 & \dfrac{1-\nu}{2} \end{bmatrix} \begin{Bmatrix} \varepsilon_x \\ \varepsilon_y \\ \gamma_{xy} \end{Bmatrix} \tag{2.3.45}$$

The bending moment can be obtained by multiplying the stress in Equation (2.3.42) by the function z in the plate thickness direction and integrating the plate thickness.

$$\begin{aligned} \boldsymbol{M}^{(e)} &= \int_{t/2}^{t/2} z\boldsymbol{\sigma}_{\mathrm{s}}^{(e)} dz = \int_{t/2}^{t/2} \boldsymbol{D}^{(e)} \left(z\boldsymbol{B}_{\mathrm{i}}^{(e)} + z^2\boldsymbol{B}_{\mathrm{b}}^{(e)}\right) \, dz \, \boldsymbol{U}^{(e)} \\ &= \boldsymbol{D}^{(e)} \int_{t/2}^{t/2} z^2 \, dz \boldsymbol{B}_{\mathrm{b}}^{(e)} \boldsymbol{U}^{(e)} = \frac{t^3}{12} \boldsymbol{D}^{(e)} \boldsymbol{B}_{\mathrm{b}}^{(e)} \boldsymbol{U}^{(e)} \\ &= \boldsymbol{D}_{\mathrm{b}}^{(e)} \boldsymbol{B}_{\mathrm{b}}^{(e)} \boldsymbol{U}^{(e)}, \end{aligned} \tag{2.3.46}$$

where

$$\boldsymbol{D}_{\mathrm{b}}^{(e)} = \frac{t^3}{12}\boldsymbol{D}^{(e)} \tag{2.3.47}$$

The relationship expressed by the components is as follows:

$$\begin{Bmatrix} M_x \\ M_y \\ M_{xy} \end{Bmatrix} = \frac{t^3}{12} \cdot \frac{E}{1-\nu^2} \begin{bmatrix} 1 & \nu & 0 \\ \nu & 1 & 0 \\ 0 & 0 & \dfrac{1-\nu}{2} \end{bmatrix} \begin{Bmatrix} \varepsilon_{x,z} \\ \varepsilon_{y,z} \\ \gamma_{xy,z} \end{Bmatrix} \tag{2.3.48}$$

2.3.4 *Relative Displacement*

The displacement at any point on the neutral plane of the subdomain is given by Equation (2.3.16). The displacement of the subdomains $\Omega^{(a)}$ and $\Omega^{(b)}$ on the adjacent boundary $\Gamma_{<ab>}$, shown in Figure 2.3.9, are defined as follows:

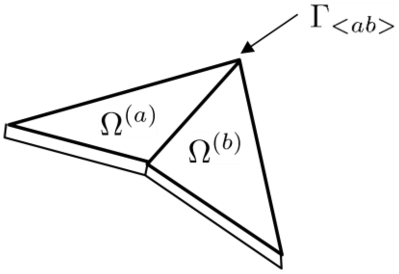

Fig.2.3.9 Adjacent boundary $\Gamma_{<ab>}$ of subdomains $\Omega^{(a)}$ and $\Omega^{(b)}$

$$\boldsymbol{u}_{<ab>}^{(a)} \overset{\text{def.}}{=} \boldsymbol{u}^{(a)}\Big|_{\Gamma_{<ab>}} \tag{2.3.49a}$$

$$\boldsymbol{u}_{<ab>}^{(b)} \overset{\text{def.}}{=} \boldsymbol{u}^{(b)}\Big|_{\Gamma_{<ab>}} \tag{2.3.49b}$$

Here, the superscripts (a) and (b) represent the subdomain numbers, and the subscript <ab> represents the adjacent boundary numbers. That is, $\boldsymbol{u}_{<ab>}^{(a)}$ implies the displacement on the boundary $\Gamma_{<ab>}$ of the subdomain $\Omega^{(a)}$. Similarly, the coefficient matrix is defined as follows:

$$\boldsymbol{N}_{<ab>}^{(a)} \overset{\text{def.}}{=} \boldsymbol{N}^{(a)}\Big|_{\Gamma_{<ab>}} \tag{2.3.50a}$$

$$\boldsymbol{N}_{<ab>}^{(b)} \overset{\text{def.}}{=} \boldsymbol{N}^{(b)}\Big|_{\Gamma_{<ab>}} \tag{2.3.50b}$$

Therefore, the displacement of the subdomains $\Omega^{(a)}$ and $\Omega^{(b)}$ on the boundary $\Gamma_{<ab>}$ is obtained as follows:

$$\boldsymbol{u}^{(a)}_{<ab>} = \boldsymbol{N}^{(a)}_{<ab>}\boldsymbol{U}^{(a)} \tag{2.3.51}$$

$$\boldsymbol{u}^{(b)}_{<ab>} = \boldsymbol{N}^{(b)}_{<ab>}\boldsymbol{U}^{(b)} \tag{2.3.52}$$

Equations (2.3.51) and (2.3.52) are represented by the local coordinate system set for each subdomain, as shown in Figure 2.3.10. However, in the computation of relative displacement, the displacement in each subdomain needs to be represented by the same coordinate system. In this paper, the relative displacement is computed according to the coordinate system on the $\Omega^{(a)}$ side.

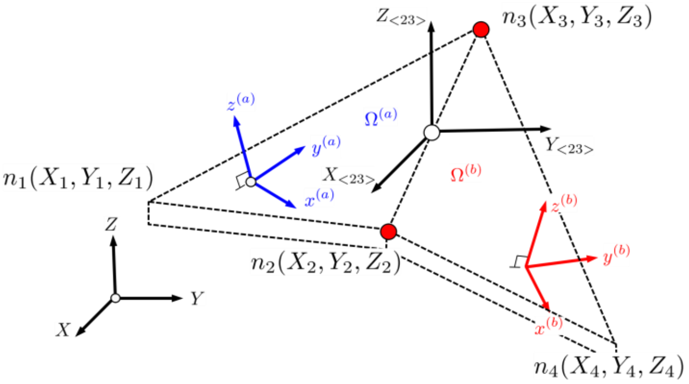

Fig.2.3.10 Coordinate system for each subdomain

First, the coordinate transformation between the local and global coordinate systems will be summarized. The relationship between the local coordinate system $\boldsymbol{x}$ in the two subregions $\Omega^{(a)}$ and $\Omega^{(b)}$ and global coordinate system $\boldsymbol{X}$, shown in Figure 2.3.10, is expressed as follows:

$$\boldsymbol{x}^{(a)}_{<23>} = \boldsymbol{R}^{(a)}_{x}\boldsymbol{X}_{<23>} \tag{2.3.53}$$

$$\boldsymbol{x}^{(b)}_{<23>} = \boldsymbol{R}^{(b)}_{x}\boldsymbol{X}_{<23>} \tag{2.3.54}$$

Here, $\boldsymbol{R}^{(e)}_{x}$ is the transformation matrix of the local coordinate system $\boldsymbol{x}$ and global coordinate system $\boldsymbol{X}$ of the element (e); the components are expressed as follows:

$$\boldsymbol{R}_x^{(e)} = \begin{bmatrix} l_1 & m_1 & n_1 \\ l_2 & m_2 & n_2 \\ l_3 & m_3 & n_3 \end{bmatrix} \tag{2.3.55}$$

Here, each component is obtained using the coordinate system shown in Fig. 2.3.11

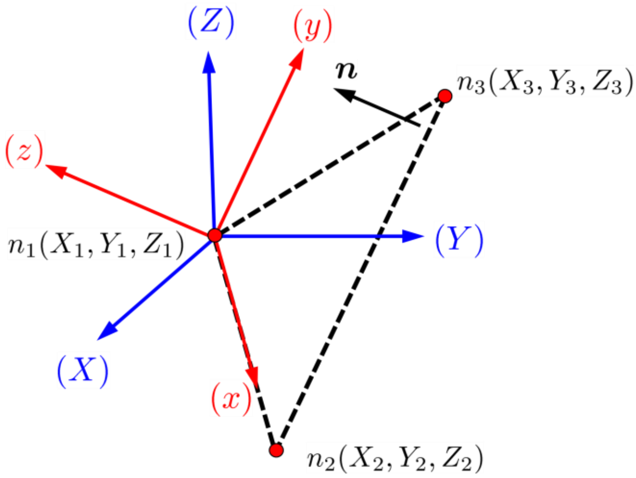

Fig.2.3.11 Local coordinate system $x - y - z$ and global coordinate system $X - Y - Z$

$$\boldsymbol{X}_i = \lfloor X_i,\ Y_i,\ Z_i \rfloor^t, \boldsymbol{X}'_i = \lfloor X'_i,\ Y'_i,\ Z'_i \rfloor^t$$

$$\boldsymbol{X}'_2 = \boldsymbol{X}_2 - \boldsymbol{X}_1, \boldsymbol{X}'_3 = \boldsymbol{X}_3 - \boldsymbol{X}_1$$

$$L = \sqrt{(X'_2)^2 + (Y'_2)^2 + (Z'_2)^2}$$

$$2A = \sqrt{\begin{vmatrix} Y'_2 & Z'_2 \\ Y'_3 & Z'_3 \end{vmatrix}^2 + \begin{vmatrix} Z'_2 & X'_2 \\ Z'_3 & X'_3 \end{vmatrix}^2 + \begin{vmatrix} X'_2 & Y'_2 \\ X'_3 & Y'_3 \end{vmatrix}^2}$$

$$l_1 = \frac{X'_2}{L}, m_1 = \frac{Y'_2}{L}, n_1 = \frac{Z'_2}{L}$$

$$l_2 = \frac{1}{2AL}\left(Z'_2 \begin{vmatrix} Z'_2 & X'_2 \\ Z'_3 & X'_3 \end{vmatrix} - Y'_2 \begin{vmatrix} X'_2 & Y'_2 \\ X'_3 & Y'_3 \end{vmatrix} \right)$$

$$m_2 = \frac{1}{2AL}\left(X'_2 \begin{vmatrix} X'_2 & Y'_2 \\ X'_3 & Y'_3 \end{vmatrix} - Z'_2 \begin{vmatrix} Y'_2 & Z'_2 \\ Y'_3 & Z'_3 \end{vmatrix} \right)$$

$$n_2 = \frac{1}{2AL}\left(Y'_2 \begin{vmatrix} Y'_2 & Z'_2 \\ Y'_3 & Z'_3 \end{vmatrix} - X'_2 \begin{vmatrix} Z'_2 & X'_2 \\ Z'_3 & X'_3 \end{vmatrix} \right)$$

$$l_3 = \frac{1}{2A}\begin{vmatrix} Y'_2 & Z'_2 \\ Y'_3 & Z'_3 \end{vmatrix}, m_3 = \frac{1}{2A}\begin{vmatrix} Z'_2 & X'_2 \\ Z'_3 & X'_3 \end{vmatrix}, n_3 = \frac{1}{2A}\begin{vmatrix} X'_2 & Y'_2 \\ X'_3 & Y'_3 \end{vmatrix}$$

Using Equations (2.3.53) and (2.3.54) to transform the local coordinate system $\boldsymbol{x}$ into the global coordinate system $\boldsymbol{X}$, we get

$$\boldsymbol{X}_{<23>} = \left(\boldsymbol{R}_x^{(b)}\right)^{-1} \boldsymbol{x}_{<23>}^{(b)} \tag{2.3.56}$$

$$\boldsymbol{X}_{<23>} = \left(\boldsymbol{R}_x^{(a)}\right)^{-1} \boldsymbol{x}_{<23>}^{(a)} \tag{2.3.57}$$

From these relationships, the coordinate system of the subdomain $\Omega^{(b)}$ can be transformed into the coordinate system of the subdomain $\Omega^{(a)}$ as follows:

$$\boldsymbol{x}_{<23>}^{(a)} = \boldsymbol{R}_x^{(a)} \left(\boldsymbol{R}_x^{(b)}\right)^{-1} \boldsymbol{x}_{<23>}^{(b)} \tag{2.3.58}$$

However, in this paper, to obtain the relative displacement, it is converted into the values in the tangential and normal directions with respect to the local coordinate system provided at the adjacent boundary shown in Figure 2.3.12. Therefore, it is necessary to convert the displacement of the local coordinate system for each subdomain into the displacement of the coordinate system along the adjacent boundary.

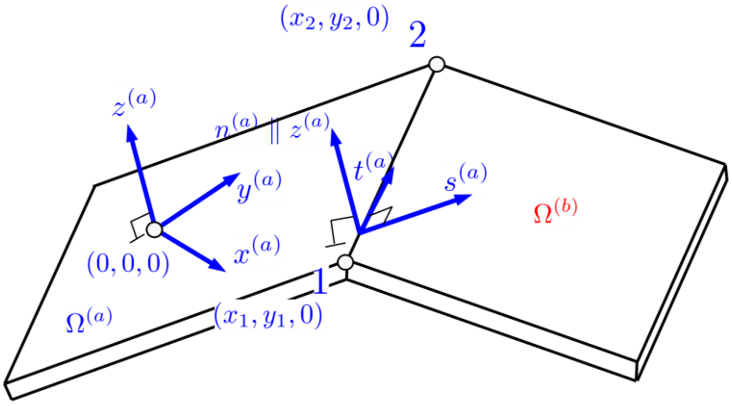

Fig.2.3.12 Local coordinate system of subdomain and adjacent boundary

Focusing on the subregion $\Omega^{(a)}$, the transformation is expressed as follows:

$$\boldsymbol{x}_n^{(a)} = \boldsymbol{R}_{<12>}^{(a)} \boldsymbol{x}^{(a)} \tag{2.3.59}$$

$$\boldsymbol{x}^{(a)} = \lfloor x^{(a)},\ y^{(a)},\ z^{(a)} \rfloor^t$$

$$\boldsymbol{x}_n^{(a)} = \lfloor s^{(a)},\ t^{(a)},\ n^{(a)} \rfloor^t$$

Here, $\boldsymbol{x}^{(a)}$ is the value in the local coordinate system of the partial region, $\boldsymbol{x}_n^{(a)}$ is the value in the local coordinate system provided on the adjacent boundary edge, and $\boldsymbol{R}_{<12>}^{(a)}$ is the coordinate transformation matrix for these coordinate systems, expressed as

$$\boldsymbol{R}_{<12>}^{(a)} = \begin{bmatrix} l_1^{(a)} & m_1^{(a)} & 0 \\ l_2^{(a)} & m_2^{(a)} & 0 \\ 0 & 0 & 1 \end{bmatrix} \tag{2.3.60}$$

The components of the coordinate transformation matrix are as follows:

$$l_1^{(a)} = \frac{x_{21}}{L},\ m_1^{(a)} = \frac{y_{21}}{L},\ l_2^{(a)} = \frac{y_{21}}{L},\ m_2^{(a)} = -\frac{x_{21}}{L}$$

$$L = \sqrt{x_{21}^2 + y_{21}^2},$$

where

$$\left.\begin{aligned} x_{ij} &= x_i - x_j \\ y_{ij} &= y_i - y_j \end{aligned}\right\}.$$

Using the above coordinate transformation relationship, the relative displacement between adjacent elements is found. Figure 2.3.13 shows the two subdomains $\Omega^{(a)}$ and $\Omega^{(b)}$ and their common boundary $\Gamma_{<ab>}$. In this paper, the relative displacement of the two subdomains shown in Figure 2.3.13 is computed with reference to the normal direction of $\Omega^{(a)}$.

The displacement $\boldsymbol{u}_{n<ab>}^{(a|a)}$ with respect to the coordinate system $n - s - t$ on the boundary of $\Omega^{(a)}$ can be obtained from Equations (2.3.51) and (2.3.59) as follows:

$$\begin{aligned} \boldsymbol{u}_{n<ab>}^{(a|a)} &= \boldsymbol{R}_{<ab>}^{(a)} \boldsymbol{u}_{<ab>}^{(a)} \\ &= \boldsymbol{R}_{<ab>}^{(a)} \boldsymbol{N}_{<ab>}^{(a)} \boldsymbol{U}^{(a)} \end{aligned} \tag{2.3.61}$$

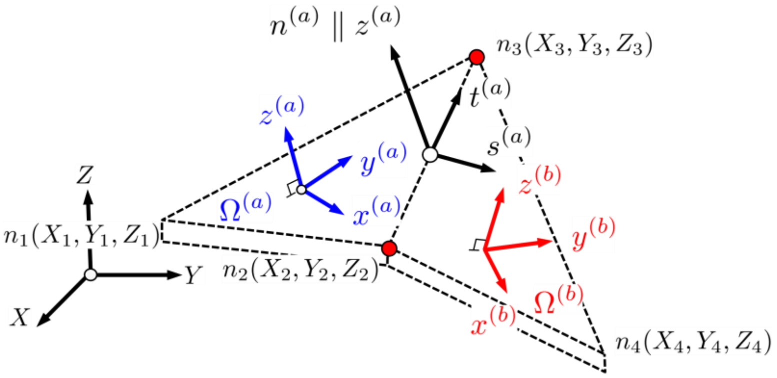

Fig.2.3.13 Local coordinate system on adjacent element boundaries

The displacement on the boundary of $\Omega^{(b)}$ is converted to the local coordinate system of $\Omega^{(a)}$ using Equation (2.3.58). The result is further converted into a coordinate system on the boundary coordinates based on $\Omega^{(a)}$ using Equation (2.3.59). Consequently, the following relationship is obtained:

$$\begin{aligned}\boldsymbol{u}_{n_{<ab>}}^{(b|a)} &= \boldsymbol{R}_{<ab>}^{(a)} \boldsymbol{R}_{x}^{(a)} \left(\boldsymbol{R}_{x}^{(b)}\right)^{-1} \boldsymbol{u}_{<ab>}^{(b)} \\ &= \boldsymbol{R}_{<ab>}^{(a)} \boldsymbol{R}_{x}^{(a)} \left(\boldsymbol{R}_{x}^{(b)}\right)^{-1} \boldsymbol{N}_{<ab>}^{(b)} \boldsymbol{U}^{(b)} \qquad (2.3.62)\end{aligned}$$

The relative displacement $\boldsymbol{\delta}_{N<ab>}^{(a)}$ on the neutral plane of the adjacent element can be obtained as the difference between Equations (2.3.61) and (2.3.62).

$$\begin{aligned}\boldsymbol{\delta}_{N<ab>}^{(a)} &= \boldsymbol{u}_{n_{<ab>}}^{(a|a)} - \boldsymbol{u}_{n_{<ab>}}^{(b|a)} \\ &= \boldsymbol{R}_{<ab>}^{(a)} \boldsymbol{N}_{<ab>}^{(a)} \boldsymbol{U}^{(a)} + \boldsymbol{R}_{<ab>}^{(b)} \boldsymbol{R}_{x}^{(a)} \left(\boldsymbol{R}_{x}^{(b)}\right)^{-1} \boldsymbol{N}_{<ab>}^{(b)} \boldsymbol{U}^{(b)} \\ &= \boldsymbol{B}_{N<ab>} \boldsymbol{U}_{<ab>} \qquad (2.3.63)\end{aligned}$$

Here,

$$\boldsymbol{B}_{N<ab>} = \left\lfloor \boldsymbol{R}_{<ab>}^{(a)} \boldsymbol{N}_{<ab>}^{(a)} \quad \boldsymbol{R}_{<ab>}^{(b)} \boldsymbol{R}_{x}^{(a)} \left(\boldsymbol{R}_{x}^{(b)}\right)^{-1} \boldsymbol{N}_{<ab>}^{(b)} \right\rfloor$$

$$\boldsymbol{U}_{<ab>} = \left\lfloor \boldsymbol{U}^{(a)} \quad \boldsymbol{U}^{(b)} \right\rfloor^{t}$$

However, in the case of the out-of-plane problem of the proposed model, as shown in Equations (2.3.22) and (2.3.23), there is a term related to the gradient of deflection. To maintain continuity with respect to these terms, it is necessary to obtain relative quantities in preparation for them. With reference to Equations (2.3.24) and (2.3.25), the gradient can be expressed as follows:

$$\boldsymbol{w}_{\theta}^{(e)} = \boldsymbol{N}_{\theta}^{(e)} \boldsymbol{U}^{(e)} \tag{2.3.64}$$

where,

$$\boldsymbol{w}_{\theta}^{(e)} = \lfloor -\frac{\partial w}{\partial x}, -\frac{\partial w}{\partial y} \rfloor^{t}$$

$$\boldsymbol{N}_{\theta}^{(e)} = \lfloor \boldsymbol{N}_{d\theta}^{(e)}, \boldsymbol{N}_{\theta\theta}^{(e)}, \boldsymbol{N}_{\varepsilon\theta}^{(e)}, \boldsymbol{N}_{\varepsilon_x\theta}^{(e)}, \boldsymbol{N}_{\varepsilon_y\theta}^{(e)}, \boldsymbol{N}_{\varepsilon_z\theta}^{(e)} \rfloor^{t}$$

$$\boldsymbol{N}_{\theta \mathrm{b}}^{(e)} = \begin{bmatrix} 0 & 1 & 0 \\ -1 & 0 & 0 \end{bmatrix}, \boldsymbol{N}_{\varepsilon \mathrm{b}}^{(e)} = \begin{bmatrix} x & 0 & y/2 \\ 0 & y & x/2 \end{bmatrix}$$

$$\boldsymbol{N}_{d\theta} = \boldsymbol{N}_{\varepsilon \mathrm{b}} = \boldsymbol{N}_{\varepsilon_x \mathrm{b}} = \boldsymbol{N}_{\varepsilon_y \mathrm{b}} = \boldsymbol{O}$$

Equation (2.3.64) is expressed as a gradient on the boundary of adjacent elements according to the method in Equation (2.3.49a) and (2.3.49b). Next, applying the coordinate transformation of Equation (2.3.59) to the local coordinates on the boundary edge, we get

$$\boldsymbol{w}_{\theta_n <ab>}^{(a|a)} = \boldsymbol{R}_{<ab>}^{(a)} \boldsymbol{w}_{\theta <ab>}^{(a)} = \boldsymbol{R}_{<ab>}^{(a)} \boldsymbol{N}_{\theta <ab>}^{(a)} \boldsymbol{U}^{(a)} \tag{2.3.65}$$

$$\boldsymbol{w}_{\theta_n <ab>}^{(b|a)} = \boldsymbol{R}_{<ab>}^{(b)} \boldsymbol{w}_{\theta <ab>}^{(b)} = \boldsymbol{R}_{<ab>}^{(b)} \boldsymbol{N}_{\theta <ab>}^{(b)} \boldsymbol{U}^{(b)} \tag{2.3.66}$$

Here, $\boldsymbol{w}_{\theta <ab>}^{(e)}$ is the gradient on the boundary $\Gamma_{<ab>}$ of the region $\Omega^{(e)}$, and $\boldsymbol{R}_{<ab>}^{(a)}$ represents the coordinate transformation matrix shown in Equation (2.3.60). $\boldsymbol{w}_{\theta_n <ab>}^{(a|a)}$ is the gradient of deflection with respect to the local coordinate system $n-s-t$ provided at the boundary $\Gamma_{<ab>}$ of the region $\Omega^{(a)}$, and $\boldsymbol{w}_{\theta_n <ab>}^{(b|a)}$ is the gradient of deflection with respect to the local coordinate system $n-s-t$ provided at the boundary $\Gamma_{<ab>}$ of the region $\Omega^{(b)}$.

Now, the relative deflection gradient is expressed as

$$\begin{aligned}\boldsymbol{\delta}_{\theta<ab>}^{(a)} &= \boldsymbol{w}_{\theta_{n<ab>}}^{(a|a)} - \boldsymbol{w}_{\theta_{n<ab>}}^{(b|a)} \\ &= \boldsymbol{R}_{<ab>}^{(a)}\boldsymbol{N}_{\theta<ab>}^{(a)}\boldsymbol{U}^{(a)} + \boldsymbol{R}_{<ab>}^{(b)}\boldsymbol{N}_{\theta<ab>}^{(b)}\boldsymbol{U}^{(b)} \\ &= \boldsymbol{B}_{\theta<ab>}\boldsymbol{U}_{<ab>}\end{aligned} \tag{2.3.67}$$

Here,

$$\boldsymbol{B}_{\theta<ab>} = \lfloor \boldsymbol{R}_{<ab>}^{(a)}\boldsymbol{N}_{\theta<ab>}^{(a)} \quad \boldsymbol{R}_{<ab>}^{(b)}\boldsymbol{N}_{\theta<ab>}^{(b)} \rfloor$$

2.3.5 *Lagrange Multipliers*

The physical meaning of the Lagrange multiplier $\boldsymbol{\lambda}$ is equivalent to the surface force on the intersection boundary, as described in Section 2.2.4. Generally, the principle of hybrid-type variational work deals with this multiplier as an unknown parameter. Because the Lagrange multiplier $\boldsymbol{\lambda}$ is equivalent to the surface force on boundary $\Gamma_{<ab>}$ in subdomains $\Omega^{(a)}$ and $\Omega^{(b)}$, this surface force is assumed as Equation (2.3.3) in this paper.

$$\boldsymbol{\lambda}_{<ab>} = \boldsymbol{k} \cdot \boldsymbol{\delta}_{<ab>} \tag{2.3.68}$$

Here, $\boldsymbol{\delta}_{<ab>}$ represents the relative displacement on the intersection boundary $\Gamma_{<ab>}$ between subdomains $\Omega^{(a)}$ and $\Omega^{(b)}$, and $\boldsymbol{k}$ is a matrix that relates the surface force $\boldsymbol{\lambda}_{<ab>}$ to relative displacement $\boldsymbol{\delta}_{<ab>}$. In this paper, the relative displacement $\boldsymbol{\delta}_{<ab>}$ deals with the displacement on the neutral plane represented by Equation (2.3.6) and the gradient of deflection represented by Equation (2.3.66). In addition, assuming that the connection of adjacent elements is bent, the relative displacement is calculated with reference to the normal vector on the $\Omega^{(a)}$ side. Therefore, $\boldsymbol{\delta}_{<ab>}$ is displayed as $\boldsymbol{\delta}_{<ab>}^{(a)}$, which is defined as

$$\boldsymbol{\delta}_{<ab>}^{(a)} = \lfloor \boldsymbol{\delta}_{N<ab>}^{(a)} \quad \boldsymbol{\delta}_{\theta<ab>}^{(a)} \rfloor^{t} \tag{2.3.69}$$

$\boldsymbol{\delta}_{N<ab>}^{(a)}$ represents the relative displacement along the coordinate axes $n - s - t$ shown in Figure 2.3.14, and $\boldsymbol{\delta}_{\theta<ab>}^{(a)}$ represents the relative displacement related to the rotation of *n* and *s* in the figure.

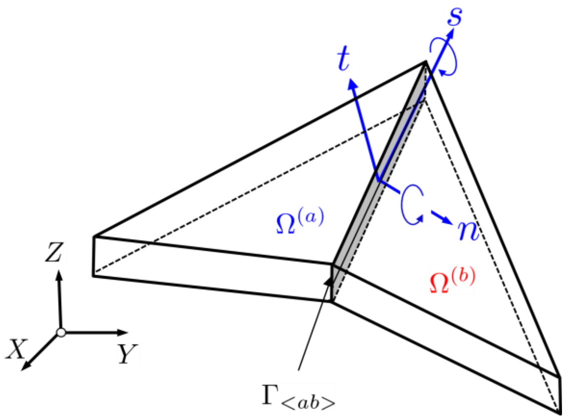

Fig.2.3.14 Local coordinate system on the boundary $\Gamma_{<ab>}$

However, $\boldsymbol{\lambda}^{(a)}_{<ab>}$ is the surface force corresponding to their relative displacement, having the following relationship:

$$\boldsymbol{\lambda}^{(a)}_{<ab>} = \lfloor \boldsymbol{\lambda}^{(a)}_{N<ab>} \quad \boldsymbol{\lambda}^{(a)}_{\theta<ab>} \rfloor^t \tag{2.3.70}$$

$\boldsymbol{\lambda}^{(a)}_{N<ab>}$ represents the surface force in the $n-s-t$ coordinate axis direction, and $\boldsymbol{\lambda}^{(a)}_{\theta<ab>}$ represents the surface force with respect to the gradient of deflection around the *n*- and *s*-axes, corresponding to the bending moment; they are expressed in terms of components as follows:

$$\boldsymbol{\lambda}^{(a)}_{N<ab>} = \lfloor \lambda^{(a)}_{s<ab>} \quad \lambda^{(a)}_{t<ab>} \quad \lambda^{(a)}_{n<ab>} \rfloor^t \tag{2.3.71}$$

$$\boldsymbol{\lambda}^{(a)}_{\theta<ab>} = \lfloor \lambda^{(a)}_{\theta_s<ab>} \quad \lambda^{(a)}_{\theta_n<ab>} \rfloor^t \tag{2.3.72}$$

In this paper, the surface force in Equations (2.3.71) and (2.3.72) is computed from Equation (2.3.68) using the relative displacement in Equation (2.3.70). Now, $\boldsymbol{k}$ is a penalty matrix and has the following relationship:

$$\boldsymbol{k} = \begin{bmatrix} \boldsymbol{k}_N & 0 \\ 0 & \boldsymbol{k}_\theta \end{bmatrix} \tag{2.3.73}$$

In addition, each component is given as follows:

$$\boldsymbol{k}_N = \begin{bmatrix} k_s & 0 & 0 \\ 0 & k_t & 0 \\ 0 & 0 & k_n \end{bmatrix} \tag{2.3.74}$$

$$\boldsymbol{k}_\theta = \begin{bmatrix} k_s & 0 \\ 0 & k_t \end{bmatrix} \tag{2.3.75}$$

In the HPM, using the penalty function p, the coefficient $\boldsymbol{k}$ is expressed as follows:

$$k_s = k_t = k_n = p \tag{2.3.76}$$

The concept of this surface contact used in HPM is exactly the same as RBSM. According to the concept of springs used in RBSM, the penalty function used in HPM assumes a very hard spring. In this paper, for the penalty function shown in Equation (2.3.75), a weighted penalty function is assumed based on the RBSM concept as follows:

$$k_n = \frac{(1+\nu)E'}{(1-\nu^2)(h_1+h_2)} \tag{2.3.77}$$

$$k_s = k_t = \frac{E'}{(1+\nu)(h_1+h_2)} \tag{2.3.78}$$

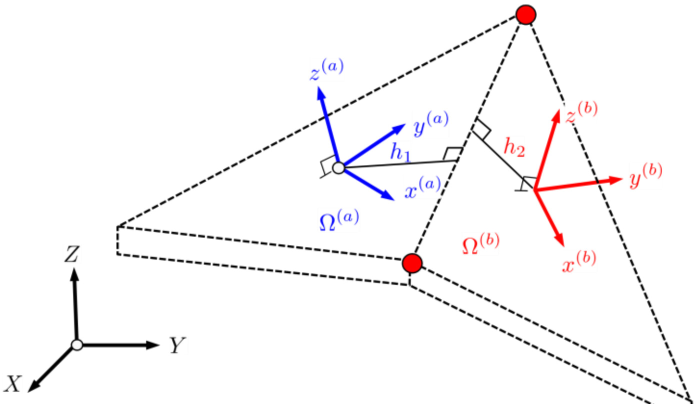

Fig.2.3.15 Height of the perpendicular line

Here, ν is Poisson ratio and h_1 and h_2 are the heights of the perpendicular line to the intersection boundary from the gravity center of each subdomain, as shown in Figure 2.3.15.

Also, *E* is elastic modulus and *E'* is penalty value defined as

$$E' = E \times p \tag{2.3.79}$$

Here, *p* is a penalty function, and a value $(p = 10^6)$ is set.

2.3.6 *Discretized Equations*

In the derivation of the discretization equation, independent displacement fields for each small subdomain, represented by Equation (2.3.38), were substituted into the hybrid-type virtual work Equation (2.2.20). The discretization of the first term of Equation (2.2.20) is described first; the first term is expressed as follows:

$$\int_{\Omega^{(e)}} \boldsymbol{\sigma} : \mathrm{grad}\delta\boldsymbol{u}\, dV = \int_{\Omega^{(e)}} {}^{t}\delta\boldsymbol{\varepsilon}_{s}^{(e)} \boldsymbol{D}^{(e)} \boldsymbol{\varepsilon}_{s}^{(e)}\, dV \tag{2.3.80}$$

Moreover, the strain of the flat shell element is expressed by the following equation:

$$\begin{aligned} \boldsymbol{\varepsilon}^{(e)} &= \boldsymbol{\varepsilon}_{\mathrm{i}}^{(e)} + \boldsymbol{\varepsilon}_{\mathrm{b}}^{(e)} \\ &= \boldsymbol{B}_{\mathrm{i}}^{(e)} \boldsymbol{U}^{(e)} + z\boldsymbol{B}_{\mathrm{b}}^{(e)} \boldsymbol{U}^{(e)} \end{aligned} \tag{2.3.81}$$

Similarly, the virtual strain is also defined as

$$\begin{aligned} \delta\boldsymbol{\varepsilon}^{(e)} &= \delta\boldsymbol{\varepsilon}_{\mathrm{i}}^{(e)} + \delta\boldsymbol{\varepsilon}_{\mathrm{b}}^{(e)} \\ &= \boldsymbol{B}_{\mathrm{i}}^{(e)} \delta\boldsymbol{U}^{(e)} + z\boldsymbol{B}_{\mathrm{b}}^{(e)} \delta\boldsymbol{U}^{(e)} \end{aligned} \tag{2.3.82}$$

Substituting Equations (2.3.81) and (2.3.82) into Equation (2.3.80) obtains the following equation:

$$\int_{\Omega^{(e)}} \boldsymbol{\sigma} : \mathrm{grad}\delta\boldsymbol{u}\, dV = \int_{\Omega^{(e)}} \left({}^{t}\delta\boldsymbol{\varepsilon}_{\mathrm{i}}^{(e)} + {}^{t}\delta\boldsymbol{\varepsilon}_{\mathrm{b}}^{(e)} \right) \boldsymbol{D}^{(e)} \left(\boldsymbol{\varepsilon}_{\mathrm{i}}^{(e)} + \boldsymbol{\varepsilon}_{\mathrm{b}}^{(e)} \right) dV \tag{2.3.83}$$

Here, $\boldsymbol{\varepsilon}_{\mathrm{b}}^{(e)}$is a linear function of z. Therefore, the integral for the thickness direction (z) with respect to the product with $\boldsymbol{\varepsilon}_{\mathrm{i}}^{(e)}$ is 0. Hence, Equation (2.3.83) is expressed as

$$\int_{\Omega^{(e)}} \boldsymbol{\sigma} : \mathrm{grad}\delta \boldsymbol{u}\, dV = \int_{\Omega^{(e)}} {}^{t}\delta\boldsymbol{\varepsilon}_{\mathrm{i}}^{(e)} \boldsymbol{D}^{(e)} \boldsymbol{\varepsilon}_{\mathrm{i}}^{(e)}\, dV + \int_{\Omega^{(e)}} {}^{t}\delta\boldsymbol{\varepsilon}_{\mathrm{b}}^{(e)} \boldsymbol{D}^{(e)} \boldsymbol{\varepsilon}_{\mathrm{b}}^{(e)}\, dV \tag{2.3.84}$$

The first term on the right-hand side of Equation (2.3.84) relates to the in-plane deformation, and the second term relates to the out-of-plane deformation.

The first term for in-plane deformation is expressed as

$$\begin{aligned} \int_{\Omega^{(e)}} {}^{t}\delta\boldsymbol{\varepsilon}_{\mathrm{i}}^{(e)} \boldsymbol{D}^{(e)} \boldsymbol{\varepsilon}_{\mathrm{i}}^{(e)}\, dV &= {}^{t}\delta\boldsymbol{U}^{(e)} \int_{\Omega_{xy}^{(e)}} {}^{t}\boldsymbol{B}_{\mathrm{i}}^{(e)} (t\boldsymbol{D}^{(e)}) \boldsymbol{B}_{\mathrm{i}}^{(e)} dA \boldsymbol{U}^{(e)} \\ &= \left(\delta\boldsymbol{U}^{(e)}\right)^{t} \boldsymbol{k}_{\mathrm{i}}^{(e)} \boldsymbol{U}^{(e)} \end{aligned} \tag{2.3.85}$$

Similarly, the second term on the out-of-plane deformation is expressed as

$$\begin{aligned} \int_{\Omega^{(e)}} {}^{t}\delta\boldsymbol{\varepsilon}_{\mathrm{b}}^{(e)} \boldsymbol{D}^{(e)} \boldsymbol{\varepsilon}_{\mathrm{b}}^{(e)}\, dV &= \left(\delta\boldsymbol{U}^{(e)}\right)^{t} \int_{\Omega_{xy}^{(e)}} {}^{t}\boldsymbol{B}_{\mathrm{b}}^{(e)} \left(\frac{t^3}{12}\boldsymbol{D}_{\mathrm{b}}^{(e)}\right) \boldsymbol{B}_{\mathrm{b}}^{(e)}\, dA \boldsymbol{U}^{(e)} \\ &= \left(\delta\boldsymbol{U}^{(e)}\right)^{t} \boldsymbol{k}_{\mathrm{b}}^{(e)} \boldsymbol{U}^{(e)}, \end{aligned} \tag{2.3.86}$$

where

$$\boldsymbol{k}_{\mathrm{i}}^{(e)} = \int_{\Omega_{xy}^{(e)}} {}^{t}\boldsymbol{B}_{\mathrm{i}}^{(e)} \boldsymbol{D}_{\mathrm{i}}^{(e)} \boldsymbol{B}_{\mathrm{i}}^{(e)} dA,$$

$$\boldsymbol{k}_{\mathrm{b}}^{(e)} = \int_{\Omega_{xy}^{(e)}} {}^{t}\boldsymbol{B}_{\mathrm{b}}^{(e)} \boldsymbol{D}_{\mathrm{b}}^{(e)} \boldsymbol{B}_{\mathrm{b}}^{(e)}\, dA.$$

Here, $\boldsymbol{D}_{\mathrm{i}}^{(e)}$ and $\boldsymbol{D}_{\mathrm{b}}^{(e)}$ are as shown in Equations (2.3.44) and (2.3.47).

Therefore, the first term of the Equation (2.2.20) for the hybrid-type virtual work is discretized as

$$\int_{\Omega^{(e)}} \boldsymbol{\sigma} : \mathrm{grad}\delta\boldsymbol{u}\, dV = {}^t\delta\boldsymbol{U}^{(e)} \left(\boldsymbol{k}_{\mathrm{i}}^{(e)} + \boldsymbol{k}_{\mathrm{b}}^{(e)}\right) \boldsymbol{U}^{(e)} \tag{2.3.87}$$

Similarly, the second term of Equation (2.2.20) can be represented as

$$\begin{aligned} \int_{\Omega^{(e)}} \boldsymbol{f} \cdot \delta\boldsymbol{u} dV &= {}^t\delta\boldsymbol{U}^{(e)} \int_{\Omega^{(e)}} {}^t\boldsymbol{N}_s^{(e)} \boldsymbol{f}\, dV \\ &= {}^t\delta\boldsymbol{U}^{(e)} \int_{\Omega_{xy}^{(e)}} {}^t\boldsymbol{N}_s^{(e)} \left(\int_{-t/2}^{t/2} dz\right) \boldsymbol{f}\, dA \end{aligned} \tag{2.3.88}$$

For simplicity, the integral term is expressed as

$$\boldsymbol{w}_s^{(e)} = \int_{\Omega_{xy}^{(e)}} {}^t\boldsymbol{N}_s^{(e)} \boldsymbol{f} \cdot t\, dA \tag{2.3.89}$$

The second term of the virtual work equation is represented as

$$\int_{\Omega^{(e)}} \boldsymbol{f} \cdot \delta\boldsymbol{u} dV = {}^t\delta\boldsymbol{U}^{(e)} \boldsymbol{w}_s^{(e)} \tag{2.3.90}$$

The third term of Equation (2.2.20) is represented as

$$\begin{aligned} \int_{\Gamma^{(e)}} \boldsymbol{t} \cdot \delta\boldsymbol{u} dS &= {}^t\delta\boldsymbol{U}^{(e)} \int_{\Gamma^{(e)}} {}^t\boldsymbol{N}_s^{(e)} \boldsymbol{t}\, dS \\ &= {}^t\delta\boldsymbol{U}^{(e)} \int_{\Gamma_{xy}^{(e)}} {}^t\boldsymbol{N}_s^{(e)} \left(\int_{-t/2}^{t/2} dz\right) \boldsymbol{t}\, ds \end{aligned} \tag{2.3.91}$$

The integral term is expressed in the same manner as in Equation (2.3.9).

$$\boldsymbol{p}_s^{(e)} = \int_{\Gamma_{xy}^{(e)}} {}^t\boldsymbol{N}_s^{(e)} \boldsymbol{t} \cdot t\, ds \tag{2.3.92}$$

Subsequently, the third term of the virtual work equation is represented as

$$\int_{\Gamma^{(e)}} \boldsymbol{t} \cdot \delta\boldsymbol{u} dS = {}^t\delta\boldsymbol{U}^{(e)} \boldsymbol{p}_s^{(e)} \tag{2.3.93}$$

Therefore, the discretized virtual work equation can be obtained as

$$\delta W_s^{(e)} = \ {}^t\delta \boldsymbol{U}^{(e)} \left(\boldsymbol{k}_{\mathrm{i}}^{(e)} + \boldsymbol{k}_{\mathrm{b}}^{(e)}\right) \boldsymbol{U}^{(e)} - \left(\delta \boldsymbol{U}^{(e)}\right)^t \boldsymbol{w}_s^{(e)} - \left(\delta \boldsymbol{U}^{(e)}\right)^t \boldsymbol{p}_s^{(e)} \qquad (2.3.94)$$

Now, let $\boldsymbol{\mathcal{M}}_s^{(e)}$ be a matrix that relates the degrees of freedom $\boldsymbol{U}$ in domain Ω and degrees of freedom $\boldsymbol{U}^{(e)}$ in the target subdomain $\Omega^{(e)}$. Then, the displacement and virtual displacement for each partial region can be expressed as follows:

$$\boldsymbol{U}^{(e)} = \boldsymbol{\mathcal{M}}_s^{(e)} \boldsymbol{U} \qquad (2.3.95)$$

$$\delta \boldsymbol{U}^{(e)} = \boldsymbol{\mathcal{M}}_s^{(e)} \delta \boldsymbol{U} \qquad (2.3.96)$$

Therefore, the discretized virtual work in Equation (2.3.94) is expressed using all degrees of freedom $\boldsymbol{U}$ as

$$\delta W_s^{(e)} = \delta \boldsymbol{U}^t \boldsymbol{K}_s^{(e)} \boldsymbol{U} - \delta \boldsymbol{U}^t \boldsymbol{P}_s^{(e)}, \qquad (2.3.97)$$

where

$$\boldsymbol{P}_s^{(e)} = \boldsymbol{W}_s^{(e)} + \boldsymbol{P}_s^{(e)}.$$

Also, each coefficient matrix is given as follows:

$$\boldsymbol{K}_s^{(e)} = {}^t\boldsymbol{\mathcal{M}}_s^{(e)} \left(\boldsymbol{k}_{\mathrm{i}}^{(e)} + \boldsymbol{k}_{\mathrm{b}}^{(e)}\right) \boldsymbol{\mathcal{M}}_s^{(e)}$$

$$\boldsymbol{W}_s^{(e)} = {}^t\boldsymbol{\mathcal{M}}_s^{(e)} \boldsymbol{w}_s^{(e)}$$

$$\boldsymbol{P}_s^{(e)} = {}^t\boldsymbol{\mathcal{M}}_s^{(e)} \boldsymbol{p}_s^{(e)}$$

Equation (2.2.19) demonstrates how the subsidiary conditions for virtual work are considered using the Lagrange multiplier. In the case of a flat shell, the subsidiary condition can be expressed using the relative displacement shown in Equation (2.3.69).

$$H_{s<ab>} = -\delta \int_{\Gamma_{<ab>}} \boldsymbol{\lambda}_{<ab>}^{(a)} \boldsymbol{\delta}_{<ab>}^{(a)} dS$$

$$= -\delta \int_{\Gamma_{<ab>}} \left(\boldsymbol{\lambda}_{N<ab>}^{(a)} \boldsymbol{\delta}_{N<ab>}^{(a)} + \boldsymbol{\lambda}_{\theta<ab>}^{(a)} \boldsymbol{\delta}_{\theta<ab>}^{(a)} \right) dS \tag{2.3.98}$$

The Lagrange multiplier implies the surface force, and in this paper, it is assumed as in Equation (2.3.68). Now, using the relation of Equations (2.3.69), (2.3.70), and (2.3.73), this can be expressed as

$$H_{<s>}^{(a)} = -\delta \int_{\Gamma_{<ab>}} {}^{t}\boldsymbol{\delta}_{N<ab>}^{(a)} \cdot \boldsymbol{k_N} \cdot \boldsymbol{\delta}_{N<ab>}^{(a)} \, dS - \delta \int_{\Gamma_{<ab>}} {}^{t}\boldsymbol{\delta}_{\theta<ab>}^{(a)} \cdot \boldsymbol{k_\theta} \cdot \boldsymbol{\delta}_{\theta<ab>}^{(a)} \, dS \tag{2.3.99}$$

For the first term of Equation (2.3.99), the relative displacement $\boldsymbol{\delta}_{N<ab>}^{(a)}$ is given by Equation (2.3.63). Therefore, it can be expressed as

$$\delta \int_{\Gamma_{<ab>}} {}^{t}\boldsymbol{\delta}_{N<ab>}^{(a)} \cdot \boldsymbol{k_N} \cdot \boldsymbol{\delta}_{N<ab>}^{(a)} \, dS = \delta \boldsymbol{U}_{<ab>}^{t} \int_{\Gamma_{<ab>}} \boldsymbol{B}_{N<ab>}^{t} \boldsymbol{k_N} \cdot \boldsymbol{B}_{N<ab>} \, dS \boldsymbol{U}_{<ab>} \tag{2.3.100}$$

The integral of the first term of Equation (2.3.99) is expressed as follows:

$$\begin{aligned} \boldsymbol{k}_{N<ab>} &= \int_{\Gamma_{<ab>}} \boldsymbol{B}_{N<ab>}^{t} \boldsymbol{k_N} \boldsymbol{B}_{N<ab>} \, dS \\ &= \int_{\Gamma_{xy<s>}} \boldsymbol{B}_{N<ab>}^{t} \left(\int_{-t/2}^{t/2} \boldsymbol{k}_N dz \right) \boldsymbol{B}_{N<ab>} \, ds \\ &= \int_{\Gamma_{xy<s>}} \boldsymbol{B}_{N<ab>}^{t} \overline{\boldsymbol{k}}_N \boldsymbol{B}_{N<ab>} \, ds, \end{aligned} \tag{2.3.101}$$

where

$$\overline{\boldsymbol{k}}_N = t \begin{bmatrix} k_s & 0 & 0 \\ 0 & k_t & 0 \\ 0 & 0 & k_n \end{bmatrix}. \tag{2.3.102}$$

Similarly, regarding the second term, because the relative displacement $\boldsymbol{\delta}_{\theta<ab>}^{(a)}$ is given by Equation (2.3.67), it can be expressed as

$$\delta \int_{\Gamma_{<ab>}} {}^t\boldsymbol{\delta}^{(a)}_{\theta<ab>} \cdot \boldsymbol{k_\theta} \cdot \boldsymbol{\delta}^{(a)}_{\theta<ab>}\, dS = \delta \boldsymbol{U}^t_{<ab>} \int_{\Gamma_{<ab>}} \boldsymbol{B}^t_{\theta<ab>} \boldsymbol{k_\theta} \cdot \boldsymbol{B}_{\theta<ab>}\, dS \boldsymbol{U}_{<ab>} \tag{2.3.103}$$

Similarly, the integral of the second term is expressed as

$$\begin{aligned} \boldsymbol{k}_{\theta<ab>} &= \int_{\Gamma_{<ab>}} \boldsymbol{B}^t_{\theta<ab>} z^2 \boldsymbol{k}_\theta \boldsymbol{B}_{\theta<ab>}\, dS \\ &= \int_{\Gamma_{xy<s>}} \boldsymbol{B}^t_{\theta<ab>} \left(\int_{-t/2}^{t/2} z^2 \boldsymbol{k}_\theta dz \right) \boldsymbol{B}_{\theta<ab>}\, ds \\ &= \int_{\Gamma_{xy<s>}} \boldsymbol{B}^t_{\theta<ab>} \overline{\boldsymbol{k}}_\theta \boldsymbol{B}_{\theta<ab>}\, ds, \end{aligned} \tag{2.3.104}$$

where

$$\overline{\boldsymbol{k}}_\theta = \begin{bmatrix} \frac{t^3}{2} k_s & 0 \\ 0 & \frac{t^3}{2} k_t \end{bmatrix}. \tag{2.3.105}$$

Therefore, Equation (2.3.93) is expressed as follows:

$$H_{s<s>} = -\delta \boldsymbol{U}^t_{<s>} \boldsymbol{k}_{N<s>} \boldsymbol{U}_{<s>} - \delta \boldsymbol{U}^t_{<s>} \boldsymbol{k}_{\theta<s>} \boldsymbol{U}_{<s>} \tag{2.3.106}$$

Equation (2.3.106) is simplified as

$$H_{s<s>} = -\delta \boldsymbol{U}^t_{<s>} \left(\boldsymbol{k}_{N<s>} + \boldsymbol{k}_{\theta<s>} \right) \boldsymbol{U}_{<s>} \tag{2.3.107}$$

Now, let $\boldsymbol{\mathcal{M}}^{(e)}_s$ be a matrix that relates the degrees of freedom $\boldsymbol{U}$ in all partial areas Ω and degrees of freedom $\boldsymbol{U}^{(e)}$ in the target partial area $\Omega^{(e)}$. The degree of freedom $\boldsymbol{U}_{<s>}$ related to the target partial area boundary is expressed by the total degree of freedom $\boldsymbol{U}$ as

$$\boldsymbol{U}_{<ab>} = \lfloor \boldsymbol{\mathcal{M}}^{(a)}_s \,,\, \boldsymbol{\mathcal{M}}^{(b)}_s \rfloor^t \boldsymbol{U} \tag{2.3.108}$$

$$\delta \boldsymbol{U}_{<ab>} = \lfloor \boldsymbol{\mathcal{M}}^{(a)}_s \,,\, \boldsymbol{\mathcal{M}}^{(b)}_s \rfloor^t \delta \boldsymbol{U} \tag{2.3.109}$$

Substituting Equations (2.3.108) and (2.3.109) into Equation (2.3.107), the discretized subsidiary condition with all degrees of freedom $\boldsymbol{U}$ is obtained as follows:

$$H_{s_{<s>}} = -\delta \boldsymbol{U}^t \boldsymbol{K}_{s_{<s>}} \boldsymbol{U}, \tag{2.3.110}$$

where

$$\boldsymbol{K}_{s_{<ab>}} = \lfloor \boldsymbol{\mathcal{M}}_s^{(a)} \ , \ \boldsymbol{\mathcal{M}}_s^{(b)} \rfloor \left(\boldsymbol{k}_{N<s>} + \boldsymbol{k}_{\theta<s>} \right) \left\{ \begin{array}{c} \boldsymbol{\mathcal{M}}_s^{(a)} \\ \boldsymbol{\mathcal{M}}_s^{(b)} \end{array} \right\}.$$

Therefore, the discretization Equation (2.3.20) of hybrid-type virtual work is expressed as follows:

$$\sum_{e=1}^{M} \delta W_s^{(e)} + \sum_{s=1}^{N} H_{s_{<s>}} = 0 \tag{2.3.111}$$

Here, M represents the number of subdomains (elements), and N represents the number of intersection boundaries of adjacent subdomains. Equation (2.3.111) is expressed from Equations (2.3.97) and (2.3.107) as follows

$$\delta \boldsymbol{U}^t \left(\sum_{e=1}^{M} \boldsymbol{K}_s^{(e)} + \sum_{s=1}^{N} \boldsymbol{K}_{s_{<s>}} \right) \boldsymbol{U} - \delta \boldsymbol{U}^t \sum_{e=1}^{M} \boldsymbol{P}_s^{(e)} = 0 \tag{2.3.112}$$

Because the virtual displacement is arbitrary, the following discretization equation for the plate bending problem can be obtained:

$$\boldsymbol{K}_s \boldsymbol{U} = \boldsymbol{P}_s \tag{2.3.113}$$

Here, $\boldsymbol{K}_s$ and $\boldsymbol{P}_s$ are defined as

$$\boldsymbol{K}_s = \sum_{e=1}^{M} \boldsymbol{K}_s^{(e)} + \sum_{s=1}^{N} \boldsymbol{K}_{s_{<s>}}$$

$$\boldsymbol{P}_s = \sum_{e=1}^{M} \boldsymbol{P}_s^{(e)}$$

2.4 Numerical Examples

2.4.1 *Cantilever with Load Acting from Two Directions* [30]

The accuracy of the solution for the proposed flat shell element is verified by a simple numerical example. Figure 2.4.1 shows the model used for the analysis. This model is a thin plate with a length of 100 mm, width of 20 mm, and thickness of 4 mm, with the left side constrained. In-plane and out-of-plane loads are applied along the right edge. The material constants are as shown in Figure 2.4.1.

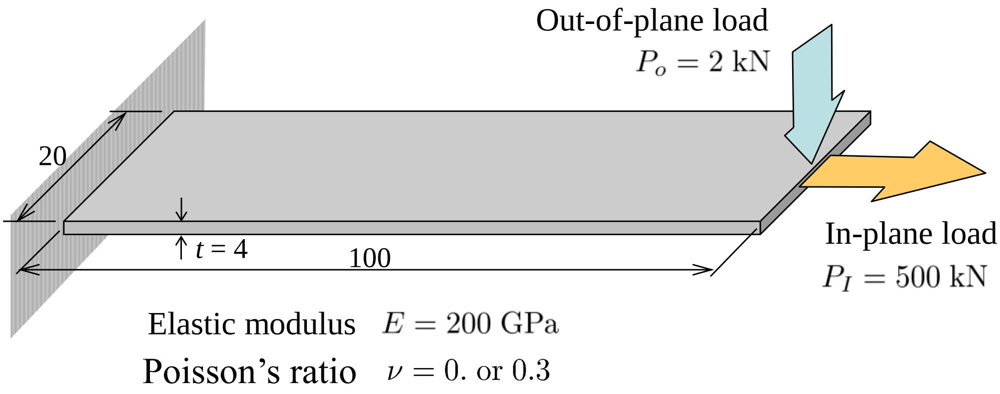

Fig.2.4.1 Numerical analysis model

Three analysis cases were set according to the loading conditions shown in Figure 2.4.1:

CASE-1: in-plane load
CASE-2: out-of-plane load
CASE-3: both in-plane and out-of-plane loads

Figure 2.4.2 shows the mesh division and boundary conditions; the upper-half of the analysis area is considered symmetrical. As shown in the figure, 10 x 10 mm squares are divided into crosses. Figure 2.4.2(a) shows the boundary conditions for the in-plane direction, where the left extremity is a slide. Figure 2.4.2(b) shows the boundary conditions for the out-of-plane direction, where the left extremity is fixed.

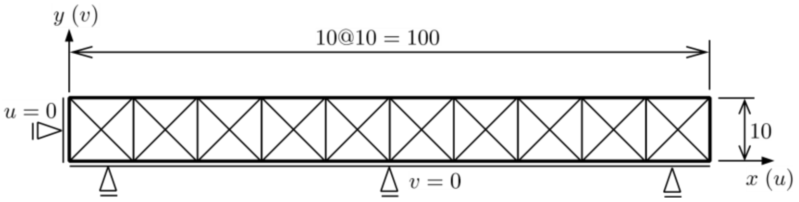

(a) Boundary condition (in-plane)

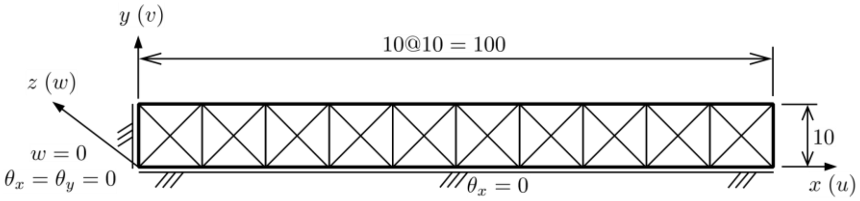

(b) Boundary condition (out-of-plane)

Fig.2.4.2 Mesh division and boundary conditions

(1) CASE-1 (in-plane load)

Figure 2.4.3(a) shows the deformation mode with a Poisson’s ratio of 0 when an in-plane load is applied. The displacement at the right extremity represents the simulation result by this method. Also, u_{exact} in parentheses represents the analytical solution. The error in this method was less than 0.01%. Figure 2.4.3(b) shows the deformation mode with a Poisson ratio of 0.3 when an in-plane load is applied. As shown, the effect of the Poisson ratio was correctly evaluated for the proposed flat shell element.

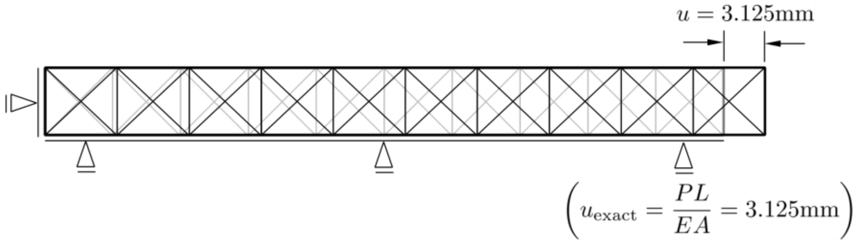

(a) Poisson’s Ratio: 0

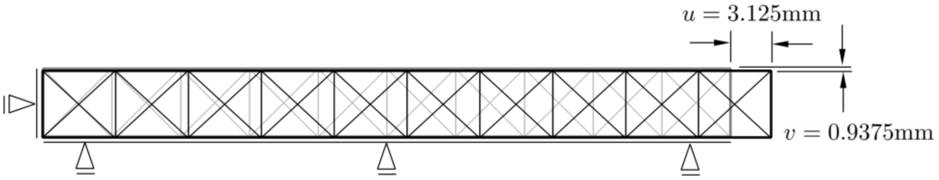

(b) Poisson’s Ratio: 0.3

Fig.2.4.3 Displacement mode (CASE-1)

(2) CASE-2 (out-of-plane load)

Figure 2.4.4 shows a deflection curve with a Poisson’s ratio of 0 when an out-of-plane load is applied.

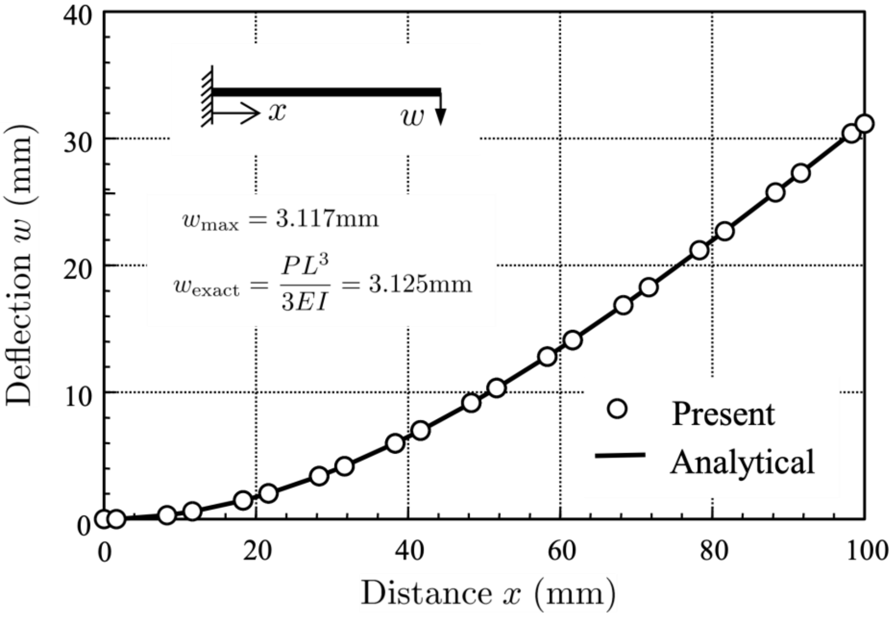

Fig.2.4.4 Deflection curve (CASE-2)

The horizontal axis in Figure 2.4.4 represents the distance from the left edge of the thin plate to the center of each element, and the vertical axis represents the deflection. The symbol in Figure 2.4.4 indicates the deflection of the flat plate shell element and indicates the value at the element centroid. The solid line shows the deflection curve based on beam theory, which approaches the solution based on the proposed model. Comparing the maximum deflection at the right extremity of the proposed model with the solution based on beam theory, the error was found to be less than 0.26%, confirming the high accuracy of the model.

Figure 2.4.5 shows the deflection angles when an out-of-plane load is applied. The horizontal axis in the figure represents the distance from the left edge of the thin plate, and the vertical axis represents the deflection angle. The deflection angles of both the proposed model and beam theory are nearly equal.

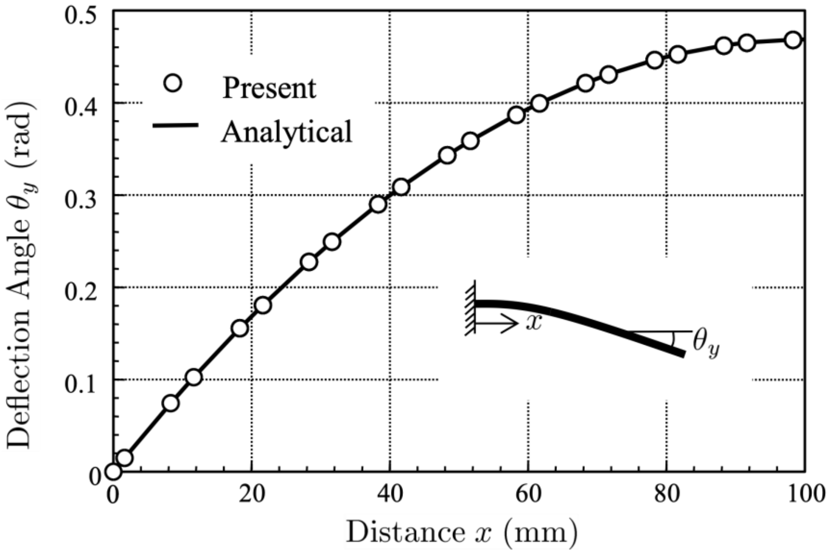

Fig.2.4.5 Deflection angle curve (CASE-2)

(3) CASE-3 (in-plane + out-of-plane loads)

Figure 2.4.6 shows the deformation state when the in-plane and out-of-plane loads act simultaneously. The horizontal axis represents the horizontal position of the flat plate obtained by multiplying the horizontal displacement by 10, and the vertical axis shows the deflection. This result is obtained by combining the horizontal displacement of CASE-1 and deflection of CASE-2. The results concurred with the concept of the proposed flat shell.

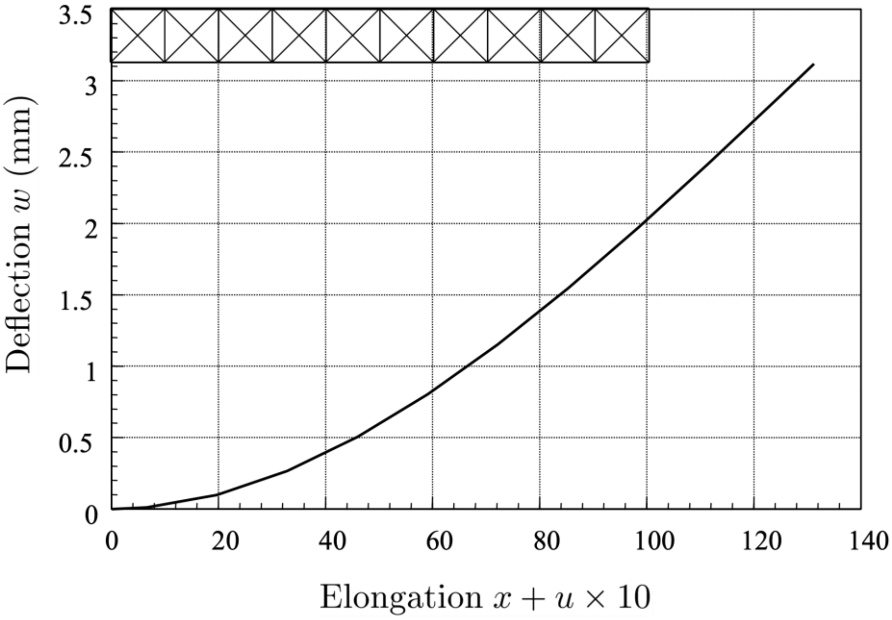

Fig.2.4.6 Deformation state for flat shell (CASE-3)

2.4.2 *Cantilever with Angle* [31]

To examine the accuracy of the displacement solution of the proposed flat plate shell model, the verification results using a simple model are shown. Figure 2.4.7 shows a numerical model of a cantilever bent at 90° under the axial and shear forces. The dimensions and load are shown in the figure. The material has an elastic modulus of E = 100 MPa and Poisson’s ratio of ν = 0. For the mesh division, a quadrilateral element is used as shown in the figure, and the displacement field of the in-plane deformation is a linear function.

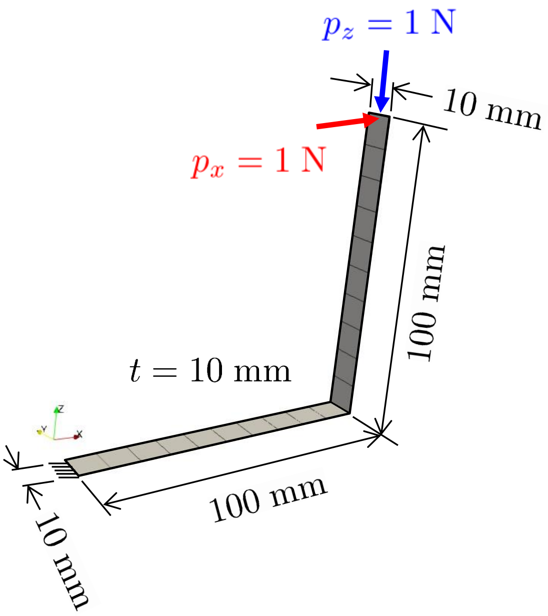

Fig.2.4.7 Numerical model for the cantilever bent at an angle

Figure 2.4.8 shows the value of the penalty function on the horizontal axis, and the ratio of the displacement at the beam tip to the beam theory equivalent on the vertical axis. The red line represents the horizontal displacement, and the blue line represents the vertical displacement. If a penalty of approximately 10^5–10^9 is used, a solution that is nearly consistent with the theoretical solution can be obtained. When it becomes 10^9 or more, the error tends to increase owing to the influence of the rounding error.

In Figure 2.4.9, the horizontal axis represents the number of elements, and the vertical axis represents the ratio of the model to the beam theory, as in the case of the penalty function. The red and blue lines, having the same denotations as the previous figure, show the values obtained by dividing the horizontal and vertical displacements by the solution of the beam theory. Even with a small number of divisions, such as 5, a solution with small error is obtained for both horizontal and vertical displacements. Because this model uses a quadratic function as the displacement field for bending, an accurate solution can be obtained.

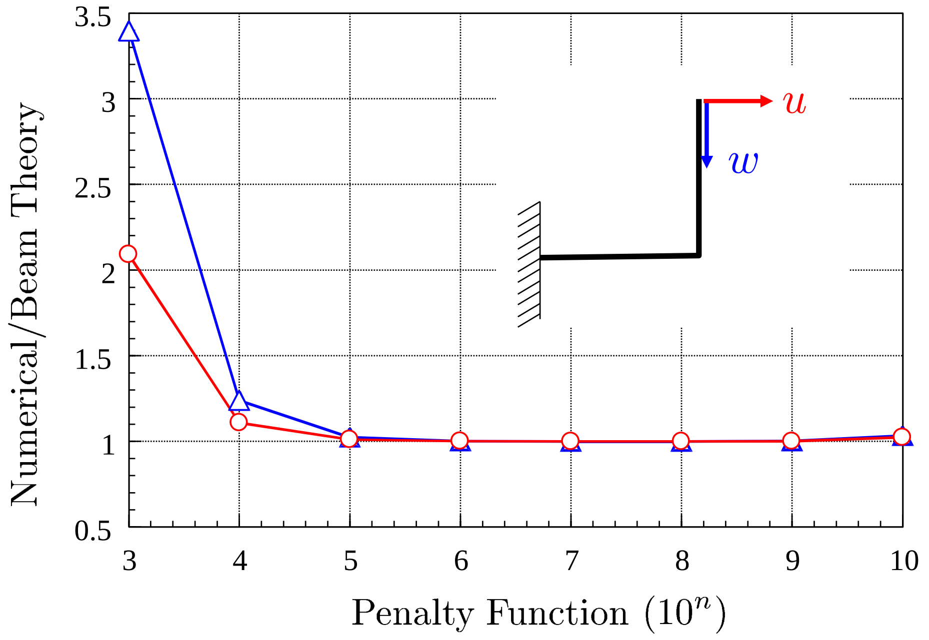

Fig.2.4.8 Convergence of displacement solution by penalty function

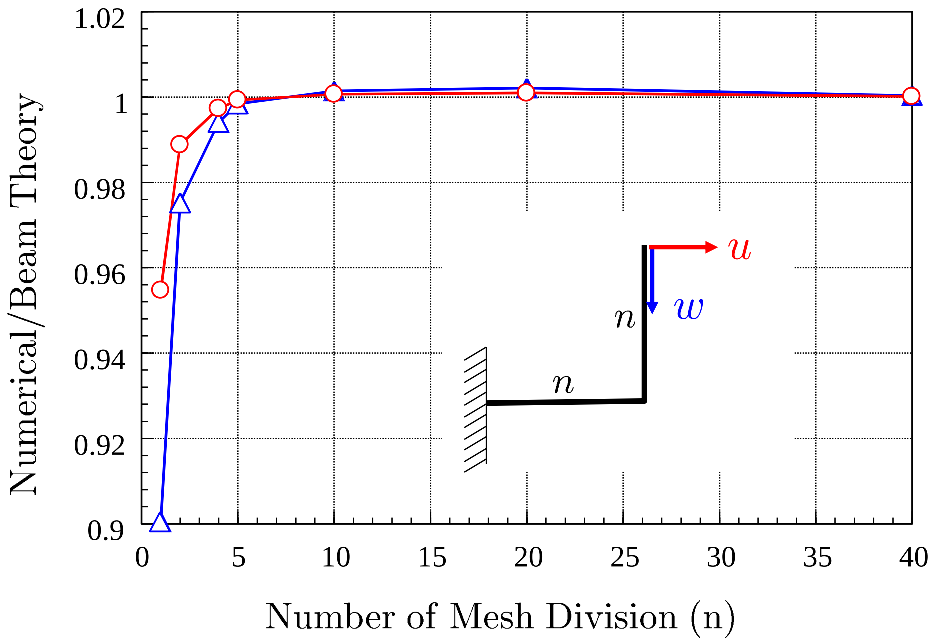

Fig.2.4.9 Convergence of displacement solution by number of elements

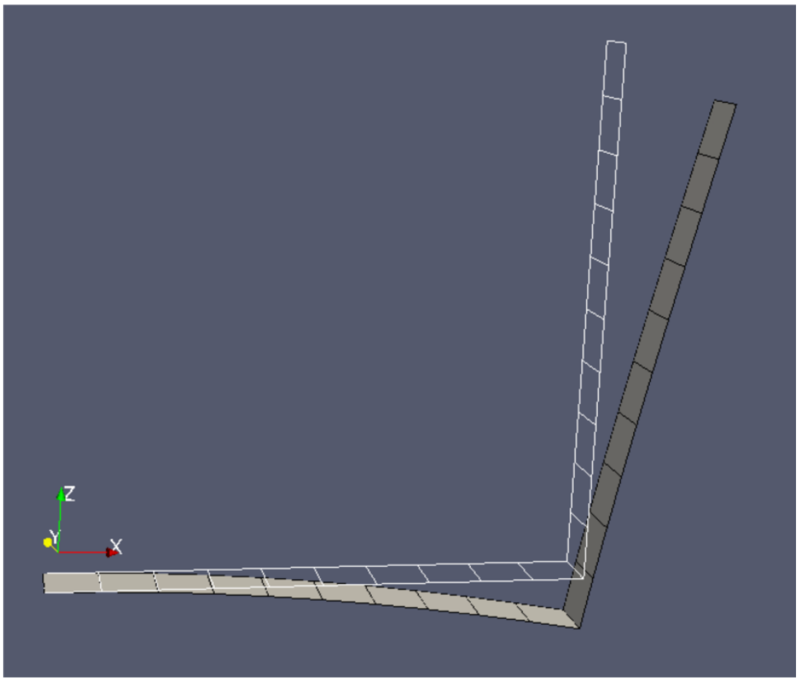

Fig.2.4.10 Displacement mode

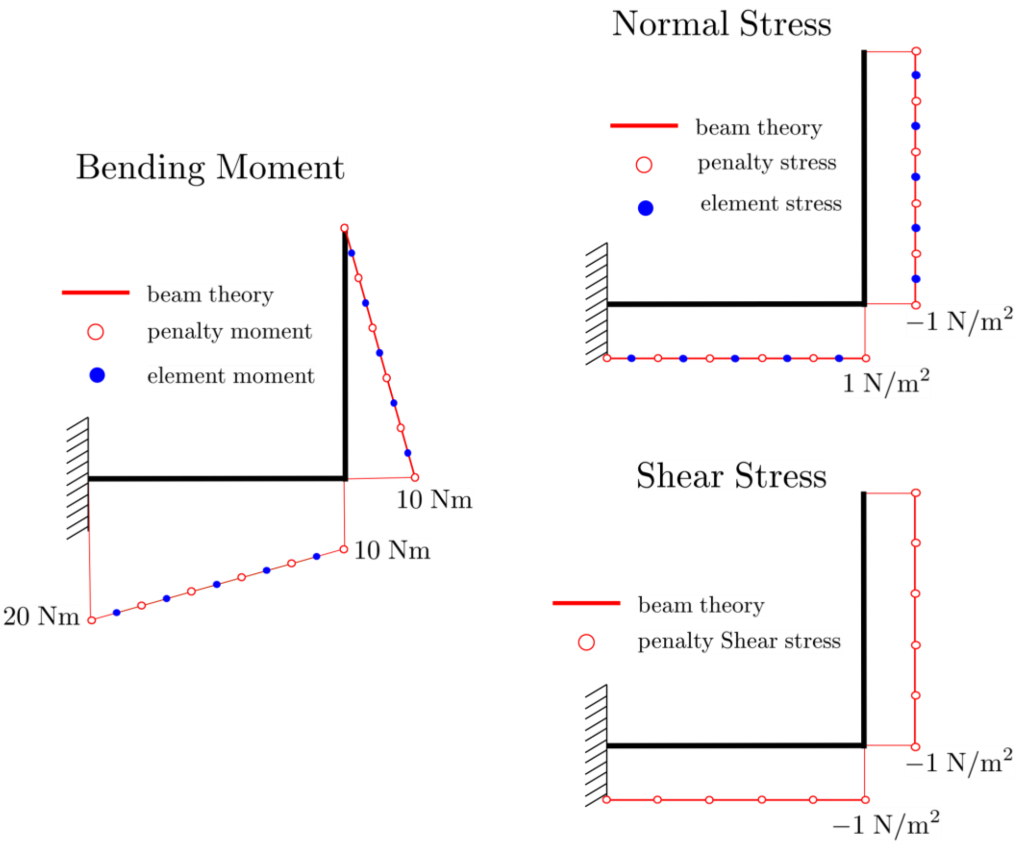

Fig.2.4.11 Sectional force distribution

Figure 2.4.10 shows the displacement mode. The wire frame is the original figure, and the filled plane is the deformed state; an appropriate displacement mode has been obtained.

Figure 2.4.11 shows the cross-sectional force diagram (axial force, bending moment, and shear force). The solid red line represents the solution according to the beam theory, the red circles represent the surface force on the boundary of the adjacent element, and the blue circles represent the cross-sectional force within the element. The section forces are in good agreement with the beam theory solution.

2.4.3 *Semicircular Curved Beam* [32]

A semicircular curved beam with a pin support at one end and a roller support at the other end was considered, as shown in Fig. 2.4.12(a); Figure 2.4.12(b) shows the beam model representation of the same problem.

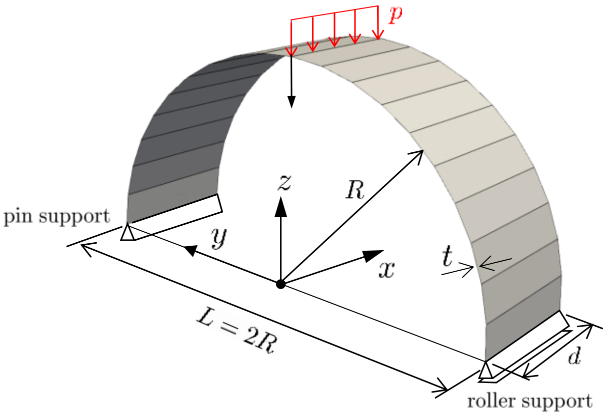

(a) Flat shell model

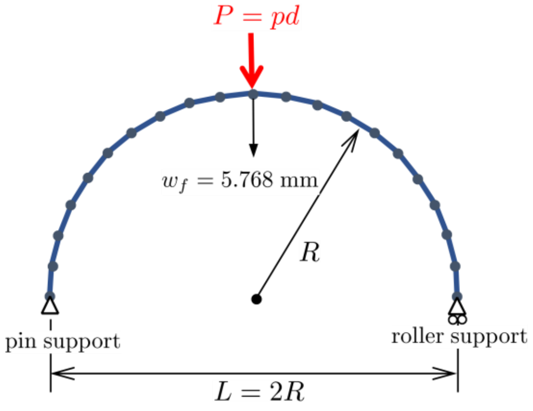

(b) Frame model

Fig.2.4.12 Numerical model for the accuracy of the elastic solution

The number of elements in both models shown in Figure 2.4.12 is 20. The parameters of the semicircular curved beam are R = 0.16 m, d = 0.1 m, and t = 0.002 m. The Young's modulus is E = 190 GN/m^2, Poisson's ratio is ν = 0, and geometrical moment of inertia is $I = 6.666 \times 10^{-11}\ \mathrm{m}^4$. A line load p = 1 kN/m $(P = p \times d = 100\ \mathrm{N})$ was applied at the top-middle of the model.

The theoretical result of the vertical displacement is

$$w_{\mathrm{Theory}} = \frac{PR^3}{4EI}\left(\frac{3\pi}{2} - 4\right) = 5.759\ \mathrm{mm}$$

In addition, the vertical displacement of the frame model with 20 elements, as shown in Fig.2.4.12(b), was computed as $w_f = 5.768\ \mathrm{mm}$.

Figure 2.4.13 shows the convergence of the displacement according to the number of elements. The circles represent the results of the flat shell model, and the blue line represents the results of the frame model with 20 elements. The horizontal axis represents the number of elements, and the vertical axis represents the ratio of the analytical solution to the vertical displacement of the center. The solution by the proposed method has an error of approximately 0.4% even with a rough element division of nearly 20 elements.

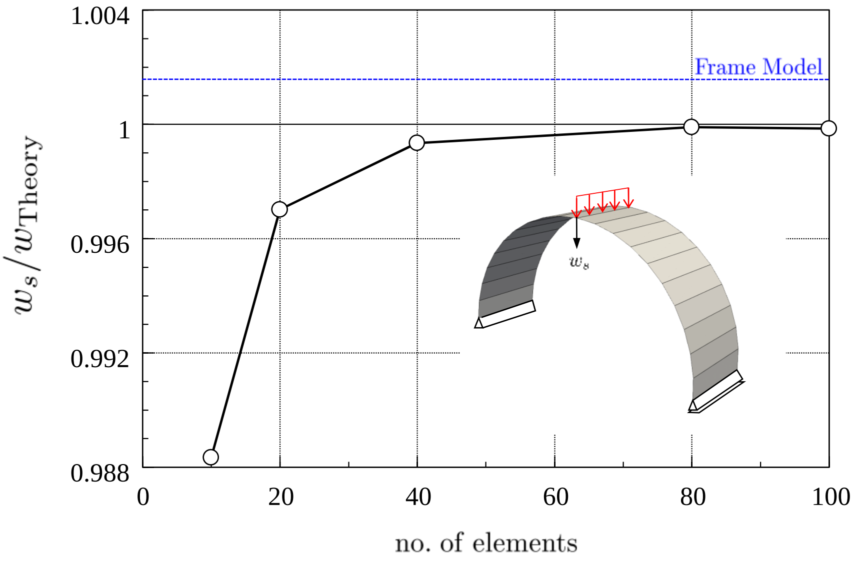

Fig.2.4.13 Convergence of the displacement solution by number of elements

Figure 2.4.14 shows the displacement mode when the number of element divisions is 40. As a scale, the displacement is multiplied by 5. Figure 2.4.15 shows color contours of the vertical displacement distribution. It can be seen that an appropriate coordinate transformation is applied in the curved portion.

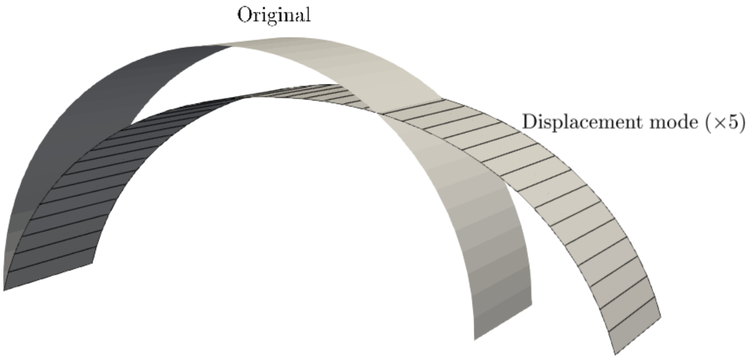

Fig.2.4.14 Distribution of vertical displacements

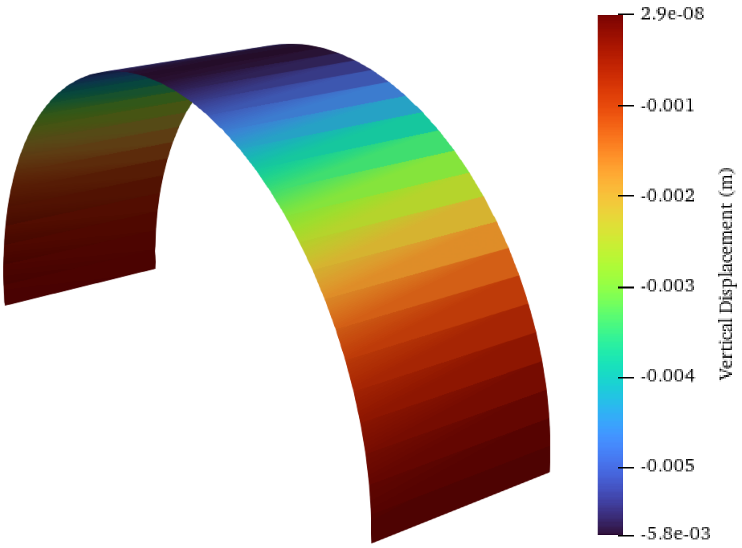

Fig.2.4.15 Color contours for the distribution of vertical displacements

3 DISCRETE LIMIT ANALYSIS OF FLAT SHELL STRUCTURE

3.1 Failure Criterion and Constitutive Equation for Penalty Function

3.1.1 *Constitutive Equation for Surface Force*

HPM deals with fracture using two parameters, stress in the element and surface force on the element boundary. In this section, yield conditions were induced for surface forces on element boundaries such as hinges and slips. The constitutive law and nonlinear analysis method use the surface force at the boundary of adjacent elements; thus, they are nearly the same as the nonlinear analysis of RBSM [27].

If the surface force between the elements is represented by $\boldsymbol{\lambda}$, the yield function f can be expressed as follows:

$$f(\boldsymbol{\lambda}) = 0 \tag{3.1.1}$$

The plastic potential Q is expressed in the same way as

$$Q(\boldsymbol{\lambda}) = 0 \tag{3.1.2}$$

The general plastic flow rule is expressed by the relationship between stress and strain, but HPM uses the surface force per unit area and relative displacement. Therefore, the increment $\Delta\boldsymbol{\delta}^p$ of the relative displacement after plasticization is considered as follows:

$$\Delta\boldsymbol{\delta}^p = \mu \frac{\partial Q}{\partial \boldsymbol{\lambda}} \tag{3.1.3}$$

Here, Δ indicates an incremental quantity, and p in the superscript indicates a plastic state quantity. If the value before plasticization is expressed by the attached e, the total relative displacement is expressed as follows:

$$\Delta\boldsymbol{\delta}^e = \Delta\boldsymbol{\delta} - \Delta\boldsymbol{\delta}^p \tag{3.1.4}$$

Moreover, the relationship between the surface force before plasticization and relative displacement is expressed as

$$\boldsymbol{\lambda} = \boldsymbol{k}^e \cdot \boldsymbol{\delta}^e \tag{3.1.5}$$

From these relationships, the incremental surface force $\Delta\boldsymbol{\lambda}$ can be obtained as

$$\Delta\boldsymbol{\lambda} = \Delta\boldsymbol{k}^e \left(\Delta\delta - \mu \frac{\partial Q}{\partial \boldsymbol{\lambda}} \right) \tag{3.1.6}$$

Here, the plastic condition is expressed as

$$\frac{\partial f}{\partial \boldsymbol{\lambda}} \Delta\boldsymbol{\lambda} = 0 \tag{3.1.7}$$

Substituting Equation (3.1.6) into Equation (3.1.7) and solving for μ gives the following relationship:

$$\mu = \frac{\boldsymbol{k}^e \dfrac{\partial f}{\partial \boldsymbol{\lambda}} \Delta\boldsymbol{\delta}}{\dfrac{\partial f}{\partial \boldsymbol{\lambda}} \boldsymbol{k}^e \dfrac{\partial Q}{\partial \boldsymbol{\lambda}}} \tag{3.1.8}$$

When the μ value represented by Equation (3.1.8) becomes negative in the plastic state, it becomes the unloading state, and when the μ value becomes positive in the unloading state, it becomes the reloading state.

(plastic state) $\mu < 0$ → unloading state

(unloading state) $\mu > 0$ → reloading state

From the above relationship, the relationship between the incremental surface force and incremental relative displacement with respect to the element boundary after plasticization can be obtained as follows:

$$\Delta\boldsymbol{\lambda} = \left(\boldsymbol{k}^e - \frac{\boldsymbol{k}^e \dfrac{\partial f}{\partial \boldsymbol{\lambda}} \dfrac{\partial Q}{\partial \boldsymbol{\lambda}} \boldsymbol{k}^e}{\dfrac{\partial f}{\partial \boldsymbol{\lambda}} \boldsymbol{k}^e \dfrac{\partial Q}{\partial \boldsymbol{\lambda}}} \right) \Delta\delta \tag{3.1.9}$$

When the associated flow rule is applied in Equation (3.1.9), the relationship between the yield function and plastic potential is expressed as

$$f \equiv Q \tag{3.1.10}$$

3.1.2 *Hinge Condition*

Let $\boldsymbol{k}^{ep}$ be in the parentheses in Equation (3.1.9); the post-plasticized constitutive matrix for various fracture conditions is found by assuming the associated flow rule.

The surface force $\boldsymbol{\lambda}^{(a)}_{<ab>}$ of the flat shell problem is defined by Equation (2.3.70), which is rewritten here as follows:

$$\boldsymbol{\lambda}^{(a)}_{<ab>} = \lfloor \boldsymbol{\lambda}^{(a)}_{N<ab>} \quad \boldsymbol{\lambda}^{(a)}_{\theta<ab>} \rfloor^{t} \tag{3.1.11}$$

Here, the surface force representing the moment is $\boldsymbol{\lambda}^{(a)}_{\theta<ab>}$, which is expressed by Equation (2.3.72) and rewritten as follows:

$$\boldsymbol{\lambda}^{(a)}_{\theta<ab>} = \lfloor \lambda^{(a)}_{\theta_s<ab>} \quad \lambda^{(a)}_{\theta_n<ab>} \rfloor^{t} \tag{3.1.12}$$

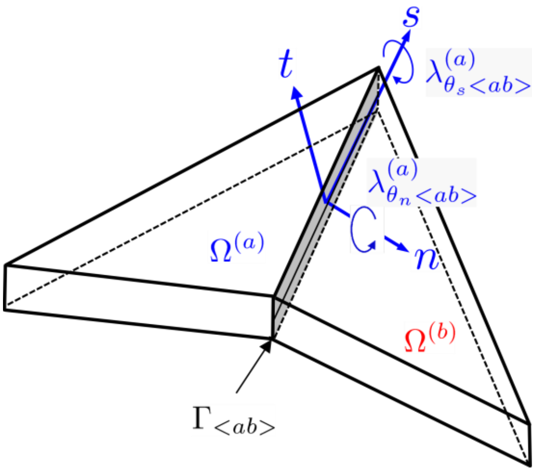

Fig.3.1.1 Moment at an element boundary

Each component of Equation (3.1.12) is shown in Figure 3.1.1. As shown in the figure, $\lambda^{(a)}_{\theta_s<ab>}$ is the component of the bending moment, and $\lambda^{(a)}_{\theta_n<ab>}$ is the component of the torsional moment.

The yield function owing to the moment is expressed as

$$f\left(\boldsymbol{\lambda}_{\theta}\right)=0 \tag{3.1.13}$$

Now, it is assumed that the hinge in the flat shell is caused by the bending moment.

$$f=\frac{\lambda_{\theta_s<ab>}^{(a)}}{M_y}-1 \tag{3.1.14}$$

Here, M_y represents the total plastic moment.

Therefore, the penalty matrix after the hinge generation for the represented penalty matrix in Equation (2.3.75) is expressed from Equation (3.1.9) as follows:

$$\boldsymbol{k}_{\theta}^{ep}=\begin{bmatrix}0 & 0\\ 0 & k_t\end{bmatrix} \tag{3.1.15}$$

In the elastic state constitutive Equation (2.3.75) the penalty function related to bending is set to 0, which implies that the transmission of the bending moment is blocked.

3.1.3 *Slip Condition*

In this section, the constitutive equation of slip fracture is described as the fracture condition due to the surface force in the plane.

1) Mohr–Coulomb condition

In the case of the in-plane problem, the yield condition is expressed by two surface forces $\left(\lambda_{s<ab>}^{(a)}\ ,\ \lambda_{n<ab>}^{(a)}\right)$ in the normal and tangential directions, as shown in Figure 3.1.2.

Therefore, the yield function has the following form:

$$f\left(\lambda_{s<ab>}^{(a)}\ ,\ \lambda_{n<ab>}^{(a)}\right)=0 \tag{3.1.16}$$

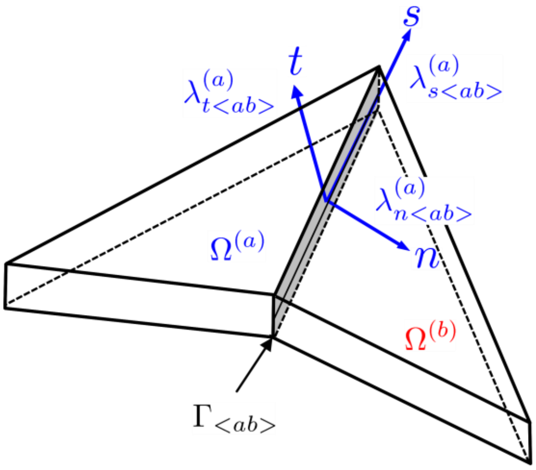

Fig.3.1.2 Surface force at an element boundary for the in-plane problem

As shown in Figure 3.1.3, when the Mohr–Coulomb condition is used as the fracture condition, Equation (3.1.16) is expressed as

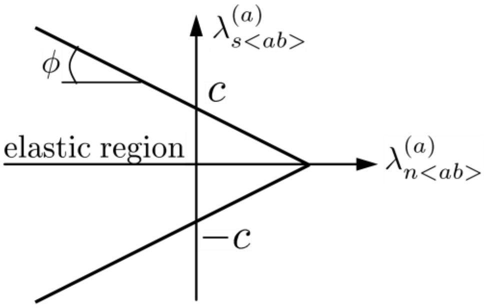

Fig.3.1.3 Mohr–Coulomb condition

$$f = \left(\lambda^{(a)}_{s<ab>}\right)^2 - \left(c - \lambda^{(a)}_{n<ab>} \tan\phi\right)^2 \tag{3.1.17}$$

Here, C is the shear strength (cohesion), and ϕ is the internal friction angle. Subsequently, the constitutive matrix $\boldsymbol{k}^{ep}$ after plasticization, shown in Equation (3.1.9), is expressed as

$$\boldsymbol{k}^{ep}_{\theta} = \begin{bmatrix} k_s & 0 \\ 0 & k_n \end{bmatrix} - \frac{1}{F}\begin{bmatrix} k_s^2(\lambda^{(a)}_{s<ab>})^2 & k_s k_n (c - \lambda^{(a)}_{n<ab>} \tan\phi)\tan\phi \\ \text{sym.} & k_n^2\{(c - \lambda^{(a)}_{n<ab>} \tan\phi)\tan\phi\}^2 \end{bmatrix}, \tag{3.1.18}$$

where

$$F = k_s \lambda^{(a)}_{s<ab>} + k_n\{(c - \lambda^{(a)}_{n<ab>} \tan\phi)\tan\phi\}^2. \tag{3.1.19}$$

Unloading and reloading are determined using μ represented by Equation (3.1.8). The value of the Mohr–Coulomb condition in the in-plane problem is

$$\mu = \frac{1}{F}\left\{k_s \lambda^{(a)}_{s<ab>} \cdot \Delta\delta^{(a)}_{s<ab>} + k_n (c - \lambda^{(a)}_{n<ab>} \tan\phi) \tan\phi \cdot \Delta\delta^{(a)}_{n<ab>}\right\} \quad (3.1.20)$$

However, the surface force of the flat shell problem shown in Figure 3.1.2 includes $\lambda^{(a)}_{t<ab>}$ as shown in Equation (2.3.70), which is rewritten as follows:

$$\boldsymbol{\lambda}^{(a)}_{N<ab>} = \lfloor \lambda^{(a)}_{s<ab>} \quad \lambda^{(a)}_{t<ab>} \quad \lambda^{(a)}_{n<ab>} \rfloor^t \quad (3.1.21)$$

Thus, the surface force of the flat shell problem matches the surface force of the three-dimensional problem. In the case of a three-dimensional problem, the relative displacement of surface force in the shear direction has a combined relationship as shown in Figure 3.1.4

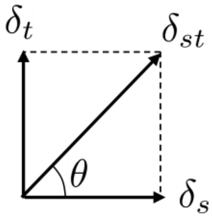

Fig.3.1.4 Relationship of shear direction in the 3D problem

These relationship can be represented in the matrix form as

$$\left\{\begin{array}{c} \delta_{st} \\ \delta_n \end{array}\right\} = \left[\begin{array}{ccc} \cos\theta & \sin\theta & 0 \\ 0 & 0 & 1 \end{array}\right] \left\{\begin{array}{c} \delta_s \\ \delta_t \\ \delta_n \end{array}\right\} \quad (3.1.22)$$

The transformation matrix of Equation (3.1.22) is applied to the second term on the right-hand side of Equation (3.1.18).

$$\boldsymbol{k}^p = \left[\begin{array}{cc} \cos\theta & 0 \\ \sin\theta & 0 \\ 0 & 1 \end{array}\right] \left[\begin{array}{cc} k_{11} & k_{12} \\ k_{12} & k_{22} \end{array}\right] \left[\begin{array}{ccc} \cos\theta & \sin\theta & 0 \\ 0 & 0 & 1 \end{array}\right] = \left[\begin{array}{ccc} k^p_{11} & k^p_{12} & k^p_{13} \\ & k^p_{22} & k^p_{23} \\ \text{sym.} & & k^p_{33} \end{array}\right]$$

(3.1.23)

Here, k_{11} , k_{12} , k_{22} are the components of the second term on the right-hand side of Equation (3.1.18), and $\boldsymbol{k}^{ep}$ is expressed as follows:

$$\boldsymbol{k}^{ep} = \begin{bmatrix} k_s & 0 & 0 \\ 0 & k_t & 0 \\ 0 & 0 & k_n \end{bmatrix} - \begin{bmatrix} k_{11}^p & k_{12}^p & k_{13}^p \\ & k_{22}^p & k_{23}^p \\ \text{sym.} & & k_{33}^p \end{bmatrix} \tag{3.1.24}$$

For unloading and reloading, we use δ_{st} expressed in Equation (3.1.22) instead of $\Delta\delta_{s<ab>}^{(a)}$ in Equation (3.1.20).

$$\mu = \frac{1}{F}\left\{k_s \lambda_{st<ab>}^{(a)} \cdot \Delta\delta_{st<ab>}^{(a)} + k_n (c - \lambda_{n<ab>}^{(a)} \tan\phi) \tan\phi \cdot \Delta\delta_{n<ab>}^{(a)}\right\} \tag{3.1.25}$$

2) Mises condition

The Mises condition for slip fracture between elements can be expressed by the relationship shown in Figure 3.1.5. The yield function of Equation (3.1.16) is expressed as follows:

$$f = \left(\lambda_{s<ab>}^{(a)}\right)^2 + \frac{1}{4}\left(\lambda_{n<ab>}^{(a)}\right)^2 - \sigma_y \tag{3.1.26}$$

Here, σ_y is the yield stress corresponding to *c* in the figure.

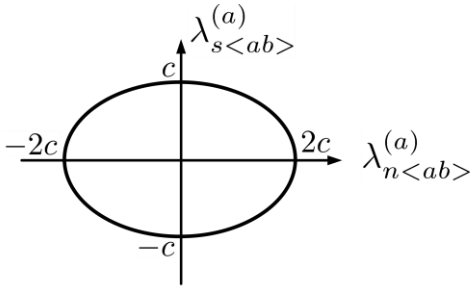

Fig.3.1.5 Mises condition

In the case of a two-dimensional problem, $\boldsymbol{k}^{ep}$ shown in Equation (3.1.9) is expressed as follows:

$$\boldsymbol{k}^{ep} = \boldsymbol{k}^e - \boldsymbol{k}^p \tag{3.1.27}$$

$$\boldsymbol{k}^e = \left[\begin{array}{cc} k_s & 0 \\ 0 & k_n \end{array} \right] \quad \boldsymbol{k}^p = \frac{1}{F} \left[\begin{array}{cc} 4k_s^2(\lambda^{(a)}_{n<ab>})^2 & k_n k_s \lambda^{(a)}_{s<ab>} \lambda^{(a)}_{n<ab>} \\ \text{sym.} & \frac{1}{4} k_n^2 (\lambda^{(a)}_{n<ab>})^2 \end{array} \right],$$

where

$$F = 4k_s \left(\lambda^{(a)}_{s<ab>} \right)^2 + \frac{k_n}{4} \left(\lambda^{(a)}_{n<ab>} \right)^2. \tag{3.1.28}$$

Unloading and reloading are determined using μ represented by Equation (3.1.8). The value of the Mises condition in the in-plane problem is

$$\mu = \frac{1}{F} \left(2k_s \lambda^{(a)}_{s<ab>} \Delta\delta^{(a)}_{s<ab>} + k_n \frac{\lambda^{(a)}_{n<ab>}}{2} \Delta\delta^{(a)}_{n<ab>} \right) \tag{3.1.29}$$

In the case of three dimensions, the relations of Equations (3.1.22)–(3.1.24) are applied using the combined relative displacement and surface force in the shear direction, same as the Mohr–Coulomb condition. In addition, unloading and reloading are determined using the following relationship.

$$\mu = \frac{1}{F} \left(2k_s \lambda^{(a)}_{s<ab>} \Delta\delta^{(a)}_{st<ab>} + k_n \frac{\lambda^{(a)}_{n<ab>}}{2} \Delta\delta^{(a)}_{n<ab>} \right) \tag{3.1.30}$$

3.2 Progressive Failure Condition and Release Force

3.2.1 *Crack Condition*

Fracture dealt in this section is a phenomenon that involves the release of the retained surface force in addition to the interruption of force transmission. The fracture patterns dealt with in this section are caused by three cases: bending moment, shearing force, and tensile force.

(1) Bending Fracture

In the hinge condition dealt with in Section 3.1, after the bending moment at the element boundary reaches the total plastic moment, as shown by the dotted line in Figure 3.2.1, the force transmission is cut off and total plastic moment is maintained. Whereas, the bending fracture dealt with here releases the surface force of the moment after the bending moment reaches the total plastic moment, as shown by the solid line in Figure 3.2.1.

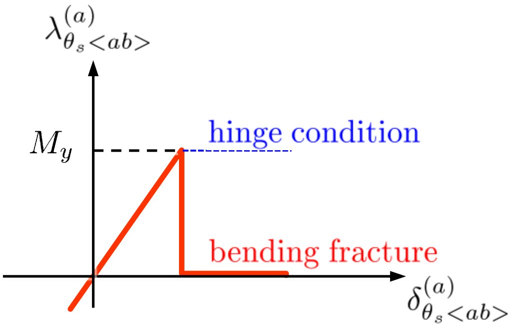

Fig.3.2.1 Hinge condition and bending fracture

Therefore, the failure criterion is the same as the hinge condition in Equation (3.1.14), defined as follows:

$$f = \frac{\lambda^{(a)}_{\theta_s<ab>}}{M_y} - 1 \qquad (3.2.1)$$

After the failure, the release force (Section 3.2.2) is applied, and the constitutive matrix involved in bending is set to 0; this relationship is expressed as follows:

$$\Delta\boldsymbol{\lambda}^{(a)}_{\theta<ab>} = \boldsymbol{k}^{ep}_{\theta}\Delta\boldsymbol{\delta}^{(a)}_{\theta<ab>} \qquad (3.2.2)$$

$$\boldsymbol{k}_{\theta}^{ep} = \begin{bmatrix} 0 & 0 \\ 0 & 0 \end{bmatrix} \tag{3.2.3}$$

(2) Shear Failure

In the case of slip fracture explained in Section 3.1, the surface force after fracture moves on the fracture surface according to the flow rule. In the shear fracture dealt with in this paper, after the surface force reaches the fracture condition shown in Figure 3.2.2, the stress is released by the method described in Section 3.2.2, and the force transmission is blocked.

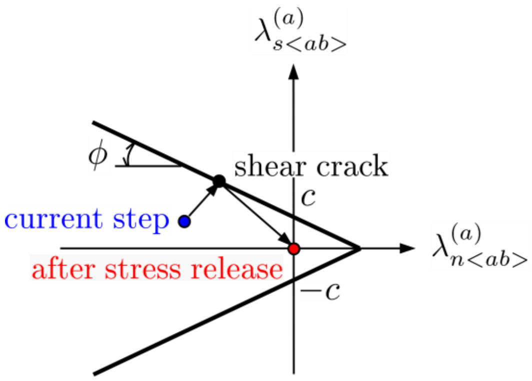

Fig.3.2.2 Stress path for shear crack

Figure 3.2.2 shows the following Mohr–Coulomb failure conditions:

$$f = \left(\lambda_{st<ab>}^{(a)}\right)^2 - \left(c - \lambda_{n<ab>}^{(a)} \tan\phi\right)^2 \tag{3.2.4}$$

However, $\lambda_{st<ab>}^{(a)}$ represents the resultant force of the two shear surface forces $\lambda_{s<ab>}^{(a)}$ and $\lambda_{t<ab>}^{(a)}$, as shown in Equation (3.1.22).

After the failure, the release force shown in Section 3.2.2 is applied, and the constitutive matrix involved in shearing is set to 0; this relationship is expressed as follows:

$$\Delta\boldsymbol{\lambda}_{N<ab>}^{(a)} = \boldsymbol{k}_{N_s}^{ep} \Delta\boldsymbol{\delta}_{N<ab>}^{(a)} \tag{3.2.5}$$

$$\boldsymbol{k}_{N_s}^{ep} = \begin{bmatrix} 0 & 0 & 0 \\ 0 & 0 & 0 \\ 0 & 0 & k_n \end{bmatrix} \tag{3.2.6}$$

As shown in Equation (3.2.6), it is assumed that shear failure occurs in the compressed state, and the normal direction penalty of the element boundary surface remains.

If the fracture condition is the Mises condition shown in Figure 3.1.5 and Equation (3.1.26), the following fracture condition is used for judgment:

$$f = \left(\lambda_{st<ab>}^{(a)}\right)^2 + \frac{1}{4}\left(\lambda_{n<ab>}^{(a)}\right)^2 - \sigma_y \tag{3.2.7}$$

Subsequently, the same coefficient matrix as in Equation (3.2.6) is used, and the transmission of force in the shear direction is blocked.

(3) Tensile Crack

Under tensile fracture conditions, tensile fracture occurs when $\lambda_{n<ab>}^{(a)}$ exceeds the tensile strength F_t. As shown in Figure 3.2.3, when the tensile surface force exceeds the allowable tensile force, the surface force of the element boundary surface is released by the method described in Section 3.2.2. Subsequently, the value of the penalty function is set to 0, so that the surface force is not transmitted.

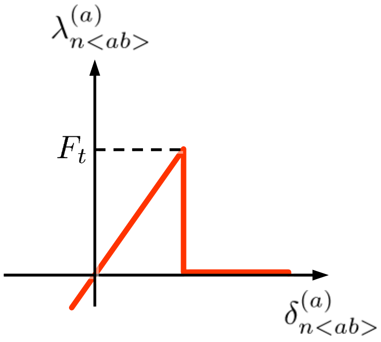

Fig.3.2.3 Tensile crack

The tensile fracture condition is expressed as follows:

$$f = \frac{\lambda_{n<ab>}^{(a)}}{F_t} - 1 \tag{3.2.8}$$

The constituent matrix after failure is expressed as

$$\Delta\boldsymbol{\lambda}_{N<ab>}^{(a)} = \boldsymbol{k}_{N_n}^{ep}\Delta\boldsymbol{\delta}_{N<ab>}^{(a)} \tag{3.2.9}$$

$$\boldsymbol{k}_{N_n}^{ep} = \begin{bmatrix} 0 & 0 & 0 \\ 0 & 0 & 0 \\ 0 & 0 & 0 \end{bmatrix} \qquad (3.2.10)$$

In the case of a tensile crack, the fracture surface becomes an opening surface; therefore, it is necessary to not only release the tensile surface force but also the surface forces to block the transmission. That is, assuming that bending fracture occurs at the same time, Equations (3.2.2) and (3.2.3) are also applied.

3.2.2 *Release Force*

In this study, the release of surface force is simply the total release. The release force $\boldsymbol{F}_{<ab>}$ at the elementary boundary $\Gamma_{<ab>}$ is obtained as follows:

$$\boldsymbol{F}_{<ab>} = -\int_{\Gamma_{<ab>}} \boldsymbol{B}_{<ab>} \boldsymbol{\lambda}_{<ab>} dS \; , \qquad (3.2.11)$$

Where $\boldsymbol{\lambda}_{<ab>}$ is the surface force, and $\boldsymbol{B}_{<ab>}$ is the matrix that relates the relative displacement and degree of freedom of the element. $\boldsymbol{B}_{<ab>}$ can be decomposed for each subregion $\Omega^{(a)}$ and $\Omega^{(b)}$ as follows:

$$\boldsymbol{B}_{<ab>} = \lfloor \boldsymbol{B}_{<ab>}^{(a)}, \boldsymbol{B}_{<ab>}^{(b)} \rfloor^{t} \qquad (3.2.12)$$

Let $\boldsymbol{F}_{<ab>}^{(a)}$ and $\boldsymbol{F}_{<ab>}^{(b)}$ be the release forces acting on the centroids of the regions $\Omega^{(a)}$ and $\Omega^{(b)}$, respectively, adjacent to the boundary surface $\Gamma_{<ab>}$. Then, the following relationship can be obtained from Equation (3.2.12):

$$\begin{Bmatrix} \boldsymbol{F}_{<ab>}^{(a)} \\ \boldsymbol{F}_{<ab>}^{(b)} \end{Bmatrix} = -\int_{\Gamma_{<ab>}} \begin{bmatrix} \boldsymbol{B}_{<ab>}^{(a)} \\ \boldsymbol{B}_{<ab>}^{(b)} \end{bmatrix} \boldsymbol{\lambda}_{<ab>} dS \qquad (3.2.13)$$

(1) Release force of a bending fracture

In the case of bending fracture, the surface force related to bending shown in Equation (2.3.72) is released, which is reproduced below.

$$\boldsymbol{\lambda}^{(a)}_{\theta<ab>} = \lfloor \lambda^{(a)}_{\theta_s<ab>} \quad \lambda^{(a)}_{\theta_n<ab>} \rfloor^t \tag{3.2.14}$$

$\boldsymbol{B}_{<ab>}$ related to bending is shown in Equation (2.3.67), which is reproduced below.

$$\boldsymbol{B}_{\theta<ab>} = \lfloor \boldsymbol{R}^{(a)}_{<ab>} \boldsymbol{N}^{(a)}_{\theta<ab>} \quad \boldsymbol{R}^{(b)}_{<ab>} \boldsymbol{N}^{(b)}_{\theta<ab>} \rfloor \tag{3.2.15}$$

From the above relationship, the release forces $\boldsymbol{F}^{(a)}_{<ab>}$ and $\boldsymbol{F}^{(b)}_{<ab>}$ related to bending fracture can be obtained from Equation (3.2.13) as follows:

$$\left\{ \begin{array}{c} \boldsymbol{F}^{(a)}_{<ab>} \\ \boldsymbol{F}^{(b)}_{<ab>} \end{array} \right\} = -\int_{\Gamma_{<ab>}} \left[\begin{array}{c} \boldsymbol{R}^{(a)}_{<ab>} \boldsymbol{N}^{(a)}_{\theta_s<ab>} \\ \boldsymbol{R}^{(b)}_{<ab>} \boldsymbol{N}^{(b)}_{\theta_s<ab>} \end{array} \right] \boldsymbol{\lambda}^{(a)}_{\theta<ab>} dS \tag{3.2.16}$$

(2) Release force of a shear failure

In the case of shear failure, the three-dimensional surface force shown in Equation (2.3.71) is released; Equation (2.3.71) is reproduced below.

$$\boldsymbol{\lambda}^{(a)}_{N<ab>} = \lfloor \lambda^{(a)}_{s<ab>} \quad \lambda^{(a)}_{t<ab>} \quad \lambda^{(a)}_{n<ab>} \rfloor^t \tag{3.2.17}$$

Moreover, $\boldsymbol{B}_{<ab>}$ of shear failure is shown in Equation (2.3.63), which is reprinted below.

$$\boldsymbol{B}_{N<ab>} = \lfloor \boldsymbol{R}^{(a)}_{<ab>} \boldsymbol{N}^{(a)}_{<ab>} \quad \boldsymbol{R}^{(b)}_{<ab>} \boldsymbol{R}^{(a)}_{x} \left(\boldsymbol{R}^{(b)}_{x} \right)^{-1} \boldsymbol{N}^{(b)}_{<ab>} \rfloor \tag{3.2.18}$$

From the above relationship, the release forces $\boldsymbol{F}^{(a)}_{<ab>}$ and $\boldsymbol{F}^{(b)}_{<ab>}$ related to shear fracture can be obtained from Equation (3.1.13) as follows:

$$\left\{ \begin{array}{c} \boldsymbol{F}^{(a)}_{<ab>} \\ \boldsymbol{F}^{(b)}_{<ab>} \end{array} \right\} = -\int_{\Gamma_{<ab>}} \left[\begin{array}{c} \boldsymbol{R}^{(a)}_{<ab>} \boldsymbol{N}^{(a)}_{<ab>} \\ \boldsymbol{R}^{(b)}_{<ab>} \boldsymbol{R}^{(a)}_{x} \left(\boldsymbol{R}^{(b)}_{x} \right)^{-1} \boldsymbol{N}^{(b)}_{<ab>} \end{array} \right] \boldsymbol{\lambda}^{(a)}_{N<ab>} dS \tag{3.2.19}$$

(3) Release force of a tensile crack

In the case of a tensile crack, in addition to the surface force shown in Equation (3.2.19), the surface force shown in Equation (3.2.16) is also released. Therefore, the release force in this case is expressed as follows:

$$\begin{Bmatrix} \boldsymbol{F}^{(a)}_{<ab>} \\ \boldsymbol{F}^{(b)}_{<ab>} \end{Bmatrix} = -\int_{\Gamma_{<ab>}} \begin{bmatrix} \boldsymbol{R}^{(a)}_{<ab>} \boldsymbol{N}^{(a)}_{\theta_s <ab>} \\ \boldsymbol{R}^{(b)}_{<ab>} \boldsymbol{N}^{(b)}_{\theta_s <ab>} \end{bmatrix} \boldsymbol{\lambda}^{(a)}_{\theta <ab>} dS$$

$$- \int_{\Gamma_{<ab>}} \begin{bmatrix} \boldsymbol{R}^{(a)}_{<ab>} \boldsymbol{N}^{(a)}_{<ab>} \\ \boldsymbol{R}^{(b)}_{<ab>} \boldsymbol{R}^{(a)}_{x} \left(\boldsymbol{R}^{(b)}_{x} \right)^{-1} \boldsymbol{N}^{(b)}_{<ab>} \end{bmatrix} \boldsymbol{\lambda}^{(a)}_{N <ab>} dS \qquad (3.2.20)$$

3.3 Algorithm for Material Nonlinear Analysis

3.3.1 *Load Incremental Method using r-min Method*

In this study, the r-min method [33] of the load increment method was used for the nonlinear analysis. This method searches for the first yielding boundary among the element boundaries and automatically determines the rate of load increment required for that boundary to yield. The found element boundaries are yielded, and incremental loads applied sequentially. The following is the algorithm for this method.

1) Classify boundaries into plasticized and non-plasticized element boundaries at the beginning of the incremental stage. For the plasticized element boundaries, a total coefficient matrix is constructed using a penalty matrix that considers plasticity.
2) For the given load increment, solve the coefficient matrix made in (1), and compute the incremental surface force. The resulting surface force is added to the previous surface force, and the increment rate r_{min} is computed such that all of the surface force is equal to or less than the yield strength.
3) The surface force at this stage is obtained by multiplying the incremental surface force by the load increment rate obtained in (2) and adding it to the previous surface force. Here, the surface force that has reached the yield strength follows the plastic flow rule.
4) Repeat steps (1)–(3) until the total load increment reaches the acting load.

Problems involving plastic deformation focus on when the surface force in the elastic state yields to the plastic state. Figure 3.3.1 shows a conceptual diagram for explaining the load increment rate; P is the position of the surface force up to the previous time, and R is the position where the incremental surface force obtained at the current time and the previous surface force is added. That is, the incremental surface force of the current time is PR. If R clearly exceeds point Q of the initial yield surface, it implies that an extra surface force QR is acting. Therefore, the surface force in R is returned to the position of Q, and only the elastic part of PQ is left. For this purpose, the following load increment rate is used.

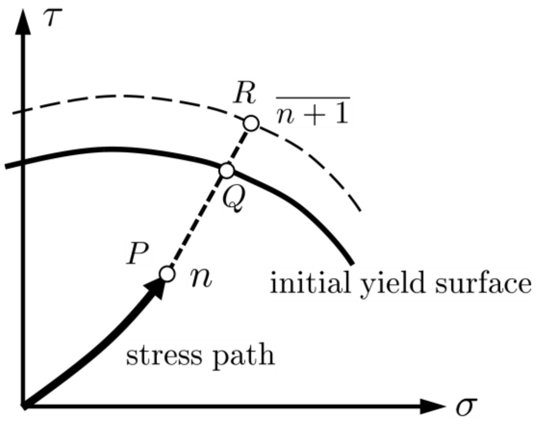

Fig.3.3.1 Rate of load increment

$$r = \frac{\mathrm{PQ}}{\mathrm{PR}} \tag{3.3.1}$$

If the value obtained by multiplying the incremental surface force by the rate of load increment *r* is added to the previous surface force, the surface force does not exceed the yield surface. Computing this rate of load increment r for all element boundaries, the smallest one, $r_{\min}$, is set as the current rate of load increment.

For nonlinear analysis, the load $\boldsymbol{P}_s$ is divided into several incremental loads $\Delta\boldsymbol{P}_s$. For this incremental load, the rate of load increment up to the i-1th step is found according to the $r_{\min}$ method, and the total is set as $r_{\min}$. As a result, the total load applied up to the i-1th step is $r_{\min}\Delta\boldsymbol{P}_s$. Therefore, the load to be loaded in the i-step is as follows:

$$\Delta\boldsymbol{P}_s^{(i)} = (1 - r_{\min})\Delta\boldsymbol{P}_s \tag{3.3.2}$$

Next, if the rate of load increment obtained by applying this load $\Delta\boldsymbol{P}_s^{(i)}$ is r_i, the load $\Delta\boldsymbol{P}_s^{(i+1)}$ acting in step (i + 1) is given by the following equation:

$$\Delta\boldsymbol{P}_s^{(i+1)} = (1 - r_i)\Delta\boldsymbol{P}_s^{(i)} \tag{3.3.3}$$

Therefore, assuming that the load applied at the beginning is $\Delta\boldsymbol{P}_s$, the load $\Delta\boldsymbol{P}_s^{(n)}$ applied in the nth step is as follows:

$$\Delta\boldsymbol{P}_s^{(n)} = \prod_{i=0}^{n-1}(1 - r_i)\Delta\boldsymbol{P}_s \quad (r_0 = 0) \tag{3.3.4}$$

The uppermost part of Figure 3.3.2 is a conceptual diagram showing the relationship of Equation (3.3.4).

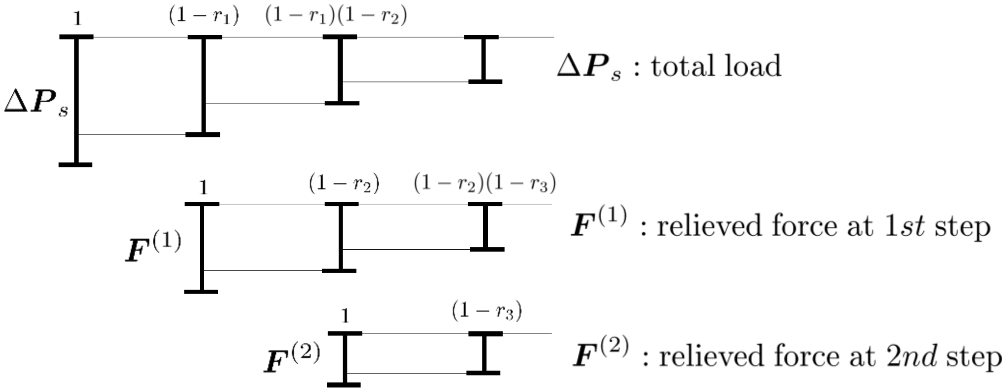

Fig.3.3.2 Concept of the rate of load increment

Assuming the case where tension or shear cracks occur at the element boundary in the (k-1) load step, at the element boundary where cracks occur, the value of the penalty function is set to 0 to block the transmission of surface force. The surface force at the element boundary is distributed to the related subregions as a release force $\Delta \boldsymbol{F}^{(k-1)}$. The release force at the S$^{\text{th}}$ element boundary is computed by the following equation:

$$\boldsymbol{F}_{<s>} = -\int_{\Gamma_{<s>}} \left({}^t\boldsymbol{B}_{N<s>} \boldsymbol{\lambda}_{N<s>} + {}^t\boldsymbol{B}_{\theta<s>} \boldsymbol{\lambda}_{\theta<s>} \right) d\Gamma \tag{3.3.5}$$

As shown in Figure 3.3.2, the distributed release force is applied to the next load step, and the incremental computation is analyzed based on those loads. Thus, the incremental load is computed as follows:

$$\Delta \boldsymbol{P}_s^{(n)} = \prod_{i=0}^{n-1} (1-r_i) \Delta \boldsymbol{P}_s + \sum_{k=1}^{n} \left\{ \prod_{i=0}^{n-1} (1-r_i) \Delta \boldsymbol{F}^{(k-1)} \right\} \tag{3.3.6}$$

The above process is repeated until all the initially applied load and release forces are used up. Then, the total load increment rate is computed as follows:

$$r_{\text{total}} = \sum_{k=1}^{n} \left\{ \prod_{i=0}^{n-1} (1-r_i) r_k \right\} \tag{3.3.7}$$

When this r_{total} becomes 1, the incremental calculation converges. As shown above, this algorithm is similar to the $r_{\min}$ method in the conventional load increment method, except that it gives a release force.

3.3.2 *Rate of Load Increment*

In the nonlinear analysis used in this study, the load increment rate is computed from Equation (3.3.1) for the boundary surface between all the unfractured elements. Assuming that the surface force at the element boundary is $\boldsymbol{\lambda}$, the incremental surface force is $\Delta\boldsymbol{\lambda}$, and the load increment rate is r. The following relationship must be satisfied so that the surface force does not exceed the fracture surface:

$$f(\boldsymbol{\lambda} + r \cdot \Delta\boldsymbol{\lambda}) \geq 0 \tag{3.3.8}$$

For all unfractured surface forces, find r using Equation (3.4.8), and let the minimum value be the current load increment rate.

If the current surface force is $\boldsymbol{\lambda}^{n}$, the surface force $\boldsymbol{\lambda}^{n+1}$ after the increment can be calculated as follows:

$$\boldsymbol{\lambda}^{n+1} = \boldsymbol{\lambda}^{n} + r \cdot \Delta\boldsymbol{\lambda} \tag{3.3.9}$$

The load increment rate for each failure condition is computed below.

(1) Hinge Condition

The hinge condition is expressed by Equation (3.1.14). Applying this to Equation (3.3.8) gives the following:

$$\left(\frac{\lambda^{(a)}_{\theta_s<ab>} + r \cdot \Delta\lambda^{(a)}_{\theta_s<ab>}}{M_y} \right) - 1 \geq 0 \tag{3.3.10}$$

By solving this for r, the load increment rate r for the hinge condition can be obtained as follows:

$$r = \frac{M_y - \lambda^{(a)}_{\theta_s<ab>}}{\Delta\lambda^{(a)}_{\theta_s<ab>}} \tag{3.3.11}$$

(2) Slip Condition (Mohr–Coulomb)

Among the slip conditions, the Mohr–Coulomb condition is expressed by Equation (3.2.4). Applying this to Equation (3.3.8) yields the following:

$$\left(\lambda_{st<ab>}^{(a)} + r \cdot \Delta\lambda_{st<ab>}^{(a)}\right)^2 \leq \left\{c - \left(\lambda_{n<ab>}^{(a)} + r \cdot \Delta\lambda_{n<ab>}^{(a)}\right) \tan\phi\right\}^2 \tag{3.3.12}$$

The load increment rate r can be obtained by solving the following quadratic equation:

$$A \cdot r^2 + B \cdot r + C = 0 \tag{3.3.13}$$

Here, each coefficient is given below.

$$A = \left(\Delta\lambda_{st<ab>}^{(a)}\right)^2 - \left(\Delta\lambda_{n<ab>}^{(a)} \tan\phi\right)^2$$

$$B = 2\left\{\lambda_{st<ab>}^{(a)} \Delta\lambda_{st<ab>}^{(a)} - \left(c - \lambda_{n<ab>}^{(a)} \tan\phi\right) \Delta\lambda_{n<ab>}^{(a)} \tan\phi\right\}$$

$$C = \left(\lambda_{st<ab>}^{(a)}\right)^2 - \left(c - \lambda_{n<ab>}^{(a)} \tan\phi\right)^2$$

(3) Slip Condition (Mises)

Among the slip conditions, the Mises condition is expressed by Equation (3.2.7). Applying this to Equation (3.3.8) yields the following:

$$\left(\lambda_{st<ab>}^{(a)} + r \cdot \Delta\lambda_{st<ab>}^{(a)}\right)^2 + \frac{1}{4}\left(\lambda_{n<ab>}^{(a)} + r \cdot \Delta\lambda_{n<ab>}^{(a)}\right)^2 = \sigma_y \tag{3.3.14}$$

The load increment rate r can be obtained by solving the quadratic equation shown in Equation (3.3.13). Here, each coefficient is given below.

$$A = \left(\Delta\lambda_{st<ab>}^{(a)}\right)^2 + \frac{1}{4}\left(\Delta\lambda_{n<ab>}^{(a)}\right)^2$$

$$B = 2\lambda_{st<ab>}^{(a)} \cdot \Delta\lambda_{st<ab>}^{(a)} + \frac{1}{2}\lambda_{n<ab>}^{(a)} \cdot \Delta\lambda_{n<ab>}^{(a)}$$

$$C = \left(\lambda_{st<ab>}^{(a)}\right)^2 + \frac{1}{4}\left(\lambda_{n<ab>}^{(a)}\right)^2 - \sigma_y$$

(4) Tensile Crack Condition

Assuming that the tensile strength is F_t, the condition of tensile failure is expressed by Equation (3.2.8). Applying this to Equation (3.3.8) yields the following:

$$\left(\frac{\lambda^{(a)}_{n<ab>} + r \cdot \Delta\lambda^{(a)}_{n<ab>}}{F_t} \right) - 1 \geq 0 \tag{3.3.15}$$

By solving this for r, the load increment rate r for the condition of tensile fracture can be obtained as follows:

$$r = \frac{F_t - \lambda^{(a)}_{n<ab>}}{\Delta\lambda^{(a)}_{n<ab>}} \tag{3.3.16}$$

3.3.3 *Analysis Algorithm*

Figure 3.3.3 shows the analysis flowchart of the load increment method proposed in this study. In this method, the stiffness matrix is recreated for each load increment; therefore, the computation process takes time. However, a stable solution can be obtained even under a load state near the collapse load. In addition, the load increment can be calculated from the load increment rate obtained by analysis, and a more accurate collapse load can be obtained.

Four conditions are assumed as factors that determine the load increment rate: plastic hinges, slips, shear cracks, and tensile cracks. These load increment rates are found for all unfractured element boundaries, and the smallest of them is set to the current load increment rate.

For shear cracks and tensile cracks under the four conditions, a process to release the surface force has been added. In this study, the surface force is fully released, but it is also possible to gradually release it by changing the release rate.

The above operation is repeated until the load increment rate $r_{\min}$ is 1; that is, the assumed total load is applied. However, if the mechanism is formed before it becomes 1, the load value at that time becomes the collapse load.

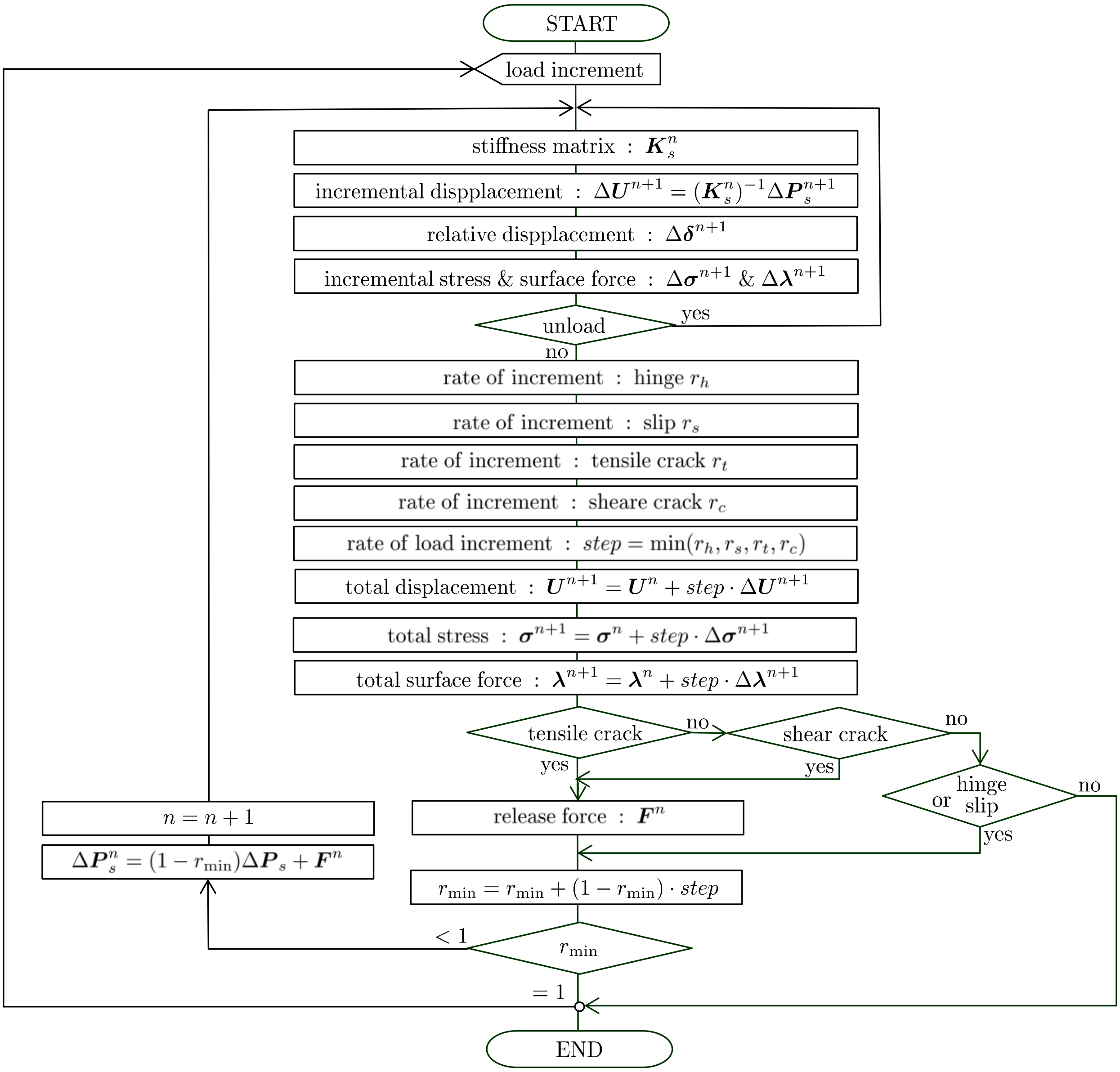

Fig.3.3.3 Flowchart for the load incremental method using the $r_{\min}$ method

3.4 Numerical Examples

3.4.1 *Flat Shell*

As an example of discrete limit analysis, a flat plate shell, in which four sides of a rectangular plate are simply supported, is analyzed. Figure 3.4.1 shows the geometrical properties of the flat plate shell, where $a = 2$ m and thickness $t = 0.1$ m. The mesh division divides the square area into crosses as shown in the figure, and the number of elements is 1024.

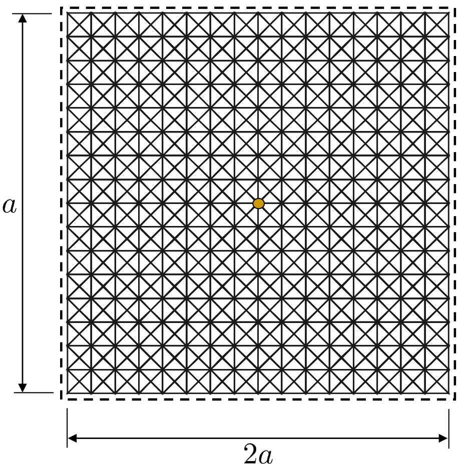

Fig.3.4.1 Model and mesh division of a flat plate shell with simple supports

The material constants used in the analysis are the elastic modulus $E = 1.0 \times 10^6\ \mathrm{N/m^2}$, Poisson's ratio $\nu = 0.0$, and total plastic moment $M_{pn} = 0.1\ \mathrm{Nm/m}$.

(1) Concentrated load

First, we show an example of analysis when a concentrated load $P = 4.0$ N acts on the center of the square plate.

Figure 3.4.2 shows the load–displacement curve; the horizontal axis represents the non-dimensional value of the deflection *w*, and the vertical axis represents the non-dimensional value of the applied load. The circles in the figure represent the results obtained by the present method, and the dashed-dotted line represents the theoretical collapse load. The non-dimensional collapse load obtained by the present method is 8.0, which is the same as its theoretical equivalent.

Figure 3.4.3 shows the hinge line. Figure 3.4.3(a) shows the collapsed state experimentally by A. Sawczuk and T. Jaege [34]; Figure 3.4.3(b) shows the hinge line assumed in the plastic analysis;

Figure 3.4.3(c) shows the progress of the hinge line by the present method. The numbers in the figure are non-dimensional load values. The final mechanism by the present method includes the hinge line assumed in the plastic analysis. Therefore, it is considered that the collapse loads are the same.

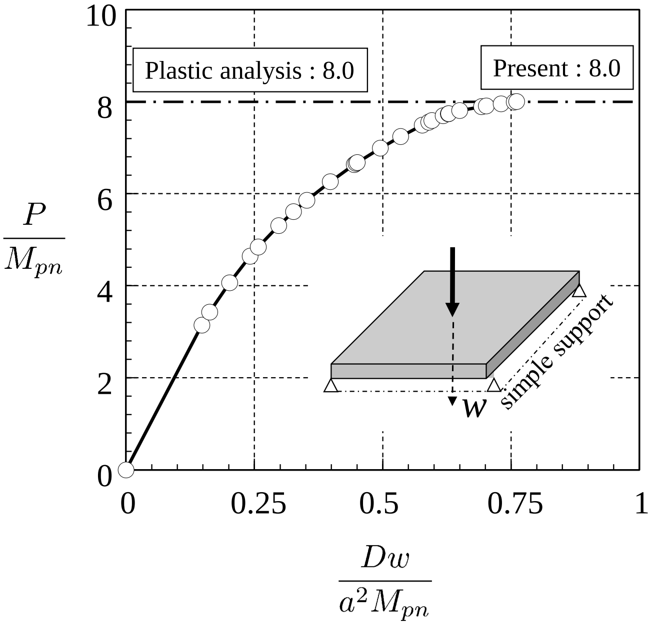

Fig.3.4.2 Load–displacement curve of a flat plate shell with centrally concentrated load

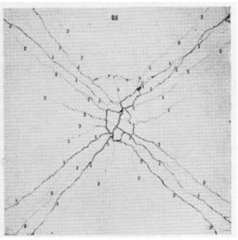

(a) Experiment

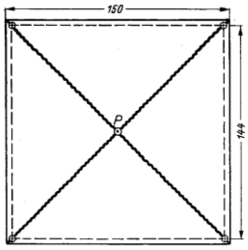

(b) Plastic analysis

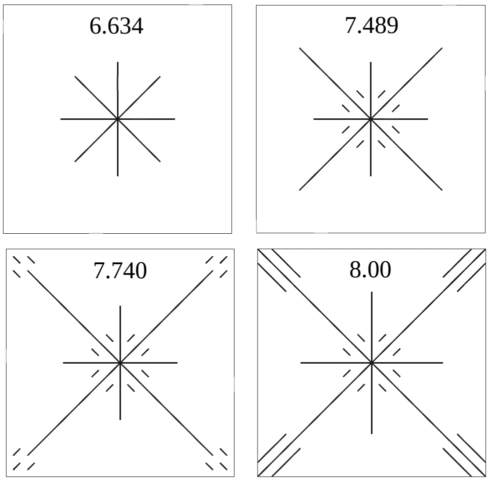

(c) Present method

Fig.3.4.3 Hinge line of a flat plate shell with centrally concentrated load [34]

(2) Distributed load

Next, we show an example of analysis when a distributed load p = 1.0 N/m^2 acts on the surface of the square plate.

Figure 3.4.4 shows the load–displacement curve; the horizontal axis indicates the dimensionless value of deflection, and the vertical axis indicates the non-dimensional value of load. The circles in the figure indicate the results obtained by this method, the dashed-dotted line indicates the collapse load obtained by plastic analysis, and the dashed line indicates the upper and lower-bound solution. The non-dimensional collapse load obtained by the present method is 24.0, which is the same as the collapse load in the plastic analysis.

Figure 3.4.5 shows the hinge line. Figure 3.4.5(a) shows the experimental collapse by A. Sawczuk and T. Jaege [34], similar to the case under concentrated loading. Similarly, Figure 3.4.5(b) shows the hinge line assumed in the plastic analysis. When a concentrated load acts, the hinge line progresses from the center; whereas when a distributed load acts, it progresses from the four corners. Even when distributed loads are applied, the final mechanism by this method includes the hinge line assumed in the plastic analysis. Therefore, even in this case, the collapse loads by plastic analysis and the present method are the same.

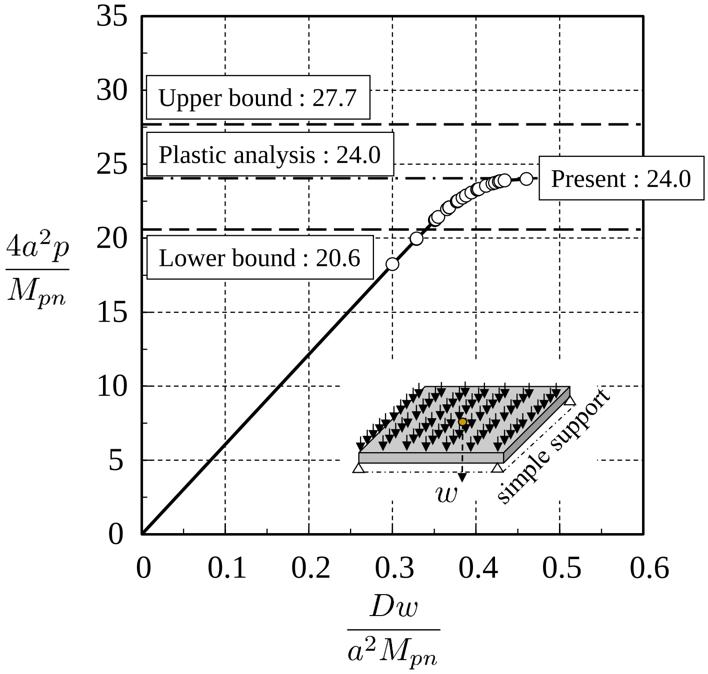

Fig.3.4.4 Load–displacement curve of a flat plate shell with distributed load

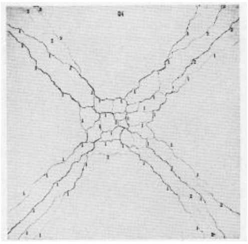

(a)Experiment

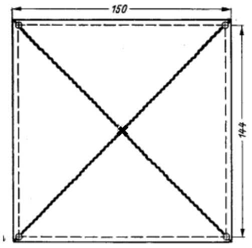

(b)Plastic analysis

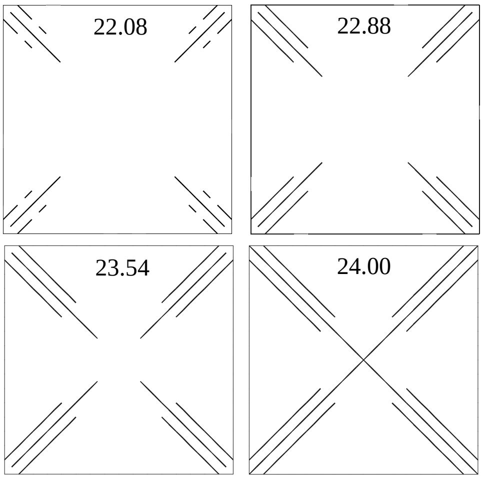

(c)Present method

Fig.3.4.5 Hinge line of a flat plate shell with distributed load [34]

3.4.2 *Portal Frame*

To examine the accuracy of the displacement solution of the proposed flat plate shell model, the results of the verification using a simple model are presented. Figure 3.4.6(a) shows the numerical model of the portal frame under a horizontal load of P = 1 kN/m. As a boundary condition, the lower ends of both the columns are fixed. The dimensions and loads are shown in the figure.

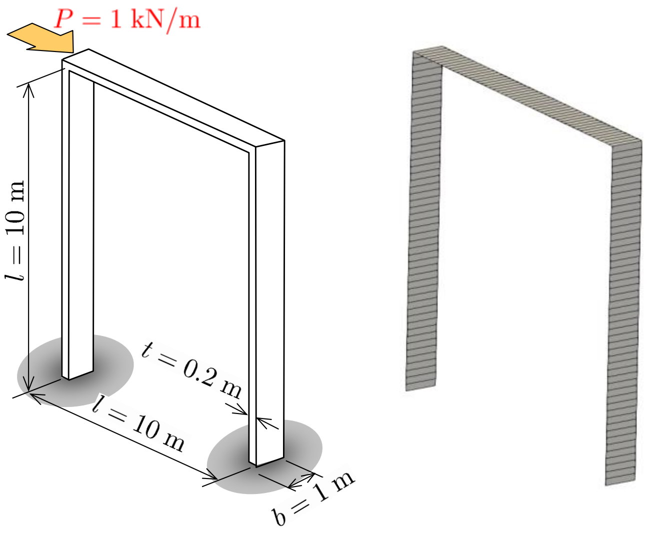

(a) Numerical model (b) Mesh division

Fig.3.4.6 Numerical example

The material has the modulus of elasticity $E = 100$ GPa, Poisson's ratio $\nu = 0$, and full plastic moment $M_y = 2\ \mathrm{kNm}$. A quadrilateral element is used for the mesh division, as shown in Fig. 3.4.6(b), and the displacement field of the in-plane deformation is a linear function. Although the figure shows an example of division of each member into 20 parts, 50 divisions were used in the analysis.

(1) Elastic Analysis

Figure 3.4.7 shows the displacement mode in the elastic analysis; the values in parentheses are the results of the framed structural analysis. The vertical displacements in both the analyses were nearly the same, although the difference between the horizontal displacements was 0.4%.

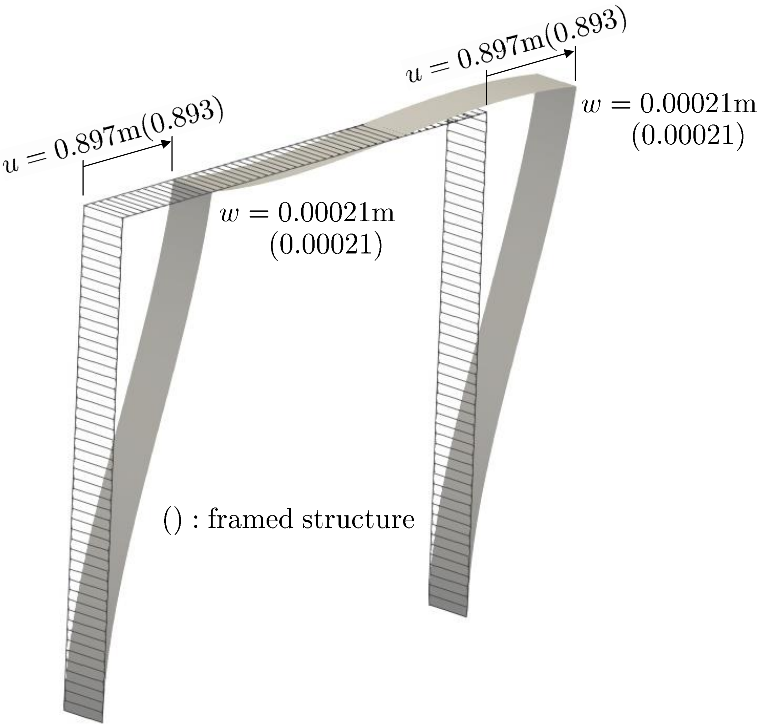

Fig.3.4.7 Displacement mode for the elastic analysis

Figure 3.4.8 shows the distribution of bending moments in the elastic analysis. At all endpoints, there was a difference of 1 or less in the third digit, although the distributions were nearly the same.

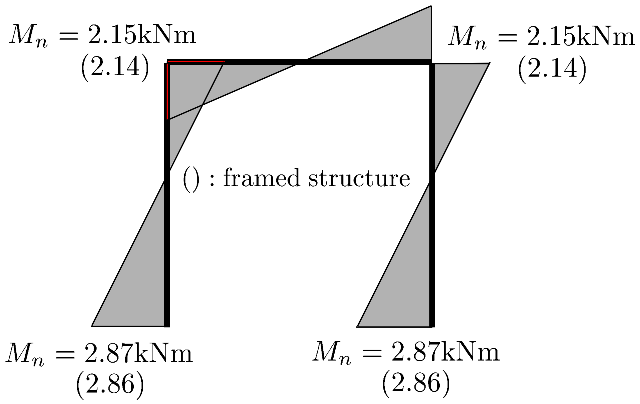

Fig.3.4.8 Bending moment for the elastic analysis

(2) Nonlinear Analysis

Figure 3.4.9 shows the results of the elastoplastic analysis for the problem shown in Fig. 3.4.6 The analysis uses the same conditions, such as the shape dimensions, loading conditions, and condition of constraints. Figure 3.4.9 shows the load–displacement curves; the vertical axis represents the dimensionless load, and the horizontal axis represents the horizontal displacement of the loading point. The blue dashed line represents the limit load in the plastic analysis of the framed structure. The numbers attached to the white circles and nodes of the portal frame in the figure indicate the order of occurrence of the plastic hinges.

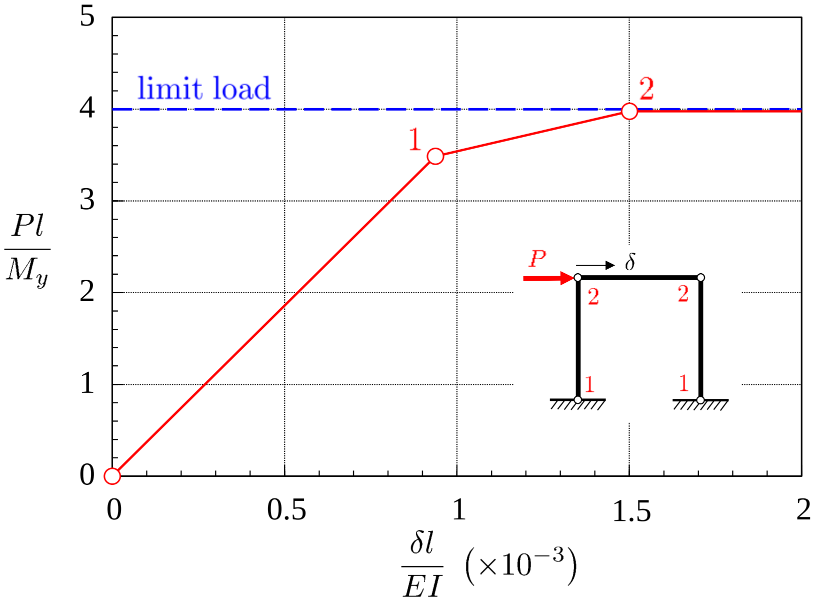

Fig.3.4.9 Load–displacement curve for the nonlinear analysis

Figure 3.4.10 shows the distribution of bending moments when the collapse mechanism is formed. The bending moment at the node of the plastic hinge was consistent with the full plastic moment.

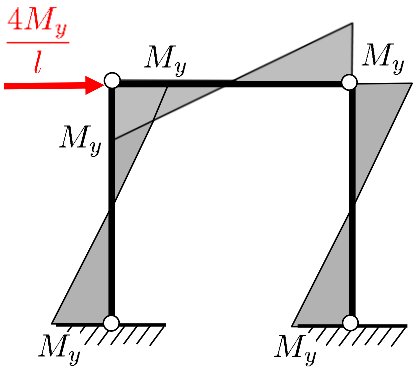

Fig.3.4.10 Bending moment in the collapse mechanism

3.4.3 *Two-hinge Arch*

Figure 3.4.11 shows the two-hinge arch analysis model. The analysis configuration is an arc with a radius of $R = 0.16$ m rotated $\pi/2$ from the position $\pi/4$ from the horizontal, and both the ends have hinge supports. The depth is $d = 0.1$ m, and the plate thickness is $t = 0.002$ m. The material has modulus E = 190 GPa, Poisson's ratio $\nu = 0$, and plastic moment $M_y = 2$ Nm/m. The number of element is 90, with 45 divisions on one side (in increments of 1°).

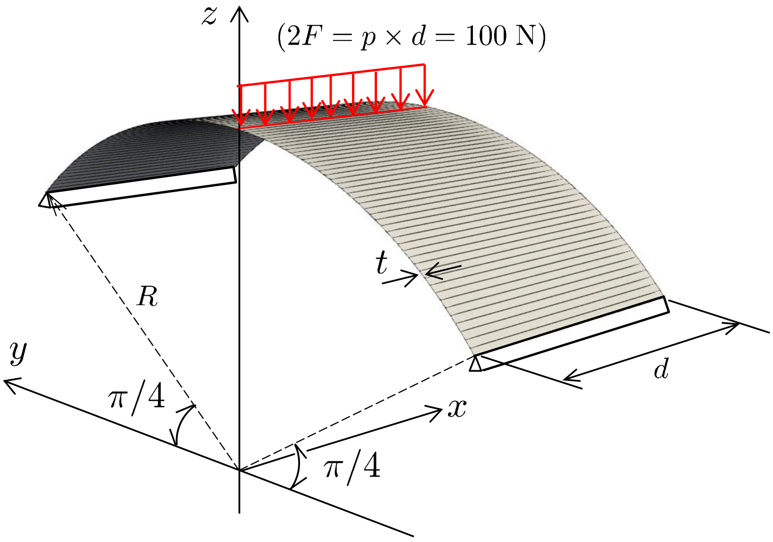

Fig.3.4.11 Numerical model for the two-hinge arch

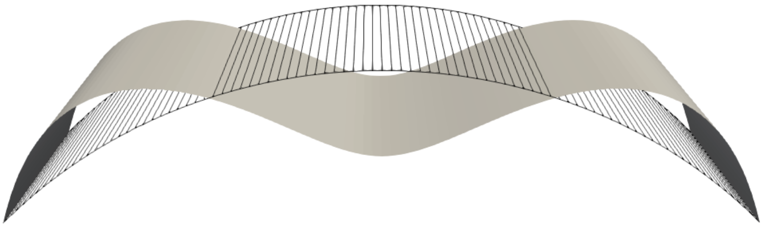

Fig.3.4.12 Displacement mode (Scale: Displacement*400)

Figure 3.4.12 shows the displacement modes. The wireframe shows the original shape before deformation, and the gray-filled shape is the shape after deformation. The displacement scale has been multiplied by 400. A total of three large curvatures appear, one in the center and two on the sides.

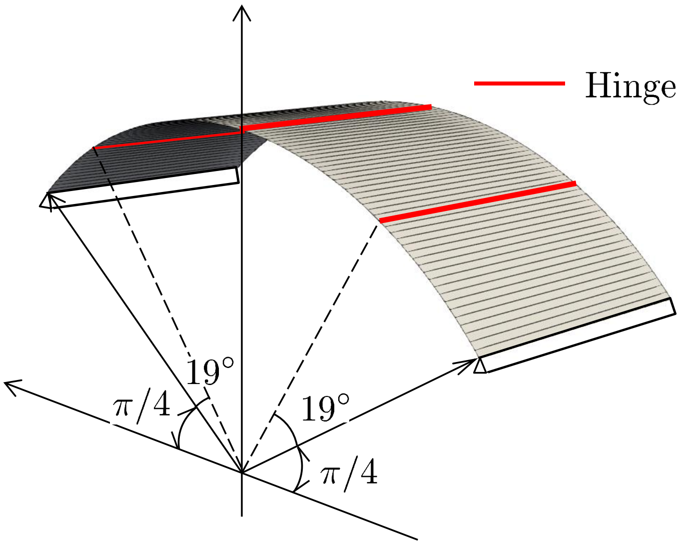

Fig.3.4.13 Hinge lines

The hinge line is generated at the point where a large curvature occurs. In this study, the influence of the axial force is ignored, and the hinge is evaluated only by the bending moment. However, the hinge occurs at a fixed position regardless of the axial force [35]. In a previous study, the hinge occurred at a position of $18°36.6'$ from the supporting point [35]; however, it occurred at $19°$ in this analysis. Because the element division is in increments of $1°$, the accuracy is not higher than this, but the result is roughly consistent with the theoretical consideration.

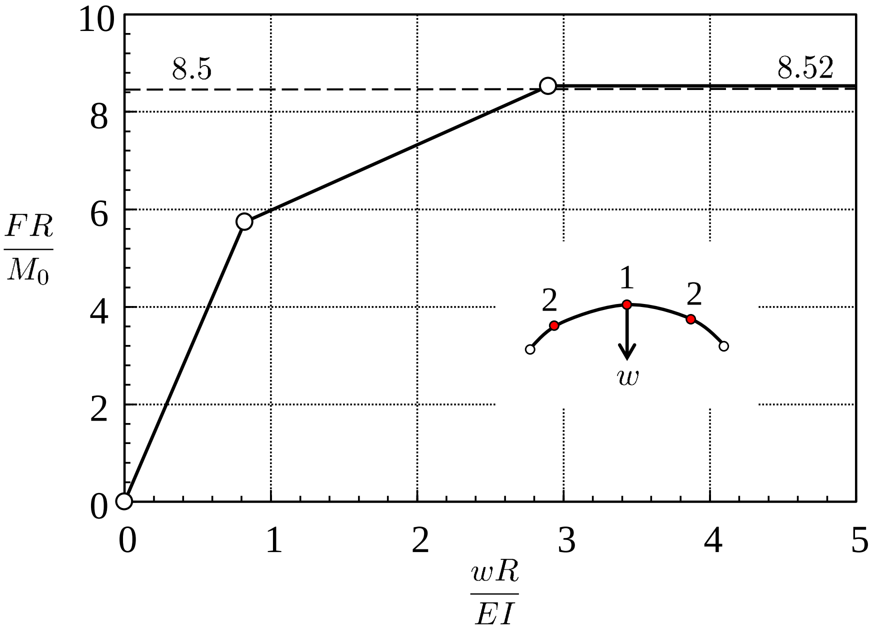

Fig.3.4.14 Load–displacement curve

Figure 3.4.14 shows the load–displacement curve, 1 and 2 in the figure represent the order of occurrence of hinges. The horizontal axis represents the deflection at the center of the arc, and the vertical axis represents the non-dimensional load. The non-dimensional collapse loads in the plastic analysis and in the present method were 8.5 and 8.52 respectively, indicating an error of less than 1%.

4 LARGE DISPLACEMENT ANALYSIS OF FLAT SHELL STRUCTURE

4.1 Deformation of Limit Rotation Angle

4.1.1 *Euler Angle*

Figure 4.1.1 shows the Euler angles $(\theta\ ,\ \phi\ ,\ \psi)$ that represent the relationship between the Cartesian coordinate systems before and after the rigid body rotation in three-dimensional Euclidean space.

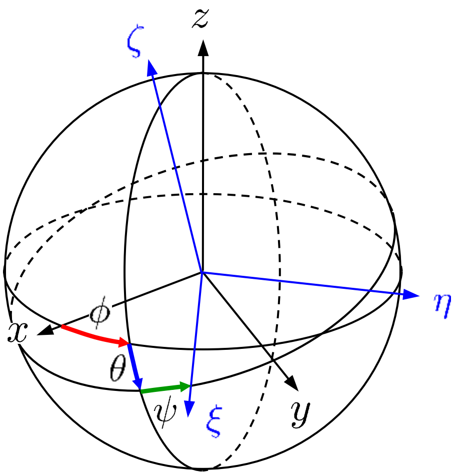

Fig.4.1.1 Euler angle

Using this, the exact three-dimensional rigid body displacement function $(u\ ,\ v\ ,\ w)$ is expressed as follows:

$$\left.\begin{aligned} u &= u_0 + l_\xi x + l_\eta y + l_\zeta z - x \\ v &= v_0 + m_\xi x + m_\eta y + m_\zeta z - y \\ w &= w_0 + n_\xi x + n_\eta y + n_\zeta z - z \end{aligned}\right\} \tag{4.1.1}$$

Here, $(u_0\ ,\ v_0\ ,\ w_0)$ are the translational displacement components of the origin. And $(l\ ,\ m\ ,\ n)$ are the following direction cosines:

$$\begin{aligned}
l_\xi &= \cos\psi\cos\theta\cos\phi - \sin\psi\sin\phi \\
l_\eta &= -\sin\psi\cos\theta\cos\phi + \cos\psi\sin\phi \\
l_\zeta &= \sin\theta\cos\phi
\end{aligned}$$

$$\begin{aligned}
m_\xi &= \cos\psi\cos\theta\sin\phi + \sin\psi\cos\phi \\
m_\eta &= -\sin\psi\cos\theta\sin\phi + \cos\psi\cos\phi \\
m_\zeta &= \sin\theta\sin\phi
\end{aligned}$$

$$\begin{aligned}
n_\xi &= -\cos\psi\sin\theta \\
n_\eta &= \sin\psi\sin\theta \\
n_\zeta &= \cos\theta
\end{aligned}$$

4.1.2 *Limit Rotation Angle*

The exact rigid body displacement function for in-plane deformation in a flat shell can be treated as a two-dimensional problem with respect to the local coordinate system (x, y) shown in Figure 4.1.2.

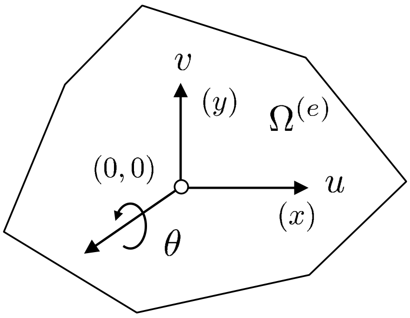

Fig.4.1.2 Local coordinate system and in-plane displacement field of flat shell

Now, Equation (4.1.1) is expressed as follows:

$$\left.\begin{aligned}
u &= u_0 + x\cos\theta - y\sin\theta - x \\
v &= v_0 + x\sin\theta + y\cos\theta - y
\end{aligned}\right\} \qquad (4.1.2)$$

When considering finite rotation, an incremental calculation that expands Equation (4.1.2) by Taylor series and considers up to the quadratic term is often used.

However, in the discrete element method and rigid body spring model, minute rotation is assumed, and the following relationship is assumed:

$$\sin\theta \approx \theta \tag{4.1.3a}$$

$$(1-\cos\theta) \approx 0 \tag{4.1.3b}$$

Now, Equation (4.1.2) is approximated as follows:

$$\left.\begin{aligned} u &= u_0 - y\theta \\ v &= v_0 + x\theta \end{aligned}\right\} \tag{4.1.4}$$

In the large displacement problem, a large rigid body rotation occurs where Equation (4.1.3) is not satisfied. The rigid body rotation angle that satisfies Equation (4.1.3) is defined as the limit rotation angle. Subsequently, an incremental method is proposed that computes sequentially so as not to exceed the ***limit rotation angle***. The details of this algorithm are described in Section 4.3.

4.2 Coordinate Transformation of Stress

4.2.1 *Rotation of Element Stress*

The method proposed in this paper analyzes the small deformation problem sequentially while updating the node coordinates for the large displacement problem. Figure 4.2.1 shows the cantilever before and after deformation.

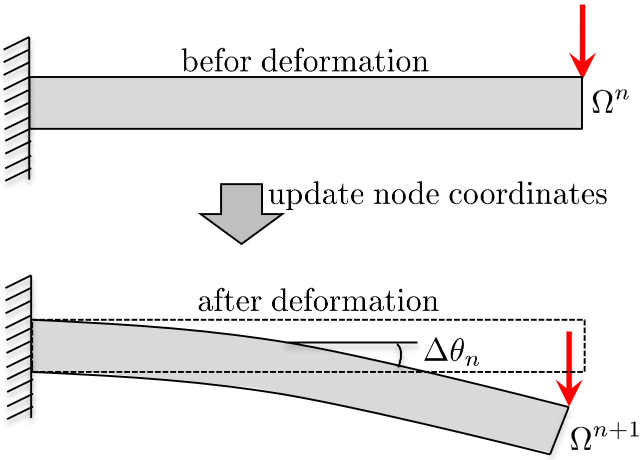

Fig.4.2.1 Cantilever deformation with updated node coordinates

The total displacement is obtained by accumulating the updated values of the nodal coordinates. However, for elemental stress, coordinate transformation is required owing to the changes in the local coordinate system; Figure 4.2.2 shows this relationship.

The left-hand side of the figure shows the stress state before deformation. By updating the nodal coordinates after deformation, this stress becomes like the stress shown in red on the right-hand side of the figure. If the stress is expressed in the local coordinate system for each element, the result of the incremental analysis by the new coordinate system can be simply added to the previous stress. However, this method cannot properly evaluate the stress distribution of the analysis domain because the definition of stress for each element is different. Therefore, we propose a method of converting stress into a global coordinate system and evaluating the stress in a unified coordinate system.

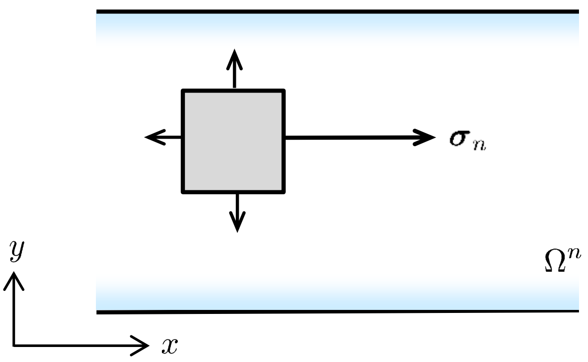

(a) Before deformation

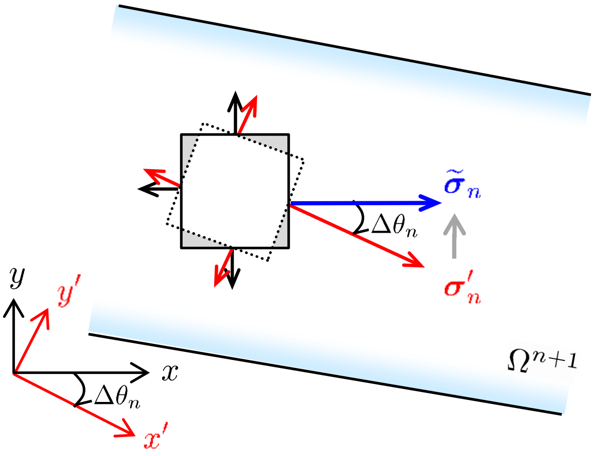

(b) After deformation

Fig.4.2.2 Coordinate transformation of stress in large displacement analysis

As shown in Figure 4.2.2, let $\boldsymbol{\sigma}'_n$ be the stress in the deformed coordinate system $(x' - y')$, which is rotated by $\Delta\theta_n$ from the global coordinate system $(x - y)$, the following relationship exists between the two coordinate systems:

$$\boldsymbol{x} = \boldsymbol{R}\boldsymbol{x}', \tag{4.2.1}$$

where

$$\boldsymbol{R} = \begin{bmatrix} \cos\Delta\theta_n & \sin\Delta\theta_n \\ -\sin\Delta\theta_n & \cos\Delta\theta_n \end{bmatrix}. \tag{4.2.2}$$

Therefore, the stress $\boldsymbol{\sigma}'_n$ before deformation is converted to the stress $\tilde{\boldsymbol{\sigma}}_n$ after deformation as follows:

$$\tilde{\boldsymbol{\sigma}}_n = {}^t\boldsymbol{R}_n \boldsymbol{\sigma}_n \boldsymbol{R}_n \tag{4.2.3}$$

Using this stress, the stress in the global coordinate system can be obtained by the following incremental computation:

$$\boldsymbol{\sigma}^{n+1} = \tilde{\boldsymbol{\sigma}}^n + \Delta\boldsymbol{\sigma}^{n+1} \tag{4.2.4}$$

4.2.2 *Rotation of Surface Force*

As shown in Figure 4.2.3, the surface force is expressed by the local coordinate system of the element boundary surface, thus, coordinate transformation is not needed.

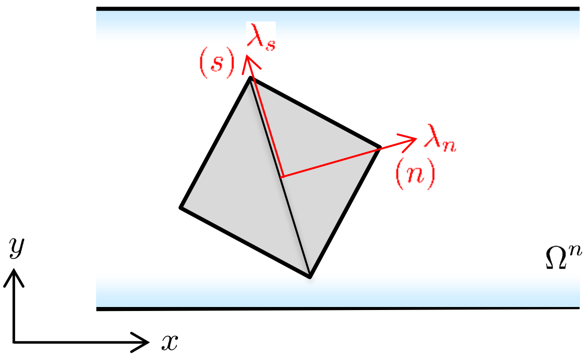

(a) Before deformation

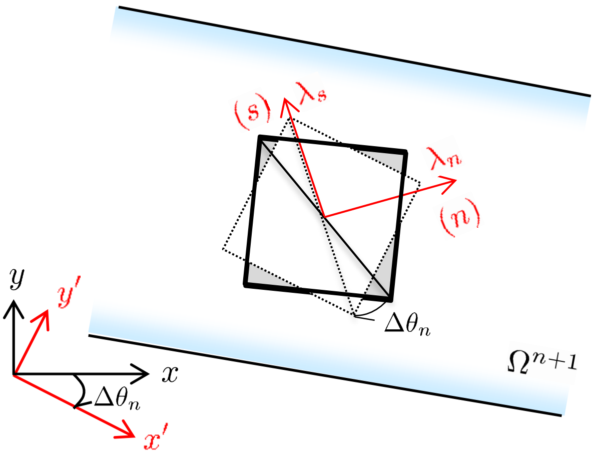

(b) After deformation

Fig.4.2.3 Rotation of the surface force in large displacement analysis

This implies that the coordinate transformation is not required in incremental computation, as shown below.

$$\boldsymbol{\lambda}^{n+1} = \boldsymbol{\lambda}^{n} + \Delta\boldsymbol{\lambda}^{n+1} \tag{4.2.5}$$

4.3 Large Displacement Analysis Algorithm via Step-by-Step Method

4.3.1 *Step-by-Step Method*

Similar to small deformation analysis, large displacement analysis is difficult to handle as a linear analysis method because the stiffness matrix changes with the deformation of the object. In this paper, as shown in Figure 4.3.1, the step-by-step method is used to analyze the large displacement problem by repeating the small-displacement analysis.

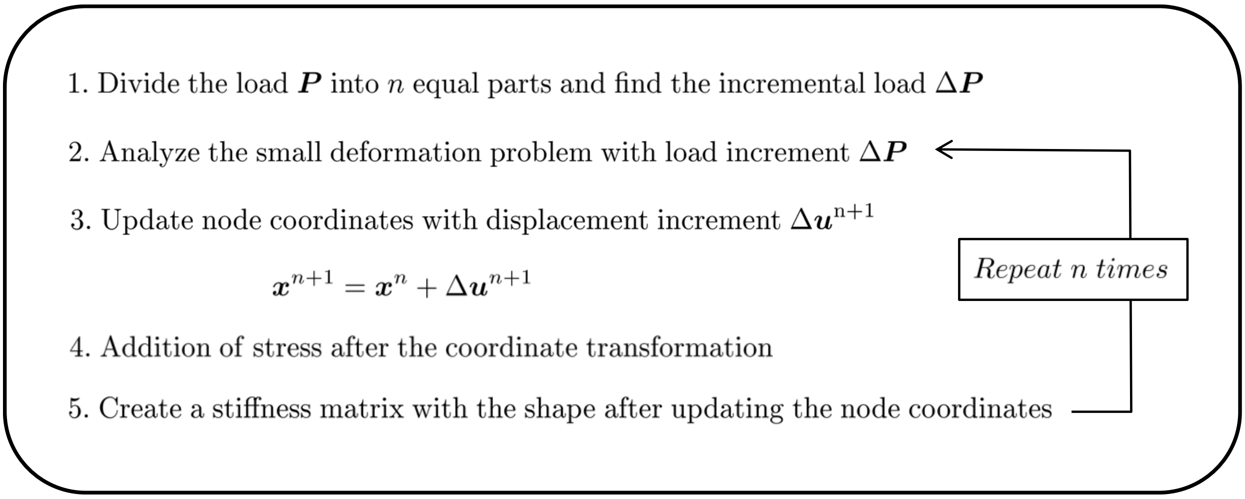

1. Divide the load $\boldsymbol{P}$ into n equal parts and find the incremental load $\Delta\boldsymbol{P}$
2. Analyze the small deformation problem with load increment $\Delta\boldsymbol{P}$
3. Update node coordinates with displacement increment $\Delta\boldsymbol{u}^{n+1}$

$$\boldsymbol{x}^{n+1} = \boldsymbol{x}^{n} + \Delta\boldsymbol{u}^{n+1}$$

4. Addition of stress after the coordinate transformation
5. Create a stiffness matrix with the shape after updating the node coordinates

Fig.4.3.1 Large displacement analysis method by a step-by-step method

As shown in the figure, the load acting on the object is divided into several incremental loads, and the small deformation problem is analyzed for each incremental load. The obtained displacement $\Delta\boldsymbol{u}^{n+1}$ is added to the coordinate value $\boldsymbol{x}^{n}$ before deformation, coordinate value is updated, and shape after deformation is created as $\boldsymbol{x}^{n+1}$. The previous stress is added to the incremental stress to obtain the total stress, a rigidity matrix is created with the new node coordinate values, and the linear analysis is repeated.

In this case, the error may accumulate depending on the setting of the incremental load. In this study, a method is proposed to determine the load increment so as not to exceed the limit rotation angle defined in Section 4.1.2.

4.3.2 *Analysis Flow*

The analysis flowchart in the present method is depicted in Figure 4.3.2. As shown in the figure, the solution is obtained by linear analysis of the small deformation problem, and the load increment rate for not exceeding the limit rotation angle is obtained in (*1). Because it is a linear analysis, the current increment value is obtained by multiplying this load increment rate by the obtained solution. By adding this to the previous values, the current total displacement, stress, and surface force are obtained. However, for stress, the coordinate transformation described in Section 4.1.2 in (*2) is required. Subsequently, the total load increment rate used up to now is calculated by (*3). If this value is less than 1, the coordinates are updated, and the linear analysis is repeated with the remaining load.

However, the limit rotation angle affects the solution in this case. In general, it is possible to prevent the accumulation of errors by satisfying Equation (4.1.3); that is, setting it to 3° or less.

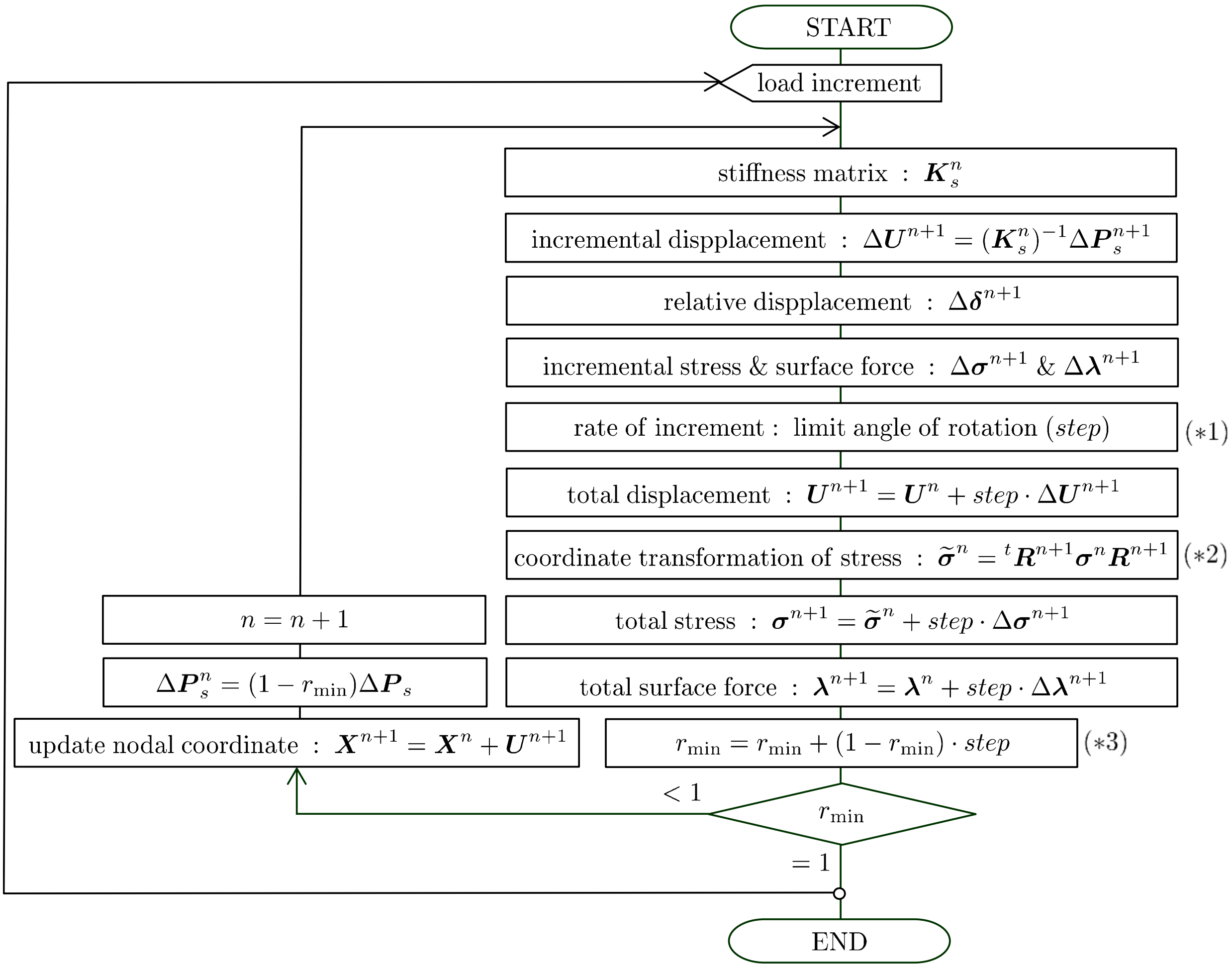

Fig.4.3.2 Analysis flowchart of large displacement problem by the step-by-step method

4.4 Numerical Examples

4.4.1 *Cantilever Beam*

In this section, the accuracy of the solution of the large displacement analysis by the step-by-step method proposed in Section 4.1 was verified for the elastic problem of the flat shell. Figure 4.4.1 shows the model and mesh division used in the analysis. As shown in the figure, the numerical model is a flat plate with one end fixed. The dimensions and material constants are shown in the figure. The mesh is divided as shown in the lower part of the figure, but the number of divisions is analyzed assuming various cases.

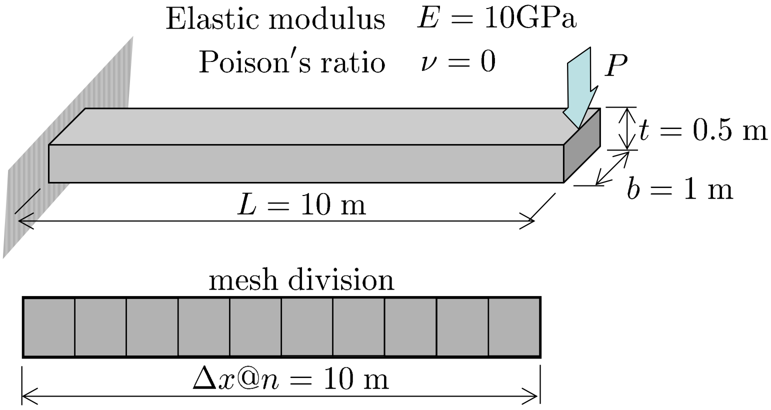

Fig.4.4.1 Numerical model and material constants for elastic cantilever beam

In Figure 4.4.2, the horizontal axis is the limit rotation angle, and the vertical axis is the value obtained by dividing the deflection at the free end by the solution of the beam theory. The red circle represents the deflection at the free end, and the blue triangle represents the horizontal displacement. A convergent solution is obtained when the limit rotation angle is set to 0.05 radians or less. This angle expressed in degrees is roughly 2.86°. Sin 2.86° is equal to roughly 0.0499, which is similar to the limit rotation angle.

Figure 4.4.3 shows the dimensionless deflection of the free end of the flat plate on the horizontal axis and the dimensionless load on the vertical axis. Horizontal displacement does not occur in infinitesimal deformation problems. The solid red line shows the large displacement solution by the beam theory, and the solid black line shows the solution by the infinitesimal deformation theory. The blue circle is the solution by this method, and the results are nearly the same.

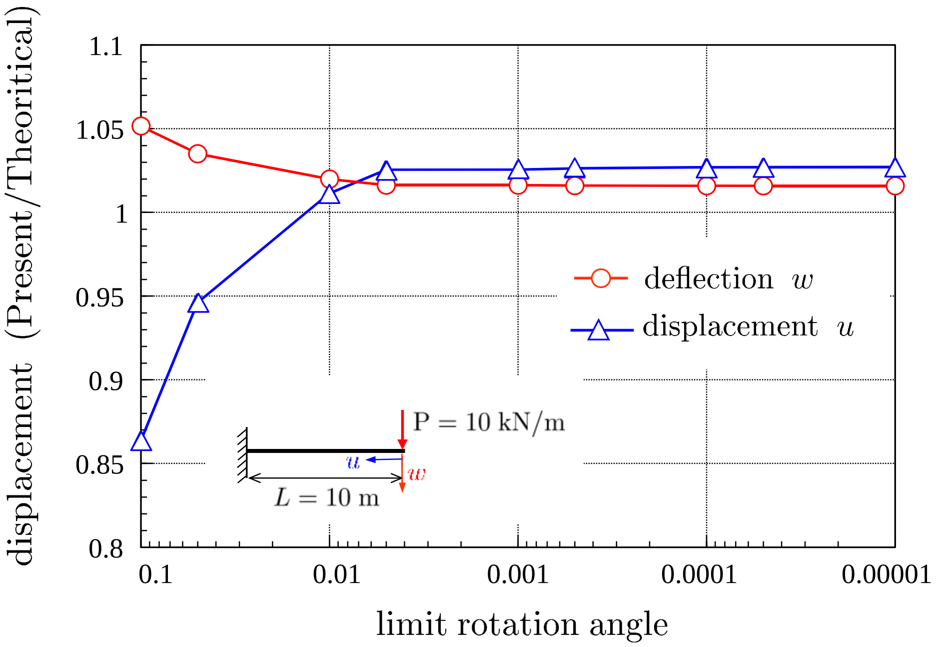

Fig.4.4.2 Accuracy of the displacement u and w for limit rotation angle

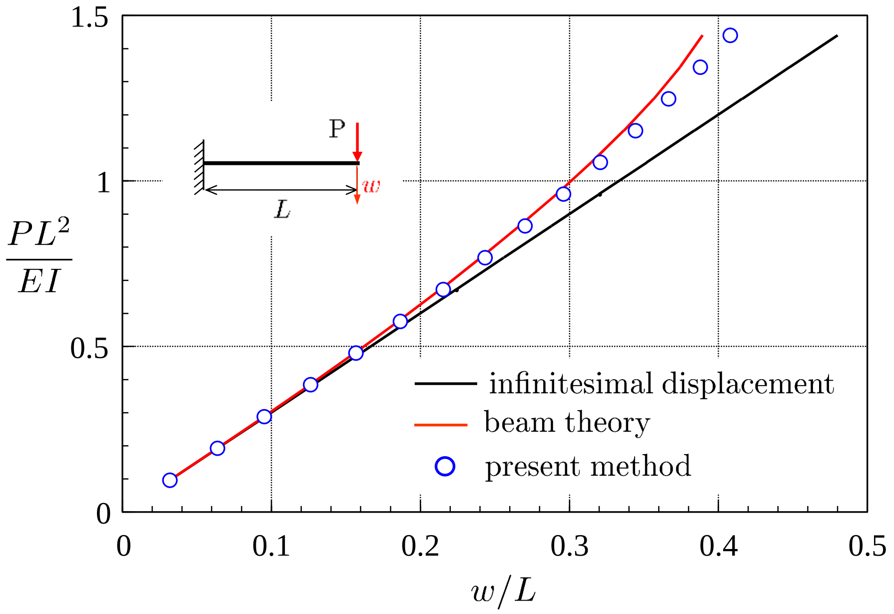

Fig.4.4.3 Relationship between load and large deflection

In Figure 4.4.4, the horizontal axis represents the dimensionless horizontal displacement value, and the vertical axis represents the dimensionless load. Horizontal displacement does not occur in infinitesimal deformation problems. The solid red line shows the large displacement solution by the beam theory. The blue circle is the solution by this method, and the results are nearly the same.

Figure 4.4.5 shows the displacement mode. The figure shows an example of 20 divisions, and the deflection and horizontal displacement are shown on a real scale.

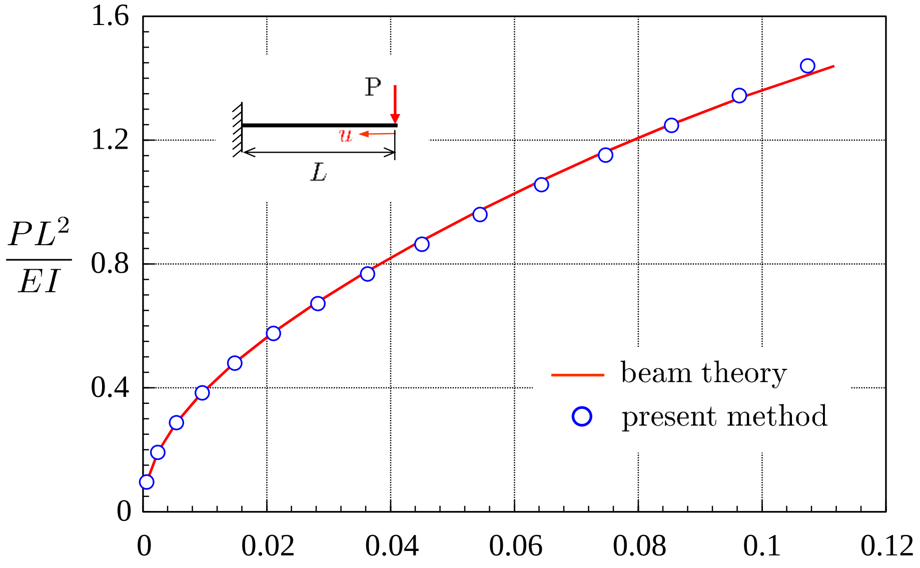

Fig.4.4.4 Relationship between the load and lateral displacement

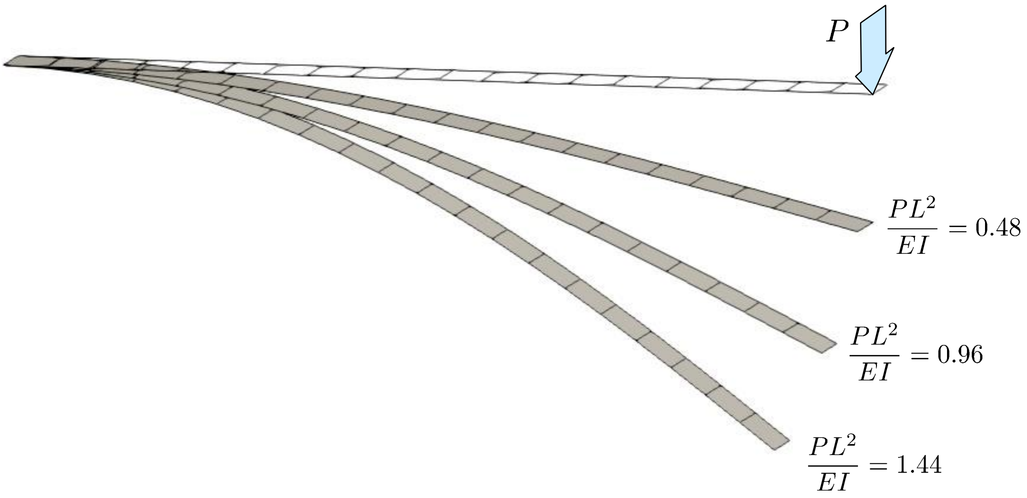

Fig.4.4.5 Displacement mode for each load

4.4.2 *Flat Shell Fixed at Both Ends*

Figure 4.4.6 shows an example of elastic large displacement analysis of a beam with fixed ends. Figure 4.4.6(a) shows the shape and dimensions. The load was applied at the center of the flat plate shell as shown in the figure; the load values are set for four cases of $P = 0.25, 0.5, 0.75$, and 1.0 N. The elastic modulus is E = 206 GPa and Poisson ratio ν = 0. The number of elements is 100 as shown in Figure (b). The limit rotation angle is set to 0.0001 rad.

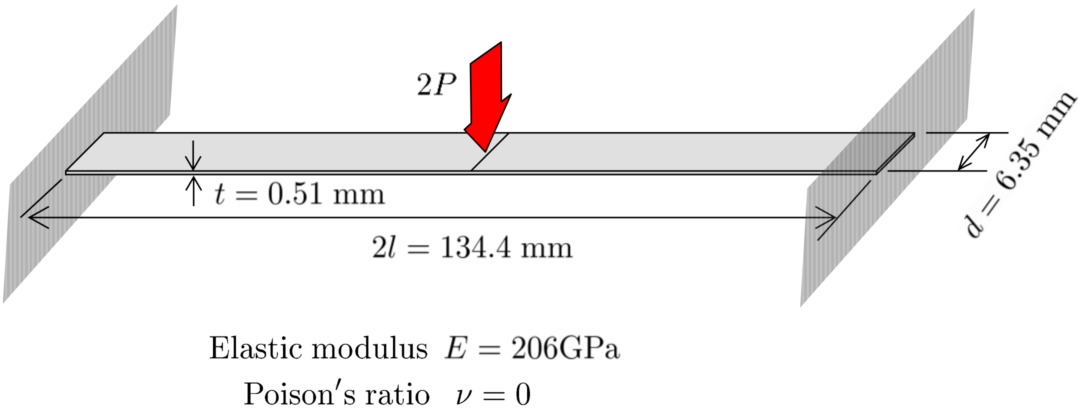

(a) model and material properties

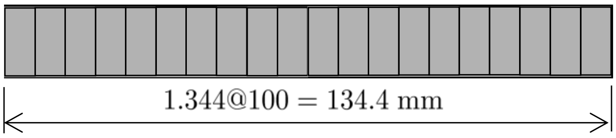

(b) mesh division

Fig.4.4.6 Numerical model for the flat shell fixed at both ends

Figure 4.4.7 shows the relationship between load and deflection. The deflection is the central value of the beam, and the load is the applied load. The dashed-dotted line represents the theoretical solution due to small deformation. because it is a linear solution, the deflection according to the load state is proportional. The solid line represents the theoretical large displacement solution. The rate of increase in deflection decreases as the load value increases. The circles represent the deflection of large displacement analysis by this method. The solution obtained by this method is close to the theoretical large displacement solution.

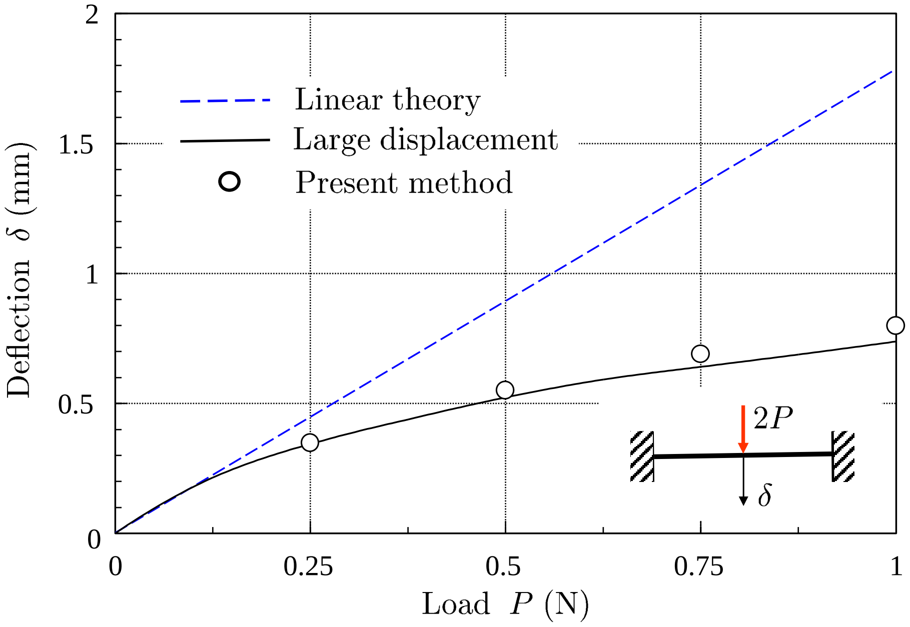

Fig.4.4.7 Deflection for each load

5 LARGE DISPLACEMENT ANALYSIS WITH MATERIAL NONLINEARITY

5.1 Load Increment Method using Limit Rotation Angle

As described in Section 4.1, the analysis method for the large displacement problem proposed in this study finds a solution by repeating the small displacement analysis. Each iterative analysis step has the same algorithm as the linear analysis in the small deformation problem. Also, in the case of material nonlinear problems, the algorithm of material nonlinear analysis developed in Chapter 3 can be applied. However, the method proposed in this paper uses the load increment rate due to the limit rotation angle. Therefore, when determining the load increment rate, the load increment rates for both the material nonlinearity and limit rotation angle are obtained, and the smaller value is used for the load increment rate. Hence, when the load increment rate is determined by the limit rotation angle, the elastic state is maintained and fracture phenomenon does not occur in the corresponding load step.

The outline of the algorithm per load step is as follows:

(1) Classify elements and element boundaries into yield and elastic states. For the yielded elements and element boundaries, the total coefficient matrix is constructed using the coefficient matrix after plasticization.

(2) For the given load increment, solve the coefficient matrix created in (1), and compute the incremental surface force.

(3) From the obtained displacement increment, find the load increment rate so that the limit rotation angle is not exceeded. Also, from the incremental stress or surface force, the load increment rate required for all elements or element boundaries to yield is computed. The smallest of these load increment rates is the current load increment rate.

(4) The stress and surface force at this stage are obtained by multiplying the incremental value obtained in step (3) by the load increment rate and adding it to the previous value. Here, the stress or surface force that reaches the yield strength then conforms to the plastic flow rules.

(5) Repeat steps (1)–(4) until the incremental load reaches the working load.

5.2 Flow Diagram of Material Nonlinear Large Displacement Analysis

Figure 5.2.1 shows the analysis flowchart of the large displacement problem with material nonlinearity used in this study. As shown in the figure, the solution is first obtained by linear analysis of the small deformation problem.

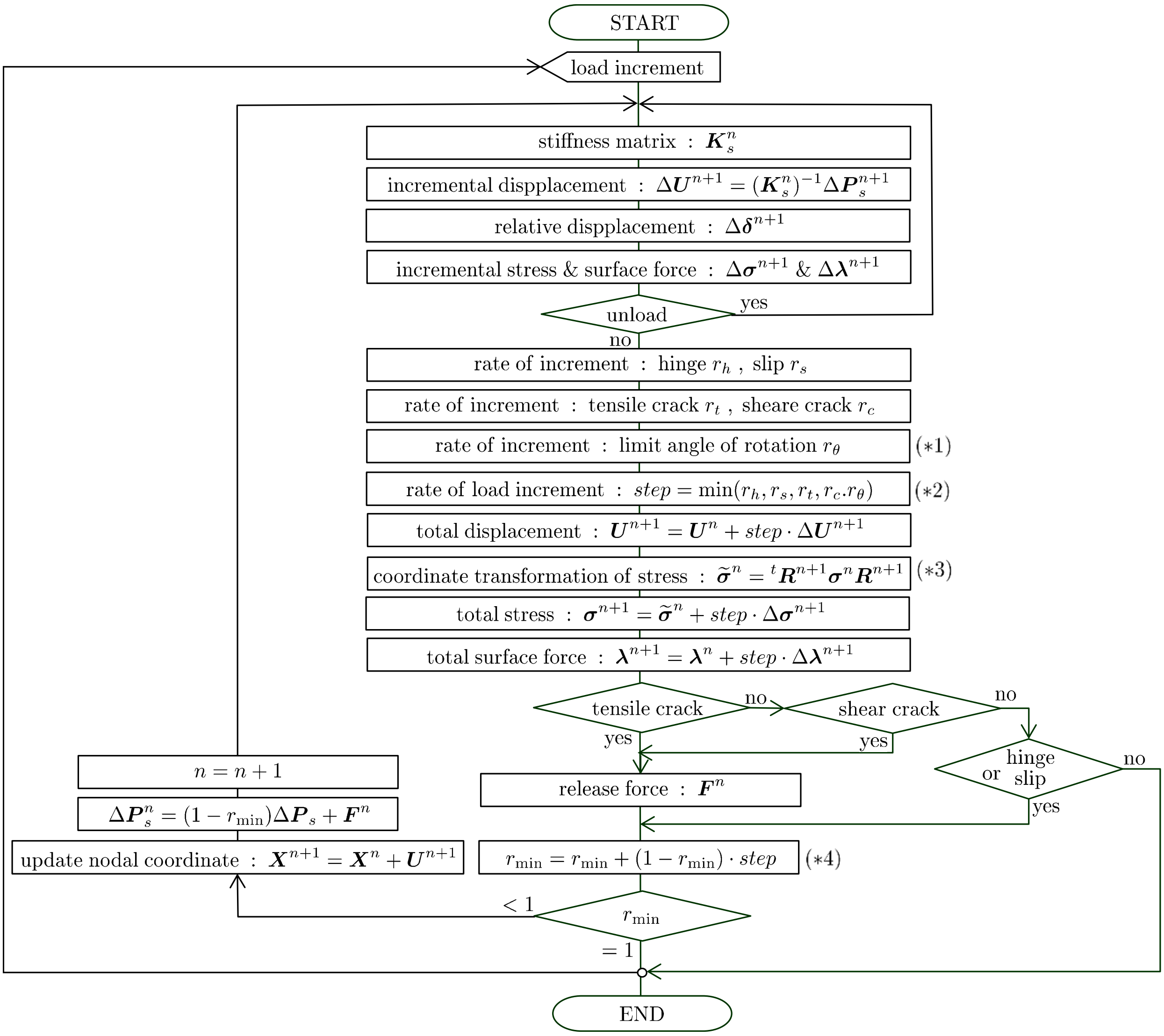

Fig.5.2.1 Analysis flowchart of the large displacement problem with material nonlinearity

Next, the load increment rate for the material nonlinear problem is obtained, and the load increment rate due to the limit rotation angle for the large deformation problem is obtained in (*1). Subsequently, the minimum load increment rate is calculated by (*2). For stress, the coordinate transformation described in Section 4.2.2 is applied in (*3). Finally, the total load increment rate used up to now is computed by (*4); if this value is less than 1, the coordinates are updated, and the linear analysis is repeated with the remaining load.

5.3 Numerical Examples

In this section, the accuracy of the solution of the large displacement analysis with material nonlinearity of the flat plate shell is verified by the step-by-step method proposed in Section 4.2.

5.3.1 *Flat plate shell fixed at one end*

Figure 5.3.1 shows the model and mesh division used in the analysis. As shown in the figure, the numerical model is a flat shell with one end fixed, and the dimensions are presented. In the nonlinear analysis, it was assumed that only the plastic hinge was generated and the total plastic moment was set. The material constants used in the analysis are shown in the figure. The mesh was divided into 20 rectangular elements as shown in the lower part of the figure.

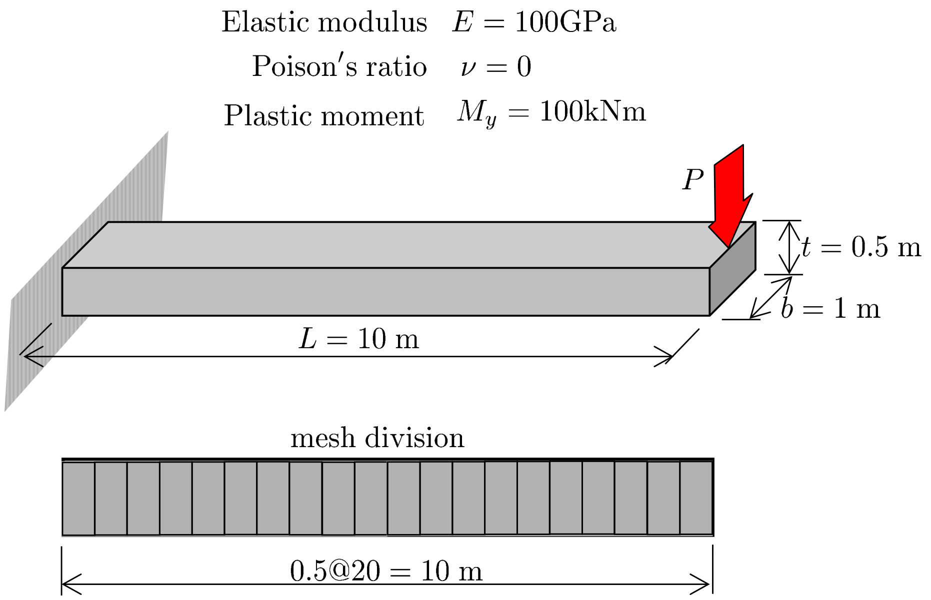

Fig.5.3.1 Numerical model and material constants for the flat shell fixed at one end

Figure 5.3.2 shows the dimensionless deflection of the free end on the horizontal axis and dimensionless load on the vertical axis. The solid red line shows the result of the large displacement analysis proposed in this paper, and the solid black line shows the result of infinitesimal deformation by the beam theory. The blue dashed line indicates the limit load in beam theory. The collapse load due to infinitesimal deformation is consistent with the solution of limit analysis. Whereas, the collapse load of the large displacement solution is slightly higher than that.

Figure 5.3.3 shows the displacement mode under a collapse load.

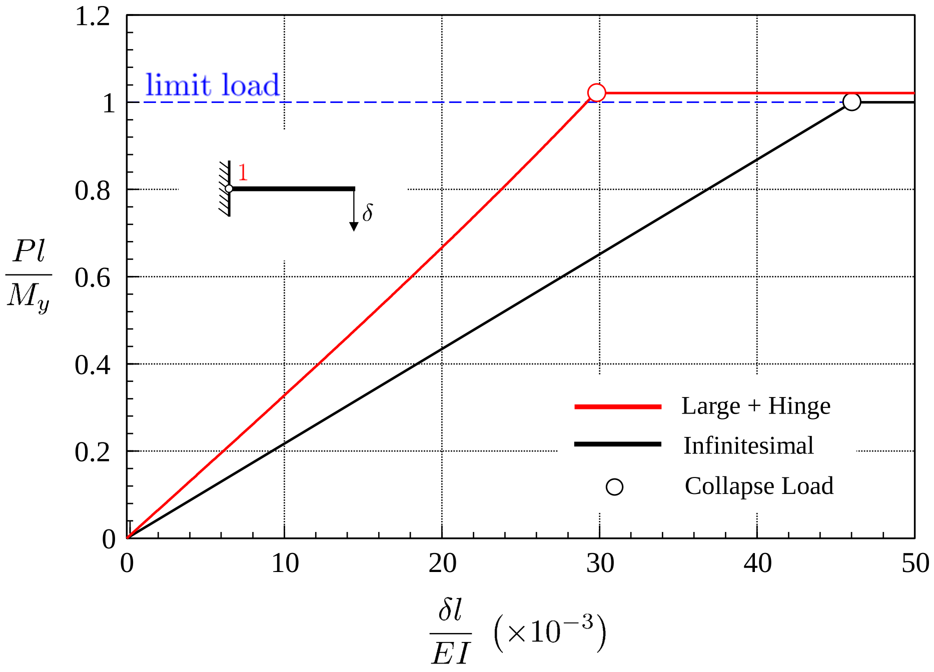

Fig.5.3.2 Load–deflection curve for the flat shell fixed at one end

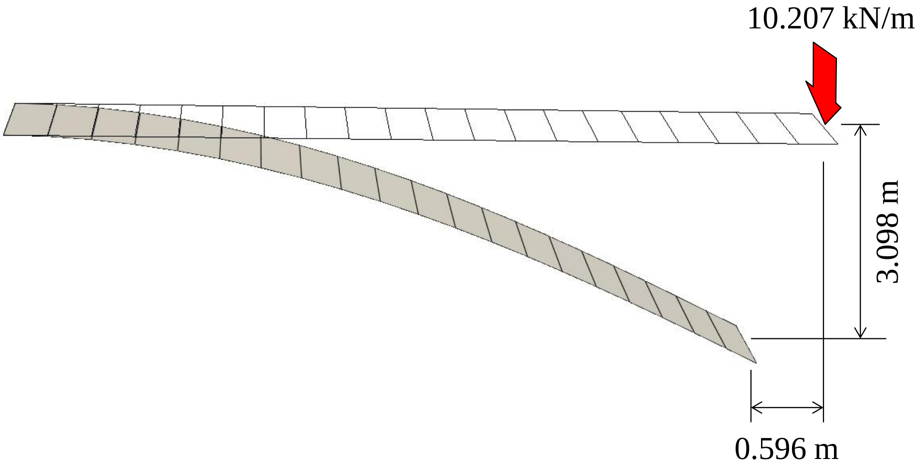

Fig.5.3.3 Displacement mode at the collapse load for the flat shell fixed at one end

5.3.2 *Flat plate shell fixed at both ends*

Figure 5.3.4 shows the model and mesh division used in the analysis. As shown in the figure, the numerical model is a flat shell with both ends fixed; the dimensions are presented in the figure. In the nonlinear analysis, it was assumed that only the plastic hinge was generated and the total plastic moment was set. The material constants used in the analysis are shown in the figure. The mesh was divided into 20 rectangular elements as shown in the lower part of the figure.

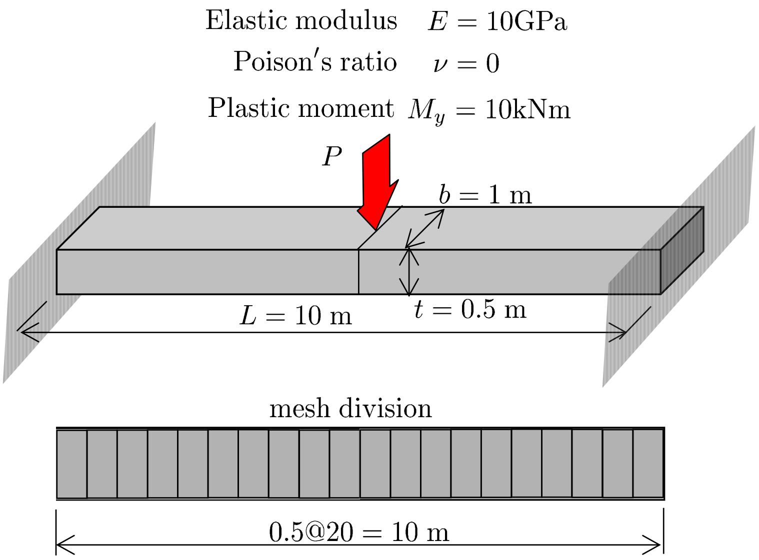

Fig.5.3.4 Numerical model and material constants for flat shell fixed at both ends

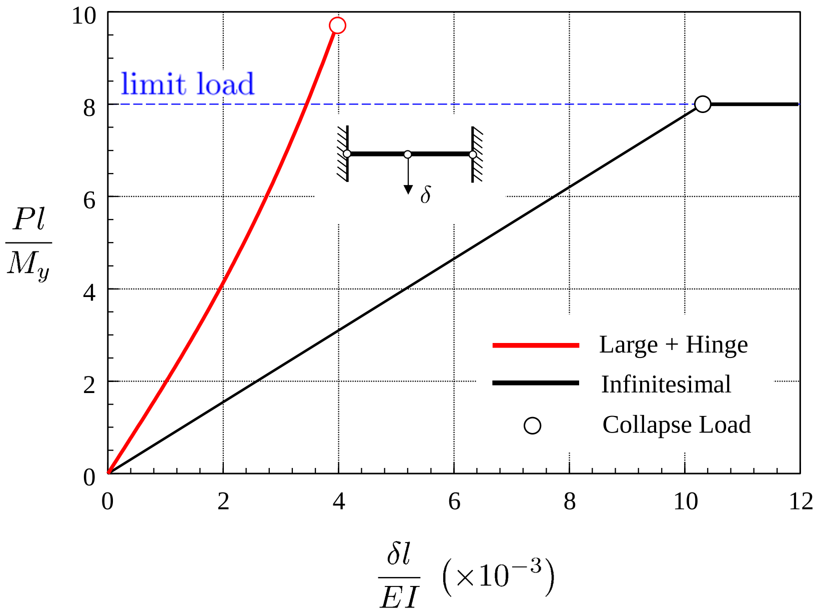

Fig.5.3.5 Load–deflection curve for the flat shell fixed at both ends

Figure 5.3.5 shows the dimensionless deflection at the center on the horizontal axis and dimensionless load on the vertical axis. The solid red line shows the result of the large displacement analysis proposed in this paper, and the solid black line shows the result of infinitesimal deformation by the beam theory. The blue dashed line indicates the limit load in beam theory. The collapse load owing to infinitesimal deformation is consistent with the solution of the limit analysis; whereas, the collapse load of the large displacement solution is slightly higher than that.

Figure 5.3.6 shows the displacement mode under a collapse load.

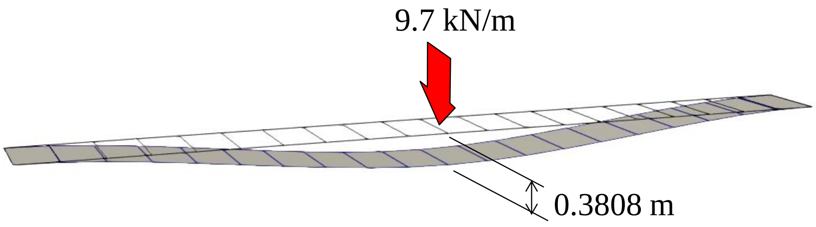

Fig.5.3.6 Displacement mode at collapse load for the flat shell fixed at both ends

5.3.3 *Portal frame*

Figure 5.3.7 shows the model and mesh division used in the analysis. As shown in the figure, the numerical model is a portal frame with both ends fixed. The dimensions are presented in the figure.

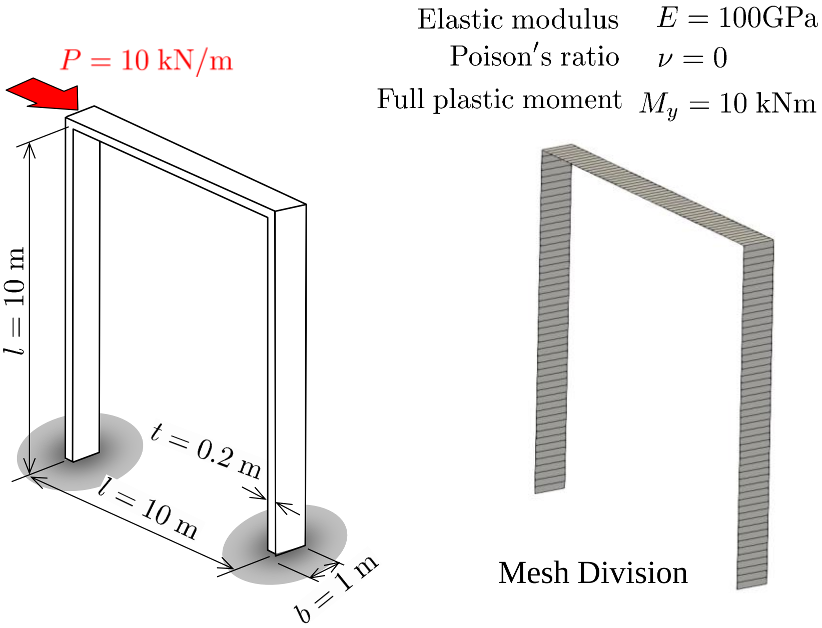

Fig.5.3.7 Numerical model and material constants for the portal frame fixed at both ends

In the nonlinear analysis, it was assumed that only the plastic hinge was generated and the total plastic moment was set. The material constants used in the analysis are shown in the figure. As shown on the right of the figure, the mesh was divided into 50 rectangular elements for columns and beam members, with 150 elements in total.

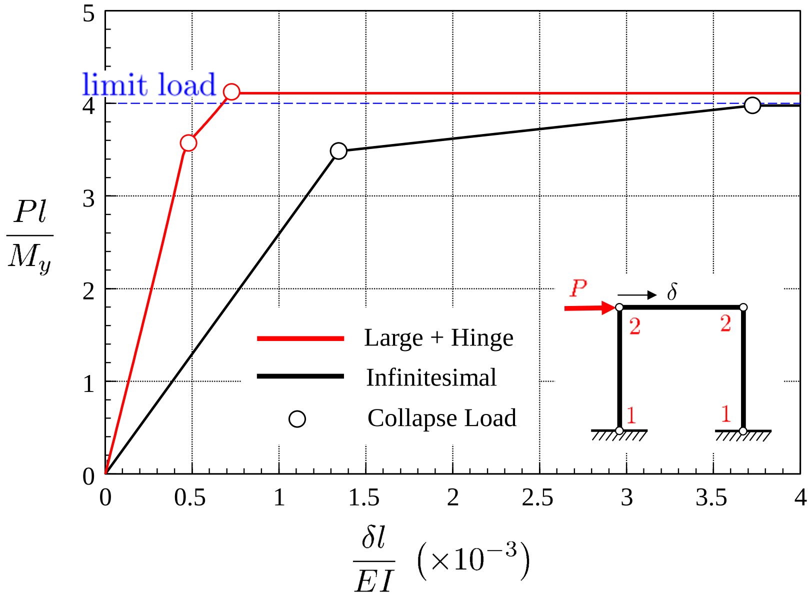

Fig.5.3.8 Load–deflection curve for the portal frame fixed at both ends

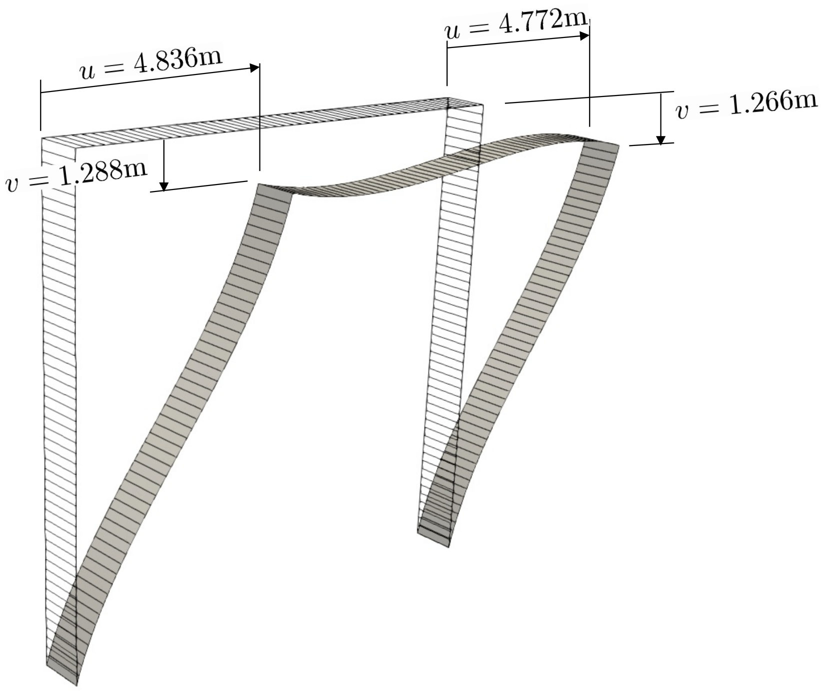

Fig.5.3.9 Displacement mode at collapse load for the portal frame fixed at both ends

Figure 5.3.8 shows the dimensionless displacement of the upper-right corner of the frame on the horizontal axis and dimensionless load on the vertical axis. The solid red line shows the result of the large displacement analysis proposed in this paper, and the solid black line shows the result of infinitesimal deformation by the beam theory. The blue dashed line indicates the limit load in beam theory. The collapse load due to infinitesimal deformation is consistent with the solution of limit analysis; whereas, the collapse load of the large displacement solution is slightly higher than that.

Figure 5.3.9 shows the displacement mode under a collapse load.

6 CONCLUSION

The primary goal of this study was to develop a shell model that uses the benefits of the HPM [19]-[21] and an algorithm for material nonlinear large displacement analysis using the shell model. The displacement field represented by the local coordinate system differs for each element. It was converted into the local coordinate system of one of the adjacent elements, and then to the coordinate system of the element boundary edge. The proposed method to calculate the relative displacement from the displacement of the boundary edge of the adjacent elements was obtained in this manner. HPM is based on the principle of the hybrid virtual work [22] and studies discontinuous elements in the finite element analysis method. In the HPM, the analysis domain is decomposed into subregions, and an independent displacement field is assumed for each element. This displacement field is composed of rigid body displacement, strain, and gradient. HPM is suitable for the analysis of large displacement problems where rigid body displacement is dominant. HPM can be used in an MOR method, which reduces the number of dimensions of the model. By using HPM for the MOR method, we can know the approximate fracture characteristics at the initial stage of structural design and provide information for safety evaluation.

In Chapter 2 we represented in-plane and out-of-plane problems, provided assumptions for modeling these problems, and showed that the superposition of these constitutes a flat shell problem. Subsequently, a governing equation of the elastic problem and hybrid virtual work equation were derived. Next, the HPM discretization equation for the flat shell problem was derived. The relationship between the coordinate systems was also described because our study was based on the local coordinate system. In the proposed model quadratic displacement field was used, and we described the relationship between the stress and the moment in the element. We also described the relationship between the relative displacement and surface force.

The accuracy of the solution for the proposed flat shell element is verified by numerical examples. We considered a cantilever with load acting from two directions [30]. Three cases were set according to the loading conditions: in-plane load, out-of-plane load, and both in-plane and out-of-plane loads. For the first case, there was a displacement at the right extremity in the simulation result by this method as well as in the analytical solution. The error in this method is less than 0.01%. For the second case, the deflection curve based on the beam theory approaches the solution based on the proposed model. Comparing the maximum deflection at the right extremity of the proposed model with the solution based on beam theory, the error was found to be less than 0.26%, confirming that high accuracy is obtained. Moreover, the deflection angles of both the proposed model and beam theory are nearly equal. For the third case, the result was obtained by combining the horizontal displacement of first case and deflection of second case. The results concurred with the concept of the proposed flat shell.

To examine the accuracy of the displacement solution of the proposed flat plate shell model, we considered a cantilever bent at an angle. In this example, if a penalty approximately in the range of 10^5–10^9 is used, a solution that is nearly consistent with the theoretical solution can be obtained. When it becomes 10^9 or more, the error tends to increase owing to the influence of the rounding error. Even with a small number of divisions, such as 5, a solution with little error is obtained for both horizontal and vertical displacements. Because this model uses a quadratic function as the displacement field for bending, an accurate solution can be obtained. Surface force on the boundary of the adjacent element and cross sectional force within the element obtained by proposed method are in good agreement with the beam theory solution.

Further for examination of the accuracy of the proposed method, we considered a semicircular curved beam [32] with a pin support at one end and roller support at the other end. The vertical displacement of the frame model with 20 elements was 5.768 mm, whereas the theoretical result of the vertical displacement was 5.759 mm. The solution by the proposed method has an error of roughly 0.4% even with a rough element division of nearly 20 elements.

Chapter 3 has described the discrete limit analysis of the flat shell problem. In the first step, the fracture conditions are described, and the relationship between the surface force and constitutive equation in HPM is summarized. As a numerical algorithm for material nonlinear analysis, the r-min method (Yamada's method) in the load increment method is used, concept of load increment in this material nonlinear analysis is described, and flowchart of this nonlinear analysis method is shown. Finally, the numerical calculation examples are presented.

As a first example of discrete limit analysis, a flat plate shell, with four sides of a rectangular plate simply supported, is analyzed. The mesh division divides the square area into crosses, and the number of elements is 1024. We considered an example where a concentrated load acts on the center of a square plate. The collapse load obtained by the present method had the same value as the theoretical collapse load. For this example, the experimental results are also given. The final mechanism of the present method includes the hinge line assumed in the plastic analysis. Therefore, it is considered that the collapse loads are the same. We also considered an example where a distributed load acts on the surface of a square plate. The collapse load obtained by the present method had the same value as the collapse load in the plastic analysis. When a concentrated load acts, the hinge line progresses from the center, whereas when a distributed load acts, it progresses from the four corners. Even when distributed loads are applied, the final mechanism of this method includes the hinge line assumed in the plastic analysis. Therefore, even in this case, the collapse load by plastic analysis and present method had the same value.

The next example is a portal frame under a horizontal load, where lower ends of both the columns are fixed. A quadrilateral element is used for mesh division, and the displacement field of the in-plane deformation is a linear function. In case of elastic analysis, the vertical displacements in both the analyses were nearly the same, although the difference between the horizontal displacements was 0.4%. For the bending moments in the elastic analysis, at all endpoints, there was a difference of 1 or less in the third digit, although the distributions were nearly the same.

In case of elastoplastic analysis, the problem uses the same conditions, such as the shape dimensions, loading conditions, and condition of constraints, and the bending moment at the node of the plastic hinge was consistent with the full plastic moment.

The last example to examine the accuracy of the proposed method is a two-hinge arch. In the numerical model the number of element is 90, with 45 divisions on one side (in increments of 1°). The hinge line is generated at the point where a large curvature occurs. In this study, the influence of the axial force is ignored, and the hinge is evaluated based on the bending moment. However, the hinge occurs at a fixed position regardless of the axial force [35]. The hinge occurred at a position of $18^\circ 36.6'$ from the supporting point in a previous study[35]; however, it occurred at 19° in this analysis. Because the element division is in increments of 1°, the accuracy is not higher, but the result is nearly consistent with the theoretical consideration. The non-dimensional collapse load in the plastic analysis was 8.5 and 8.52 in the present method, with an error of less than 1%.

Chapter 4 describes the large displacement analysis of the flat shell problem. In this study, the r-min method in the load increment method, described in Chapter 3, is applied as an algorithm for large displacement analysis. In order to control the load increment, a newly defined limit rotation angle is used.

For verification of accuracy, we considered an elastic problem of a cantilever beam. The numerical model is a flat plate with one end fixed. A convergent solution is obtained when the limit rotation angle is set to 0.05 or less. Expressed in degrees, it is approximately 2.86°. Sin 2.86° is approximately 0.0499, which is similar to that of the limit rotation angle. Large displacement solution by the beam theory and the solution by this method are nearly consistent.

The next example is an elastic large displacement analysis of a beam with fixed ends. The load was applied at the center of the flat plate shell. The number of elements is 100, and the limit rotation angle is set to 0.0001 rad. The results show that the solution obtained by this method is close to the theoretical large displacement solution.

Chapter 5 describes large displacement analysis with material nonlinearity. The numerical algorithm for nonlinear analysis uses the r-min method in the load increment method, described in Chapters 3 and 4. The rate of load increment is determined by simultaneously considering the rate of load increment with respect to the strength, described in Chapter 3, and rate of load increment owing to the limit rotation angle, described in Chapter 4.

In the nonlinear analysis, it was assumed that only the plastic hinge was generated, and only the total plastic moment was set. To verify the accuracy of the solution of the large displacement analysis with material nonlinearity, we considered a flat plate shell fixed at one end. The mesh was divided into 20 rectangular elements. Subsequently, we considered a flat plate shell fixed at both ends, and the final example was a portal frame with both ends fixed. For these 3 cases, the results show that the collapse load due to infinitesimal deformation is consistent with the solution of limit analysis. The collapse load of the large displacement solution is slightly higher than that from limit analysis.

REFERENCE

[1] Z-Q Qu, *Model Order Reduction Techniques with Applications in Finite Element Analysis*, Springer-Verlag, 2004.

[2] O.C. Zienkiewicz and R. L. Taylor, *The Finite Element Method,* Butterworth-Heinemann, 2000.

[3] TNO DIANA, DISNA User's Manual – Element Library, 2022.7. https://dianafea.com/manuals/d944/ElmLib/node227.html

[4] Nippon Sheet Glass Co., Ltd., About heat cracking, 2022.7. https://www.asahiglassplaza.net/gp-pro/knowledge/vol15.html

[5] S. Ahmad, B.M. Irons and O.C. Zienkiewicz, Analysis of thick and thin shell structures by curved finite elements. *Int. Journal for Numerical Methods in Engineering*, Vol.2, pp.419-451, 1970.

[6] D. Hamadi, A. Ayoub and O. Abdelhafid, A new flat shell finite element for the linear analysis of thin shell structures, *European Journal of Computational Mechanics*, Vol.24, No.6, pp.232-255, 2016.

[7] J. Burand and S.S. Angalekar, Non-linear finite element analysis of shells using parametric study, *International Journal of Engineering Science & Research Technology*, Vol.6, No.7, pp.116-121, 2017.

[8] D.M. Lamine, D.Hamadi, O. Temami, A. Ashraf and K. Abdelhak, Effect of boundary conditions and geometry on the failure of cylindrical shell structures. *Engineering Solid Mechanics*,Vol.8, pp.313-322, 2020.

[9] M.G. Rivera, J.N. Reddy and M. Amabili, A continuum eight-parameter shell finite element for large deformation analysis, *Mechanics of Advanced Materials and Structures*, Vol.27, No.7, pp.551-560, 2020.

[10] K.Y. Sze, X.H. Liu and S.H. Lo, Popular benchmark problems for geometric nonlinear analysis of shell, *Finite Elements in Analysis and Design*, Vol.40, No.11, pp.1551-1569, 2004.

[11] A.R. Silva and L.E.S. Dias, An interface element for numerical analysis of flat plate/shell elements with deformable connection, *Latin American Journal of Solid and Structures*, Vol.15, No.2, pp.1-16, 2018.

[12] J.A. Cottrell, T.J.R. Hughes and Y. Bazileves, Isogeometric Analysis, *John Wiley and Sons*, 2009.

[13] J. Kiendl, K.U. Bletzinger, J. Linhard and R. Wuchner, Isogeometric shell analysis with Kirchhoff-Love element, *Computer Methods in Applied Mechanics and Engineering*, Vol.198, No.49, pp.3902-3914, 2009.

[14] D. Schollhammer, B. Marussig and T.P. Fries, A consistent higher-order isogeometric shell formulation, *arXiv:2012.11975v1*, 1-51, 2020.

[15] A. Kefal and E. Oterkus, Isogeometric iFEM analysis of thin shell structures, *Sensors*, Vol.20, pp.1-24, 2020.

[16] D. Ngo and A. C. Scordelis, Finite element analysis of reinforced concrete beams, *J. Am. Concrete Inst.*, Vol.64, No.3, pp.152-163, 1967.

[17] R. E. Goodman, R. L. Taylor and T. L. Brekke, A model for the mechanics of jointed rock, *J. Soil Mech. and Found. Divi. Proc. ASCE*, Vol.94, SM3, pp.637-659, 1968.

[18] Y. Belytschko and T. Black, Elastic crack growth in finite elements with minimal remeshing, *Int. J. Numer. Meth. Engrg*, No.45, pp.602-620, 1999.

[19] N. Takeuchi, M. Kusabuka, H. Takeda, K. Sato and T. Kawai, The discrete limit analysis by using the hybrid model with the penalty, *Journal of Structural Engineering*, Vol.46A, pp.261-270, 2000.

[20] N. Takeuchi, H. Ohki, A. Kambayashi and M. Kusabuka, Material non-linear analysis by using discrete model applied penalty method in hybrid displacement model, *Transactions of JSCES*, Paper No.20010002, 2001.

[21] H. Ohki and N. Takeuchi, Upper and lower bound solution with hybrid-type penalty method, *Transactions of JSCES*, Paper No.20060020, pp.1-10, 2006.

[22] K. Washizu, *Variational Methods in Elasticity and Plasticity*, Pergamon Press, New York, 1968.

[23] K. Yamaguchi and N. Takeuchi, Discrete Limit Analysis for Framed Structures by using Hybrid-type Penalty Method, *Bulletin of Research Center for Computing and Multimedia Studies*, Hosei University, Vol.30, pp.1-11, 2016.

[24] Y. Tajiri, R. Mihara and N. Takeuchi, Discrete limit analysis for thin plate by using hybrid-

type penalty method，Journal of applied mechanics, Vol.11, pp.233-242, 2008.

[25] A. Vardanyan and N. Takeuchi, Discrete analysis for plate bending problems by using hybrid-type penalty method, Bulletin of Research Center for Computing and Multimedia Studies: Hosei University, 21, 131-141, 2008.

[26] N. Takeuchi and A. Vardanyan, Elasto-plastic analysis for plate bending problems by using hybrid-type penalty method, Bulletin of Chuvash State Pedagogical University, 6, 179-194, 2009.

[27] T. Kawai, New element models in discrete structural analysis, *Journal of the Society of Naval Architects of Japan*, No.141, pp.187-193, 1977.

[28] Y. Fujiwara, N. Takeuchi, T. Shiomi and A. Kambayashi, Discrete crack modeling of RC structure using hybrid-type penalty method, *International Journal of Aerospace and Lightweight Structures*, Vol.3, No.2, pp.263.275, 2013

[29] Y. Fujiwara, N. Takeuchi, T. Shiomi and A. Kambayashi, Discrete crack analysis of concrete structures using the hybrid-type penalty method, *Computer and Concrete*, Vol.16, No.4, pp.587-604, 2015.

[30] A. Vardanyan and N. Takeuchi, Development of a flat shell element in hybrid-type penalty method, *Bulletin of Research Center for Computing and Multimedia Studies*, Hosei University, Vol.35, pp.21-30, 2020.

[31] A. Vardanyan and N. Takeuchi, Development of flat shell elements for arbitrary-shaped shell structures by using HPM, *Bulletin of Research Center for Computing and Multimedia Studies*, Hosei University, Vol.36, pp.1-10, 2021.

[32] A. Vardanyan, N. Takeuchi and K. Terada, Large displacement analysis with material nonlinear of shell structure using new flat shell elements, Moder Environmental Science and Engineering, Vol.2022, No.5, 2022 (Accept)

[33] Y. Yamada, N. Yoshimura and T. Sakurai, Plastic stress-strain matrix and its application for the solution of elasto-plastic problems by the finite element method, International J. Mech. Sci. Vol.10, pp.343-354, 1968.

[34] A. Sawczuk and T. Jaeger, *Grenztragfahigkeits-Theorie der Platten*, Springer-Verlag,1963.

[35] P. Hodge, P*lastic Analysis of Structures*, McGraw-HillBook Co, Inc., 1959.

[36] R. Frisch-Fay, *Flexible Bars*, Butterworths & Co. Ltd., 1962.

ACKNOWLEDGMENTS

The author wish to express her profound appreciation to her scientific supervisor *Dr. Professor Norio Takeuchi* for his deep and wide knowledge that he continuously shared with her. *Dr. Professor Norio Takeuchi* many years ago believed her and gave her a opportunity to become Hosei International Fund Foreign Scholars Fellow. He also inspired her to aim for the new big, fundamental questions in mechanics and to not be afraid. The author very grateful to *Dr. Professor Norio Takeuchi* for his support and guidance throughout the work on her doctoral thesis.

The author eternally grateful to *Professor Yutaka Tanaka* for his insightful advices and cooperation.

Author’s special thanks for *Professor Hideaki Hamada* for stimulating interesting scientific discussions.

The Author would like to thank to Hosei University Professional Graduate School Scholarship for awarding her the scholarship that supported her studies at the Hosei University.

The author especially thank to her family.